Diss. ETH No. 28571

An exploration of Granular Material

A thesis submitted to attain the degree of

DOCTOR OF SCIENCES OF ETH ZURICH

(Dr. sc. ETH Zurich)

presented by

Christopher McLaren

MSc Process Engineering, ETH Zurich

born on June 18, 1989

citizen of Germany

accepted on the recommendation of

Prof. Dr. Christoph R. Müller, examiner

Prof. Dr. Alex Penn, co-examiner

Prof. Dr. Chris Boyce, co-examiner

2022

1 Table of Contents

2 Summary

Granular material is ubiquitous in our everyday lives. For example, in nature the dynamics of granular materials determine how sand dunes are formed and how avalanches and rockslides propagate. Many products we consume are made of granular materials, e.g. tablets in the pharmaceutical industry or instant coffee in the food industry. Although granular materials are omnipresent and have been studied since decades, there still remains much to be learned about their properties and dynamics. For example, the mixing of granular materials requires high energy inputs, hence, an improved understanding of its mixing behaviour would lead to enormous benefits in energy reduction. Chemical products are often produced from granular materials in a chemical reactor which often is a fluidized bed. Fluidized beds channel gas through a bed of particles, and can operate in multiple regimes, depending on the velocity of the gas flow. When operated above the minimum fluidization velocity, the particles are fluidized and have liquid like properties. It is possible to further agitate the bed with vibration.

In this dissertation we have observed for the first time a new family of gravitational instabilities in mixtures of granular materials when agitated by both vertical vibration and upward gas flow. These instabilities include a Rayleigh-Taylor (R-T)-like instability in which lighter grains rise through a layer of heavier grains forming fingers and granular bubbles. This R-T-like instability was found to arise from the upward-directed drag force that is increased locally by gas channeling and downward-directed contact forces. Therefore, the physical mechanism behind the formation of such fingers is distinctly different to that in liquids. The same gas channeling mechanism was found to lead to further gravitational instabilities, i.e. the rising of granular bubbles and the splitting of granular droplets during their sinking.

The sinking and splitting of granular droplets is examined in more detail. Granular droplets of smaller, but denser particles in a bed of larger and lighter particles is probed both numerically and experimentally. It is observed that a sinking granular droplet performs a series of binary splits resembling the fragmentation of a liquid droplet falling in a miscible fluid, although a different physical mechanism is responsible for the split. Particle-image-velocimetry (PIV) and numerical simulation show that the droplet of high-density particles forms an immobilized zone directly below it. This immobile zone obstructs the downwards motion of the droplet and forces the droplet to spread and ultimately to split. The resulting daughter droplets sink at inclined trajectories around the immobilized zone until they split themselves. The occurrence of consecutive splitting events is explained by the creation and relaxation of the immobilized zone underneath the droplet fragments.

A key requirement for the observation of R-T instabilities is the agitation of the granular bed by both vibration and gas-fluidization. We have explored to what extent the addition of mechanical vibration can reduce the minimum fluidization velocity (U_{mf}). A series of experiments show that vibration reduces both U_{mf} and the minimum bubbling velocity (U_{mb}) in both Geldart Group B and D particles. U_{mf} is reduced more than U_{mb}, allowing a bubble-free fluidization state when the superficial gas velocity is between U_{mf} and U_{mb}. This is a key requirement for the observation of R-T-like instabilities in granular media. U_{mf} and U_{mb} both decrease when the vibration frequency and amplitude are increased. The particle density does not seem to affect the influence of vibration on U_{mf} and U_{mb}, while on the other hand particle size affects the influence of vibration on U_{mf} and U_{mb} non-monotonically.

Next the dissertation studies the mixing in rotating cylinders, a key industrial process. Particle image velocimetry was performed on the free surface of the bed of particles within a rotating cylinder that is operated in the avalanching regime. The velocities of the particles determined by PIV are used to examine the validity of existing avalanche models. The movement of bed particles (at the surface) is shown to depend on their location on the surface of the bed at the start of the avalance with particles located near the center of the bed travelling the farthest. The distance travelled by particles during an avalanche decreases at an increasing rate the farther the particle is from the center. The start of an avalanche can be linked to a single initiation point, that may even be located on the bottom half of the bed. An avalanche quickly propagates through the entire free surface, with

90 % of the surface in motion within 257 ms (20 % of the duration of an avalanche event). An updated geometric model is proposed which better describes the motion on the surface during avalanching of the granular bed. Experimental mixing measurements confirm the higher accuracy of the newly proposed avalanching model when compared to exisiting ones.

3 Zusammenfassung

Granulare Materie ist in unserem Alltag allgegenwärtig. In der Natur bestimmt die Dynamik granularer Materie beispielsweise, wie sich Sanddünen bilden und wie sich Lawinen und Steinschläge ausbreiten. Viele Produkte, die wir konsumieren, bestehen aus granularem Material, z. B. Tabletten in der Pharmaindustrie oder Instantkaffee in der Lebensmittelindustrie. Obwohl granulare Materialien allgegenwärtig sind und seit Jahrzehnten erforscht werden, gibt es noch viel über ihre Eigenschaften und Dynamik zu lernen. So erfordert beispielsweise das Mischen von granularen Materialien einen hohen Energieaufwand, so dass ein besseres Verständnis ihres Mischverhaltens zu enormen Energieeinsparungen führen würde. Produkte in der chemischen Industrie werden häufig mit Hilfe von granularen Materialien in Wirbelschichtreaktoren hergestellt. In Wirbelschichtreaktoren wird Gas durch ein Bett aus Partikeln geleitet, je nach Geschwindigkeit des Gasstroms arbeitet der Reaktor dabei in verschiedenen Betriebszuständen. Bei einem Betrieb oberhalb der minimalen Fluidisierungsgeschwindigkeit werden die Partikel fluidisiert und haben flüssigkeitsähnliche Eigenschaften. Ausserdem ist möglich, das Bett durch Vibration noch stärker anzuregen.

In dieser Dissertation haben wir zum ersten Mal eine neue Familie von Gravitationsinstabilitäten in Mischungen aus granularen Materialien beobachtet, wenn diese sowohl durch vertikale Vibration als auch durch einen aufwärts gerichteten Gasstrom in Bewegung versetzt werden. Zu diesen Instabilitäten gehört eine Rayleigh-Taylor (R-T)-ähnliche Instabilität, bei der leichtere Partikel durch eine Schicht aus schwereren Partikeln aufsteigen und Finger und Partikelblasen bilden. Es wird beobachtet, dass diese R-T-ähnliche Instabilität auf die nach oben gerichtete Widerstandskraft zurückzuführen ist, die lokal durch die Kanalisierung von Gas und nach unten gerichtete Kontaktkräfte verstärkt wird. Der physikalische Mechanismus, welcher der Bildung solcher Finger zugrunde liegt, unterscheidet sich also deutlich von dem in Flüssigkeiten. Es wird ausserdem beobachtet, dass derselbe Mechanismus der Gaskannalisierung zu weiteren Gravitationsinstabilitäten führt, d. h. zum Aufsteigen von Partikelblasen und zur Aufspaltung von Partikeltröpfchen während ihres Absinkens.

Das Absinken und Aufspalten von Partikeltröpfchen wird daher genauer erläutert. Dazu werden Partikeltröpfchen aus kleineren, aber dichteren Partikeln in einem Bett aus größeren und leichteren Partikeln sowohl numerisch als auch experimentell untersucht. Es wird beobachtet, dass ein sinkender Partikeltropfen eine Reihe von binären Spaltungen durchläuft, ähnlich der Fragmentierung eines Flüssigkeitstropfens, der in eine mischbare Flüssigkeit sinkt, obwohl dabei ein anderer physikalischer Mechanismus für die Spaltung verantwortlich ist. Particle Image Velocimetry (PIV) und numerische Simulationen zeigen, dass der Tropfen aus Partikeln mit hoher Dichte direkt unter sich eine immobilisierte Zone bildet. Diese immobilisierte Zone behindert die Abwärtsbewegung des Tropfens und zwingt den Tropfen, sich auszubreiten und schließlich zu spalten. Die entstehenden Tochtertröpfchen sinken auf geneigten Bahnen um die immobilisierte Zone, bis die Tochtertröpfchen sich wiederrum selbst aufspalten. Das Auftreten von aufeinanderfolgenden Spaltvorgängen wird durch die Entstehung und Lockerung der immobilisierten Zone unter den Tröpfchenfragmenten erklärt.

Eine wichtige Voraussetzung für die Beobachtung von R-T-Instabilitäten ist die Bewegung des Partikelbetts sowohl durch Vibration als auch durch Gasfluidisierung. Wir haben untersucht, inwieweit das Zuschalten mechanischer Vibration die minimale Fluidisierungsgeschwindigkeit (U_{mf}) verringern kann. Eine Reihe von Experimenten zeigt, dass Vibration sowohl U_{mf} als auch die minimale Blasenbildungsgeschwindigkeit (U_{mb}) bei Partikeln der Geldart-Gruppen B und D reduziert. U_{mf} wird dabei stärker reduziert als U_{mb}, was einen blasenfreien Fluidisierungszustand ermöglicht, wenn die Leerrohrgeschwindigkeit zwischen U_{mf} und U_{mb} liegt, was eine wichtige Voraussetzung für die Beobachtung von R-T-ähnlichen Instabilitäten in granularer Materie ist. U_{mf} und U_{mb} nehmen beide ab, wenn die Schwingungsfrequenz und -amplitude erhöht werden. Eine Variation der Partikeldichte verändert dabei den Einfluss der Vibration auf U_{mf} und U_{mb} nicht, während sich eine Variation der Partikelgröße auf den Einfluss der Vibration auf U_{mf} und U_{mb} nichtmonoton auswirkt.

Als Nächstes wird in dieser Dissertation das Mischen in rotierenden Zylindern, einem industriellen Schlüsselprozess, untersucht. Dafür wird PIV benutzt um die freie Oberfläche des Partikelbetts innerhalb eines rotierenden Zylinders, welcher im sogenannten im lawinenbildenden Modus betrieben wird, zu untersuchen. Die durch PIV ermittelten Partikelgeschwindigkeiten werden verwendet, um die Gültigkeit der bestehenden

Lawinenmodelle zu untersuchen. Es wird gezeigt, dass die Bewegung der Partikel (an der Bettoberfläche) von ihrer Position auf der Bettoberfläche zu Beginn der Lawine abhängt, wobei sich die Partikel am weitesten bewegen, die sich nahe der Mitte des Bettes befinden. Die von den Partikeln während einer Lawine zurückgelegte Entfernung nimmt mit zunehmender Entfernung zur Mitte ab. Der Start einer Lawine kann mit einem einzigen Auslösepunkt in Verbindung gebracht werden, der sich sogar in der unteren Hälfte des Bettes befinden kann. Eine Lawine breitet sich schnell über die gesamte freie Oberfläche aus, wobei sich 90 % der Oberfläche innerhalb von 257 ms losbewegen (20 % der Dauer eines Lawinenereignisses). Es wird ein aktualisiertes geometrisches Modell vorgestellt, welches die Bewegung eines Lawinenereignisses auf der Oberfläche des Partikelbetts besser beschreibt als bisherige Modelle. Experimentelle Messungen der Partikeldurchmischung bestätigen die höhere Genauigkeit des neuen Modells.

4 Introduction

Granular material is an agglomeration of discrete, solid, micro- or macroscopic particles [1]. Every day we come into contact with granular material, e.g. in nature in the form of sand or rocks, or even consuming them in pharmaceuticals or manufactured food. In industry, granular materials are processed to create products for the mineral, ceramic, metallurgical, chemical, pharmaceutical, waste or food industries [2 – 15]. In particular, dynamic granular materials are of interest as their processing often takes place in rotating vessels, or vibrated or fluidized beds. Many fascinating natural phenomena such as avalanches, moving sand dunes and rockslides are also simply dynamic granular material. Although, previous works have uncovered numerous similarities between granular flows and liquids, there are also some fundamental differences in forces which are active, e.g. frictional forces in granular material or surface tension in liquids [16 – 18]. In the EU 30 % of the industrial energy usage is used in the chemical and construction sectors, where respectively reactors and the processing of cement are large contributors. Hence, a better understanding of the dynamics that occur during the processing of granular materials would lead to savings in energy.

Figure 1 Remnants of a rockslide in Randa, Switzerland.

4.1 Mixing

The mixing of granular materials is used across many different industries: ceramics, fertilizers, detergents, glass, pharmaceuticals, processed food and powder metallurgy [2, 19]. However, granular materials can also segregate due to differences in density, sizes and shape [2]. While certain segregation phenomena such as radial segregation in rotating drums are well understood, others are less so, e.g. axial segregation or shape-induced segregation [12].

Besides the fact that we currently have no comprehensive understanding of the processes that govern the mixing (and the simultaneously occurring segregation) in granular materials, there are also difficulties in quantifying the quality of mixing [3]. In this regard two type of criteria have been introduced: The first criterion is the extent of segregation, i.e. the variation of the local composition compared to the average composition [4]. The second criterion determines the segregation scale, i.e. measuring the size of areas where components have not mixed [4]. A uniform, random mix is defined by Raasch [5] as a state at which "the probability of coming across an ingredient of the mix in any subsection of the area being examined is equally high at any point in time for all subsections of the same size".

Lacey argued that three mechanisms contribute to mixing: convection, diffusion, and shearing [6]. Convection refers to the coherent motion of a relatively large assembly of particles whereas diffusion is the random movement of an individual particle [7]. Shear mixing occurs when two planes within the granular material slip relative to each other [7]. In a rotating drum or a fluidized bed, mixing through convection is the dominating process.

4.2 Rotating drum

A rotating drum setup is extremely simple, i.e. a drum filled with granular material that is rotating at a given speed. This setup has been used to investigate a large range of physical phenomena [8] such as the shape of the free surface in liquids [9], the effect of liquid viscosity on segregation in suspensions [10] and segregation and pattern formation in granular materials [11] . Furthermore, rotating drums are frequently used in the industrial processing of granular material, e.g. for the manufacture of cement. Depending on the operation parameters, a rotating cylinder may be operated in different regimes. The rotational speed largely determines the regime (akin to the gas velocity in a fluidized bed). Figure 1 shows schematics of several regimes in a rotating drum as a function of rotation speed. In rotating cylinders, the rotational speed is commonly given in a non-dimensionalized form through the Froude number ($Fr = \omega^2 R/g$), where ω is the rotational speed, R (L in figure 1) is the radius of the cylinder and g is the gravitational acceleration. At low rotational speeds avalanching occurs. In the avalanching regime there are two discrete phases, which occur one after the other. The first phase is solid body rotation. The granular material rotates together with the drum until a critical angle β_i of the free surface is reached. When the critical angle β_i is reached the granular material avalanches down the free surface until the free surface is at angle β_f. The process repeats itself. The higher the rotation speed, the faster this process and the less time there is between avalanches. At high enough rotation speeds the avalanches are no longer separated and a continuous flow regime takes over which is called the rolling regime. At even higher speeds the cataracting regime will be entered, where some particles become airborne and the free surface is not flat anymore [2]. For Fr = 1 centrifuging occurs, where high centrifugal forces lead to a continuous solid body rotation of the bed. **Figure 2** shows the various flow regimes.

A key application of rotating drums in industry is the mixing of granular material. Various models have been developed in order to describe mixing in the avalanching regime. For example, Metcalfe *et al.* [12] developed a model for particle mixing in the avalanche regime and compared its predictions with experimental data obtained in a pseudo two-dimensional rotating cylinder. In their model, during an avalanche event, a wedge of

material from the top half of the surface (dark grey in figure 2 a, b and c) slides down the free surface such that after the avalanche it occupies a new wedge at the bottom half of the free surface. It was assumed that no particles outside of this wedge are affected by the avalanche. The model splits the problem of mixing in the avalanching regime into two components: the transport of wedges from the upper surface down the free surface and mixing within these wedges. Metcalfe et al. [12] assumed perfect mixing within the wedge and when comparing to experimental data, good agreement between their model and experimental data was found (**Figure 3** d and e).

The model of Metcalfe et al. [12] was later refined by Lim et al. [13] who performed positron emission particle tracking (PEPT) experiments in rotating cylinders when operated in the avalanching regime. In order to tag a single particle, they irradiated a particle of glass with a beam of ^3He ions from a cyclotron to convert some of the oxygen atoms in the solid into a radionuclide [13]. Radionuclides decay under the emission of a positron which is annihilated under the emission of two γ-rays, which are detected and used to determine the position and displacement of the particle through triangulation. Lim et al. [13] found particles to not slide down in a single avalanche but rather to slump down the free surface in multiple instinct avalanches, thus disproving Metcalfe et al.'s [12] wedge model. Based on their experimental findings Lim et al. [13] proposed a modified wedge model that is shown in **Figure 4**. In Lim et al.'s [13] model, when the critical angle γ_s (β_i in **Figure 2**) is reached, a wedge made up of the entire chord length (tapered downward; shaded wedge) avalanches down yielding a wedge of the entire chord length (tapered upwards; dotted wedge) with the free surface at an angle of γ_t (β_f in **Figure 2**) The avalanching material moves on average 1/3 of the chord length. This was determined experimentally by varying the Froude number and finding that for the lowest Froude numbers particles took 3.5-4 avalanches to travel down the chord and when increasing the Froude number to Fr = 0.00006 about 1.5 avalanches to descend the chord.

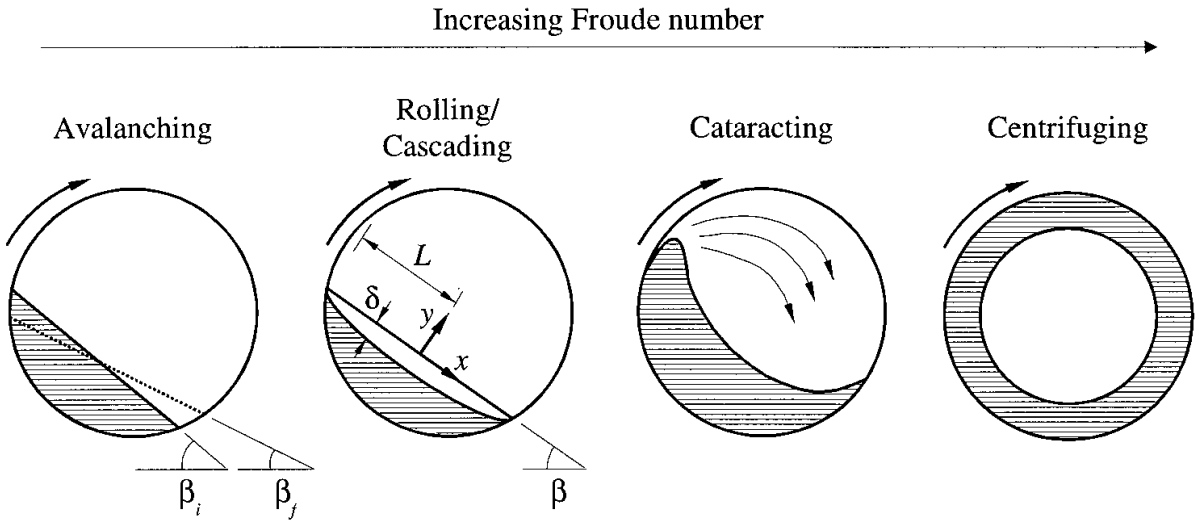

Figure 2 Schematic view of different flow regimes in a rotating cylinder with increasing Froude number (rotation speed). Here β_i is the angle of the free surface just before an avalanche occurs and β_f is the angle just after an avalanche; β is the free surface angle in the rolling regime, which is the dynamic angle of repose [2].

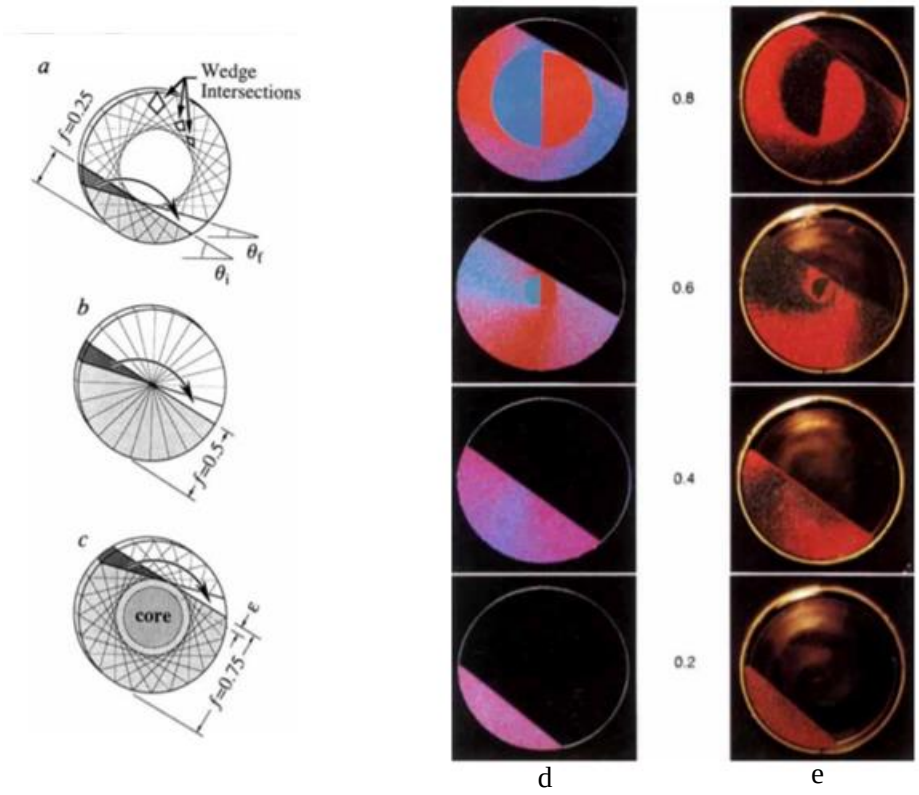

Figure 3 left: Schematic view of Metcalfe et al.'s [12] wedge model for different fill levels: a) < 50 % fill level, b) 50 % fill level and c) > 50 % fill level; right: comparison of predictions of Metcalfe et al. [12] model (left) and experiments (right) [12].

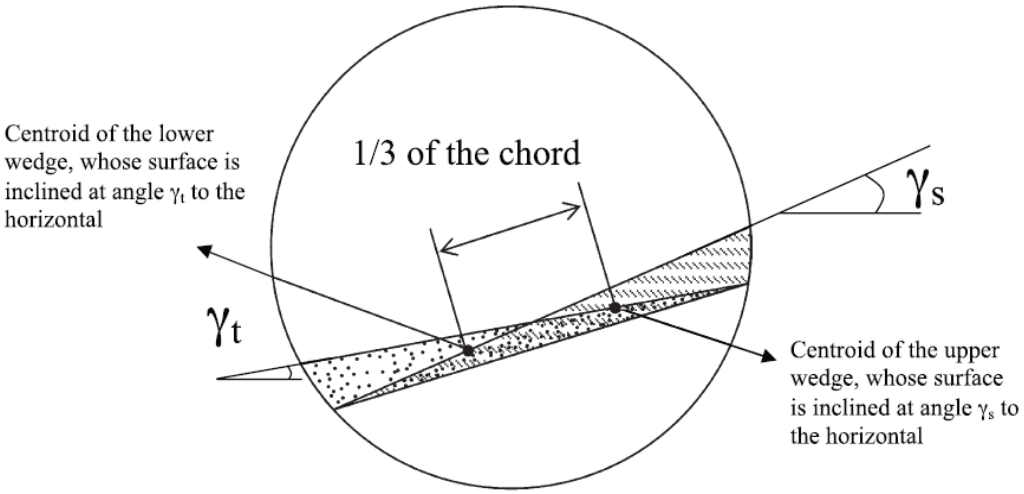

Figure 4 Schematic of the modified wedge model of Lim et al. [13].

4.3 Fluidization

If a flow of fluid passes through a bed of particles placed in a column at low flow rates, the position of the particles in the bed remains fixed (fix or packed bed). Increasing the flow rate of the fluid, the bed starts to expand as the distance between the particles is slightly increased. Once the fluid flow is raised to the point at which the pressure drop through the bed is equal to the weight of the fluid and particles per cross sectional area, the bed is said to be at minimum fluidization [14]. For particles in Geldart's group A increasing the flow rate beyond minimum fluidization leads to a further expansion of the bed, while Geldart's group B and D particles form bubbles immediately as minimum fluidization is surpassed. **Figure 5** gives an overview of the different operating regimes of a fluidized bed.

The superficial air flow speed in a fluidized bed is the volumetric airflow divided by the cross-sectional area of bed. At minimum fluidization, the pressure drop across the bed is equal to the weight of the bed divided by its cross-sectional area, yielding the following equation (3.1):

$$\frac{\Delta p_{bed}}{L} = \left(1 - \epsilon_{mf}\right)\left(\rho_s - \rho_g\right)g \tag{3.1}$$

where L is the height of the bed, ϵ_{mf} is the void fraction at minimum fluidization, ρ_s t is the density of the particles, ρ_g is the density of the gas and Δp_{bed} is the pressure drop of the bed. To incorporate the fluid velocity into equation (3.1), typically Ergun's equation (3.2) is used to express the pressure drop, viz.

$$\frac{\Delta p_{bed}}{L} = 150\frac{(1-\varepsilon)^2}{\varepsilon^3}\frac{\mu U}{\phi^2 d_p^2} + 1.75\frac{1-\varepsilon}{\varepsilon^3}\frac{\rho_g U^2}{\phi d_p} \tag{3.2}$$

Here μ is the viscosity of the gas, and U is the superficial gas velocity, d_p is the particle diameter, and ϕ_p is the sphericity of the particles. At minimum fluidization $\epsilon = \epsilon_{mf}$ and $U = U_{mf.}$ and putting 3.2 into 3.1 yields:

$$\frac{1.75}{\epsilon_{mf}^3 \phi_p}\left(\frac{d_p U_{mf}\rho_g}{\mu}\right)^2 + \frac{150\left(1-\epsilon_{mf}\right)}{\epsilon_{mf}^3 \phi_p^2}\left(\frac{d_p U_{mf}\rho_g}{\mu}\right) = \frac{d_p^3 \rho_g\left(\rho_s - \rho_g\right)g}{\mu^2} \tag{3.3}$$

Equation 3.3 may be reformulated using the Archimedes number, *Ar* and the Reynolds number, *Re*:

$$Ar = \frac{d_p^3 \rho_g\left(\rho_s - \rho_g\right)g}{\mu^2}$$

$$Re_{p,mf} = \frac{d_p \rho_g U_{mf}}{\mu}$$

yielding:

$$\frac{1.75}{\epsilon_{mf}^3 \phi_p} Re_{p,mf}^2 + \frac{150(1-\epsilon_{mf})}{\epsilon_{mf}^3 \phi_p^2} Re_{p,mf} = Ar \equiv K_1 Re_{p,mf}^2 + K_2 Re_{p,mf} \qquad (3.4)$$

where

$$K_1 = \frac{1.75}{\epsilon_{mf}^3 \phi_p} \quad \text{and} \quad K_2 = \frac{150(1-\epsilon_{mf})}{\epsilon_{mf}^3 \phi_p^2}$$

Typically, the values of ϵ_{mf} and ϕ_p are not known. Using experimental data, Wen and Yu [15] developed a correlation for K_1 and K_2, which spans a large set of values for ϵ_{mf}, d_p and ϕ_p, viz. covering d_p = 0.05 - 50 mm, ϵ_{mf} = 0.385 - 0.935, ϕ_p = 0.136 - 1.0, and particle diameter to column diameter ratios ranging between 0.000807 - 0.25 [15]. The following relationships between K_1 and K_2 were determined by Wen and Yu:

$$\frac{1}{K_1} = 0.0408 \quad \text{and} \quad K_2 = 67.4 \times K_1$$

giving in turn:

$$Re_{p,mf} = [(33.7)^2 + 0.0408 Ar]^{1/2} - 33.7$$

As Wen and Yu reported an average deviation of 34 % between experimental values and their correlation, even nowadays the minimum fluidization velocity is often determined experimentally.

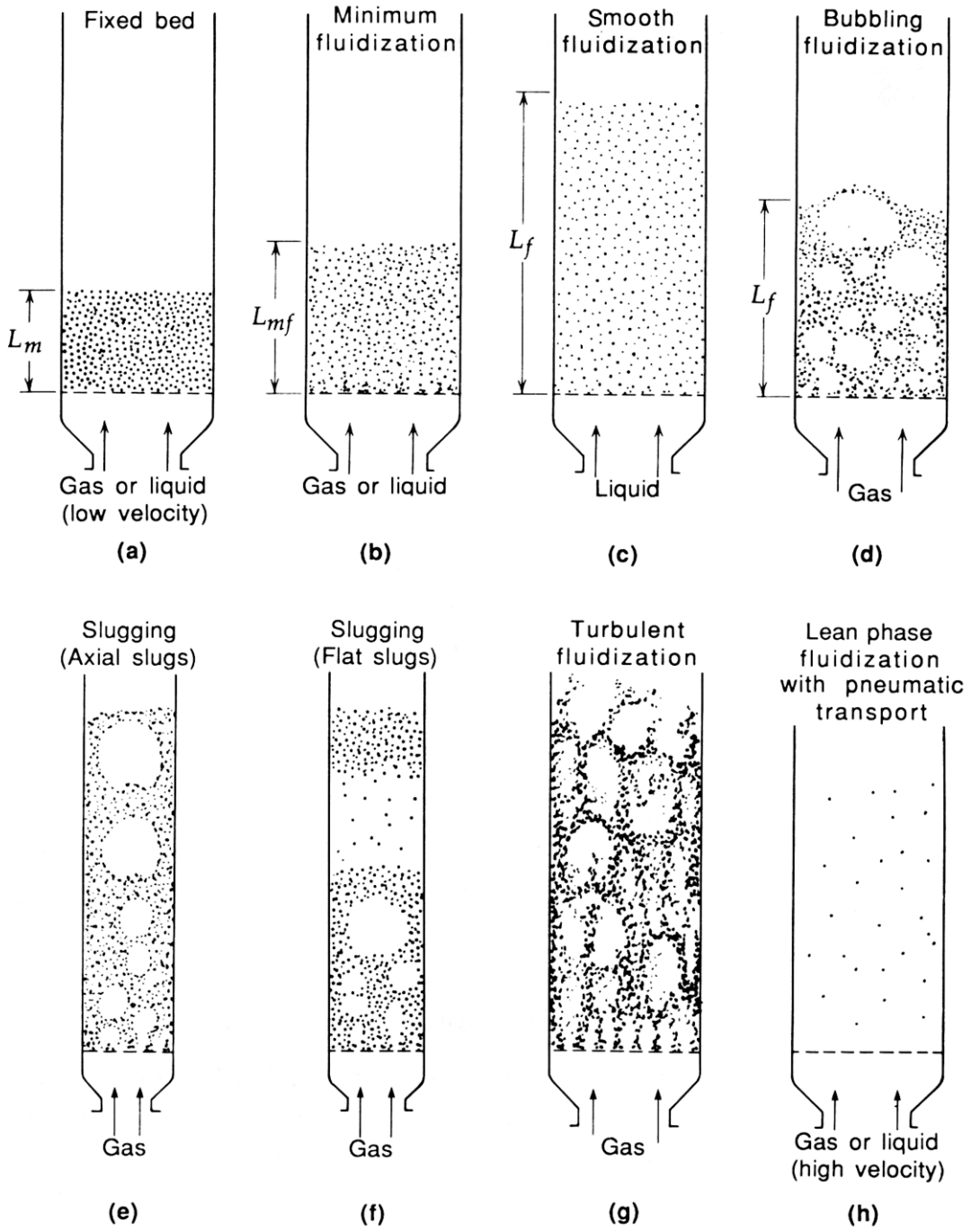

Figure 5 Schematic view of different flow regimes in a fluidized bed from Kunii and Levenspiel [14].

For Geldart's group B and D particles bubbling occurs when surpassing U_{mf} (for Geldart's group A particles there exist a minimum bubbling velocity, U_{mb}, that is larger than U_{mf}). The formation of (small) bubbles in fluidized beds is a desirable feature as it promotes mixing. For Geldart's group A particles there exists a region of homogeneous (smooth) fluidization for U > U_{mf}. This is because for Geldart's group A particles (d_p ~ 20-100 µm, ρ ≲ 1500 kg/m^3) $U_{mf} < U_{mb}$ [16] and for $U_{mf} < U < U_{mb}$ the bed "absorbs" the additional gas flow (above U_{mf}) through a homogenous bed expansion. For Geldart's Group B (particle diameter, d_p ~ 100-800 µm, ρ ~ 1400-4000 kg/m^3 and D (d_p ≳ 800 µm, ρ ≳ 2000 kg/m^3) particles, $U_{mf} \approx U_{mb}$ [16]. Cohesive particles, i.e. Geldart's Group C (d_p ≲ 20 µm), e.g. flour, are difficult to fluidize [16] leading often to channeling. One approach to fluidize cohesive particles is the introduction of mechanical vibration to the bed.

4.4 Rayleigh Taylor instability

The Rayleigh-Taylor (R-T) instability [17] is a fluid mechanical phenomenon which describes the formation of fingers and/or bubbles when a denser fluid is placed on top of a lighter fluid. The R-T instability is found in many systems including e.g. the formation of mushroom-shaped clouds in nuclear explosions [18], fingering patterns in supernova explosions (shown in

Figure 6) [18] and structures in lava lamps [19]. While the R-T instability dates back to 1880, more recently, visually similarly appearing fingering patterns [19, 36, 37] have been observed also in granular systems. For example, density-driven, R-T-like phenomena in granular systems have been observed in 2D systems that contain a liquid [20] or gas [21] on top of a particle bed and that is rapidly inverted. This leads to the fluid phase pushing upward through falling particles and can be seen in **Figure 7** [20].

The R-T behavior of mixtures of two types of grains is of great relevance for several natural phenomena, including the formation of geological structures ranging from mud-sand sediments [22] to deposits of sediment under glaciers [23] to volcanic flows [24]. Typically, R-T driven dynamics are prevented from occurring in granular systems because: (i) there exist strong frictional forces between grains preventing granular flow and (ii) in granular systems surface tension is absent, which is the "stabilizing" force in the R-T instability in fluids.

When only gas-fluidization is applied to granular particles, gas bubbles which rise through the system are formed and granular structures very distinct from those associated with the R-T instability are observed [25]. On the other hand the vibration of dry grains causes buoyant segregation [26], but without gas fluidization it did not lead to the liquefaction necessary for R-T structures to form.

While so far R-T instabilities have not been observed in single phase granular systems, R-T instabilities have been observed in liquid-particle systems. In nature, seismic shaking or experimentally, shaking via a vibrating system of the liquid-particle system causes liquefaction allowing movement of the grains and formation of R-T-like structures [27].

4.4.1 Deformation of a sinking droplets

A further fascinating phenomenon in fluid mechanics is the deformation of a liquid droplet when falling in a miscible liquid [28]. In miscible fluids, a droplet of a dense liquid can form a torus when falling into a miscible but less dense liquid. Arrechi et al. [29] found the development of such a torus to depend on the Fragmentation number, F, i.e. the ratio of the diffusion time to the time required for the fluid to convectively mix. The fragmentation number is given by $F = g\frac{\Delta\rho V}{\mu D}$ where respectively μ, $\Delta\rho$, V and D is the viscosity of the surrounding liquid, the difference in the densities of the liquids, the volume of the droplet, and the diffusion coefficient [29]. For values of F greater than the critical value F_c (determined empirically) a torus will form, and the droplet will fragment, for values lower than F_c the droplet disappears via diffusion [29]. During the sinking of the droplet, the diameter of the torus increases up to the point at which the RT instability creates discrete circumferential aggregations that ultimately become large enough to separate and form new toroidal structures [46 – 50]. Similar instabilities leading to deformation of the interface, have also been observed in two-phase granular materials. For example, a swarm of glass particles sinking in a glycerol solution with very low Reynolds numbers ($R_e << 1$), transforms into a torus with increasing radius and eventually splits (shown in **Figure 8**) [51, 52].

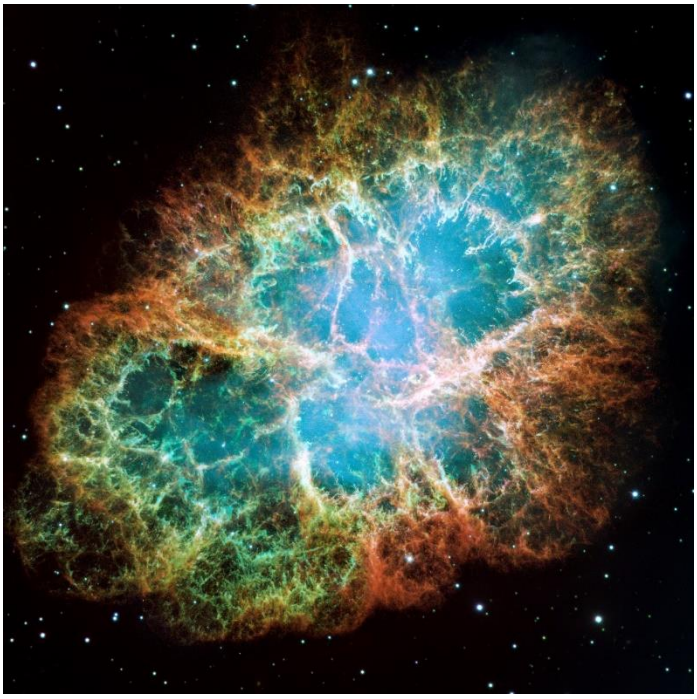

Figure 6 Crab Nebula taken by NASA's Hubble Space Telescope [30].

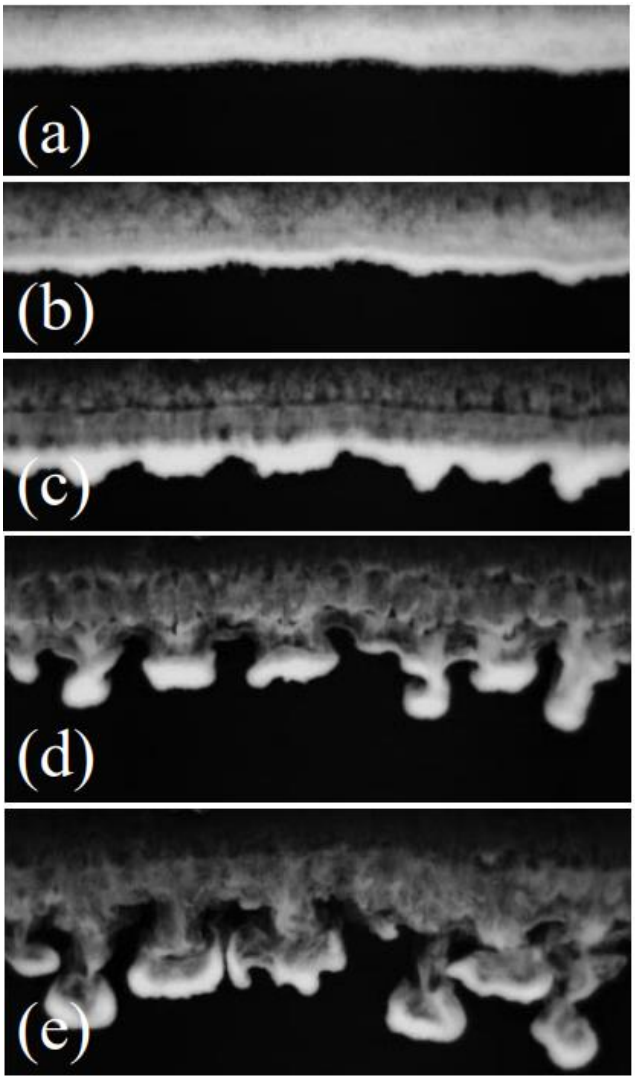

Figure 7 Sand-water interfaces at different time steps: (a) 20 ms, (b) 80 ms, (c) 140 ms, (d) 200 ms, and (e) 260 ms. The size of the sand particles is 71-80 μm and the sand mass in the cell is 2 g. The frames show the middle part of the cell and have a length of 68 mm [20].

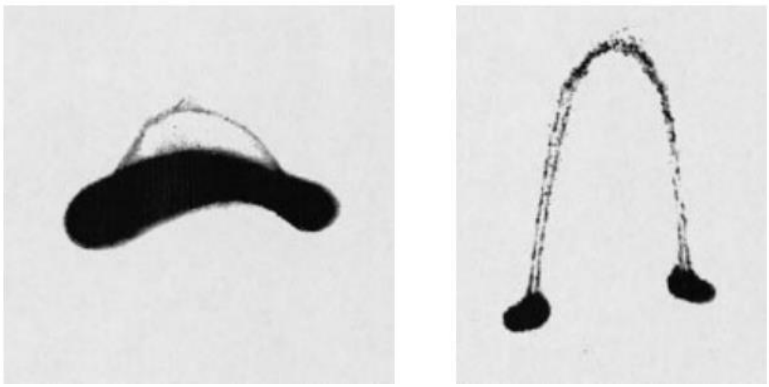

Figure 8 Evolution of a swarm of glass particles sedimenting in pure glycerin. (a) The open torus is spanned by a "membrane" of particles. (b) The open torus formed from a suspension drop becomes unstable and breaks into two secondary droplets [31].

4.5 Structure of this dissertation

Chapter 5 studies granular instabilities in binary granular material. The Rayleigh-Taylor (R-T) instability [17] is a phenomenon in classical fluid mechanics in which a lighter fluid pushes into a denser fluid above it due to buoyancy. This yields "fingers" and "bubbles" of lighter fluid in the denser fluid. R-T behavior is prevented from occurring between grains under typical conditions due to two differences to liquids: (i) there exist strong frictional forces between grains when put under pressure which prevent them from flowing and (ii) grains do not exhibit cohesive forces, which would be necessary in order to create a surface tension between two types of granular material, and surface tension is the key stabilizing force in the classic R-T instability. Here, we address the question if an analog of the R-T instability exists between dry grains of different density when exciting a granular system using a combination of both vibration and gas flow and, if so, how the phenomenon compares with that occurring in fluids.

Chapter 6 explores the reduction in the minimum fluidization velocity (U_{mf}) and minimum bubbling velocity (U_{mb}) in gas-solid fluidized beds due to vibration. Experiments show that vibration may reduce both U_{mf} and U_{mb} in Geldart Group B and D particles. U_{mf} is reduced more than U_{mb}, creating a densely packed, bubble-free fluidization state with a superficial gas velocity between U_{mf} and U_{mb}. This increases the range of gas velocities for which particles can mix without gas bubbles forming. The "components" of vibrational strength, i.e. frequency and amplitude, both decrease U_{mf} and U_{mb} when increased. The results for U_{mf} and U_{mb} in multiple vibration conditions can be condensed along a single curve.

Chapter 7 investigates the physics behind the sinking and splitting of a granular droplet composed of smaller and denser particles in a bed of larger and lighter particles. A sinking granular droplet of denser particles undergoes a series of binary splits mirroring the fragmentation of a liquid droplet falling in a miscible fluid. Particle-image-velocimetry and numerical simulations demonstrate that the droplet of high-density particles causes the formation of an immobilized zone underneath the droplet which obstructs the downwards motion of the droplet causing the droplet to spread and ultimately to split. The role of friction, density, and size of the particles is discussed.

Chapter 8 covers the dynamics of avalanches in a rotating cylinder. Particle image velocimetry has been applied to measure particle velocities on the free surface of a bed of particles during avalanching within a rotating cylinder. The movement of particles is shown to depend on their location on the surface of the bed, with particles located closer to the center of the bed travelling the farthest, while the distance travelled decreases at an increasing rate for particles located farther from the center. Based upon these insights, a new geometric model for the mixing in rotating drums is proposed.

Finally, chapter 8 summarizes the conclusions of this dissertation and outlines some remaining research challenges.

5 Gravitational Instabilities in Binary Granular Materials

Adapted from: McLaren, C. P., Kovar, T. M., Penn, A., Müller, C. R., & Boyce, C. M. (2019). Gravitational instabilities in binary granular materials. Proceedings of the National Academy of Sciences, 116(19), 9263-9268.

5.1 Significance

Flow of granular materials, such as sand and catalytic particles, is critical to a wide range of natural phenomena and industrial processes. However, the physics underlying granular flows is poorly understood. We report the discovery of gravitational instabilities in binary granular materials driven by a gas channeling mechanism unseen in fluids. A Rayleigh-Taylor instability analog is observed despite a lack of surface tension between grains, while a droplet branching phenomenon demonstrates a deviation from fluid motion due to solidification of particles. These discoveries shed new light on granular dynamics and can potentially explain geological formations and enable new process technologies.

5.2 Abstract

The motion and mixing of granular media are observed in several contexts in nature, often displaying striking similarities to liquids. Granular dynamics occur in geological phenomena and also enable technologies ranging from pharmaceuticals production to carbon capture. Here, we report the discovery of a new family of gravitational instabilities in granular particle mixtures subject to vertical vibration and upward gas flow, including a Rayleigh-Taylor (R-T)-like instability in which lighter grains rise through heavier grains in the form of “fingers” and “granular bubbles”. We demonstrate that this R-T-like instability arises due to a competition between upward drag force increased locally by gas channeling and downward contact forces, and thus the physical mechanism is entirely different from that found in liquids. This gas channeling mechanism also generates other gravitational instabilities: the rise of a granular bubble which leaves a trail of particles behind it and the cascading branching of a descending granular droplet. These instabilities suggest new opportunities for patterning within granular mixtures.

5.3 Introduction

From moving sand dunes [32] to avalanches [33], granular motion forms the basis of several natural phenomena. These dynamics are also utilized in pharmaceuticals production [34] and carbon capture [35]. Previous studies have found fascinating similarities between granular and liquid flow, e.g., wavy instabilities found in grains under shear [36], gas bubbles rising through ensembles of particles [17, 18] and particle droplets forming in hourglass streams [37] and tapped plates [38]. The Rayleigh-Taylor (R-T) instability [17] is a classic fluid mechanical phenomenon in which lighter fluid pushes into denser fluid above it due to buoyancy, producing “fingers” and “bubbles” of lighter fluid. This instability manifests itself in a broad range of systems, from the formation of mushroom-shaped clouds in nuclear explosions [18] to fingering patterns in supernova explosions [18] to structures in lava lamps [19]. A variety of fingering patterns [19, 36, 37] have been observed in grains, including density-driven, R-T-like phenomena when a closed cell containing liquid [20] or gas [21] and particles is quickly inverted and the fluid pushes upward on the falling particles.

The understanding and prediction of R-T behavior between two types of grains is of great significance in multiple scientific fields, including geological structures ranging from mud-sand sediments underwater [22] to deposits under glaciers [23] to volcanic flows [24]. Two differences from traditional fluid flow prevent R-T behavior from occurring between grains under typical conditions: (i) grains under pressure have a solid-like nature with strong frictional forces preventing them from flowing like a fluid and (ii) grains typically do not have significant cohesive forces to create a surface tension between two types of granular material, and surface tension provides the stabilizing force in the classic understanding of the R-T instability. Previous studies have shown that seismic shaking of granular material saturated with water can cause liquefaction, enabling grains to

move and create R-T-like structures [27]. “Fluidization” of granular material based on the upward flow of gas or liquid suspending the particles can also allow grains to flow like liquid. However, prior studies have shown that upward flow of liquid leads to either a homogeneous “layer inversion” [39] if both particles are fluidized, or the formation of volcano-like “water escape structures” [40] if only the lighter grains are fluidized. Fluidization via gas flow creates gas bubbles which rise through the system, leading to the formation of granular structures very distinct from those associated with the R-T instability [25]. Vibration of dry grains with interstitial gas causes buoyant segregation [26], but without net gas flow interstitial gas does not lead to the liquefaction necessary for R-T structures to form. Here, we seek to address the question if an analog of the R-T instability exists between dry grains of different density when exciting a granular system using a combination of vibration and gas flow and, if so, how the underlying mechanism compares with that occurring in conventional fluids.

5.4 Experimental Setup

Our experiments consist of a model binary granular system with two sets of spherical particles of different diameters and densities (color-coded) arranged in a classic R-T setup (see **Figure 9** and the Supplementary Movie) with the light particles (black) below the heavy particles (white). The cell, a “vibrated-fluidized bed”, shakes vertically to induce motion in the grains and contains upward air flow at velocities close to the “minimum fluidization velocity”, U_{mf}, needed to suspend the particles by providing a drag force which offsets their weight. Under the conditions, both sets of particles exhibit liquid-like behavior, i.e. they are loosely packed and can flow. However, importantly, the system does not exhibit any gas bubbling or bulk convection of particles, as would happen if the gas flow or vibration strength were increased. The U_{mf} of both sets of particles is similar because the light particles have a larger diameter than the heavy particles ($U_{mf} \propto d_p^{0.5}\rho_p$).

5.4.1 Materials and Methods

a. Vibrated-fluidized Bed

The vibrated-fluidized bed was constructed of polymethyl methacrylate (PMMA). It was 200 mm in width, 500 mm in height and 10 mm in depth. In each experiment, it was filled to a height H_0 = 400 mm with particles. Air at ambient conditions was passed through a perforated plate with 20 holes in its base to ensure even distribution of gas at the bottom. The air was bubbled through a humidifier prior to passing through the bed in order to keep a constant relative humidity of 87-91 % in the air and keep electrostatic forces from building up on the surfaces of the particles. The gas flow rate was controlled using a mass flow controller (F-203AV, Bronkhorst). The bed was placed on top of an electrodynamic shaker (Labworks Inc., ET-139), which generated a vertical sinusoidal displacement, $\delta = A\sin(2\pi ft)$, using a controller (Labworks Inc. VL-144), an amplifier (Labworks Inc., PA-138-1) and an accelerometer (PCB Piezotronics Inc., J352C33). Each experiment was initiated by increasing the gas flow to the desired superficial velocity and then commencing the vibration shortly thereafter. The experiment shown in **Figure 15** was conducted in an identical system, but with a width of 400 mm.

b. Particles

The “light” particles were spherical glass beads from Sigmund Lindner GmbH. They were colored black to create a contrast with the white color of the “heavy” particles. The light particles had a density of 2500 kg/m^3, as measured by the manufacturer. Three size ranges of light particles were used: Type S.L: 0.5-0.75 mm, type M.L: 1.55-1.85 mm and type L.L: 2.45-2.9 mm. Based on optical imaging, the size distribution of Type S.L particles was 0.61 ± 0.06 mm. The size distribution of Type M.L particles was: 1.70 ± 0.07 mm; these particles were used in most experiments. The size distribution of Type L.L particles was 2.75 ± 0.13 mm. Type M.L particles were sieved with a 1.7 mm sieve to produce particles of two size distributions: Type M.L(a) particles with a size distribution of 1.73 ± 0.06 mm and Type M.L(b) particles with a size distribution of 1.64 ± 0.05 mm. Type M.L(b) particles were used in **Figure 10** (d)(i).

The "heavy" particles were spherical ceramic beads from SiliBeads. They had a density of 6000 kg/m^3, as measured by the manufacturer. Three size ranges were used: Type S.H: 0.4-0.5 mm Type M.H: 1.0-1.2 mm and Type L.L: 1.6-1.8 mm. Based on optical imaging, the size distribution of Type M.H particles was: 1.17 ± 0.06 mm; these particles were used in most experiments. The size distribution of Type S.H particles was 0.41 ± 0.03 mm, and the size distribution of Type L.H particles was 1.89 ± 0.06 mm. Type M.H particles were sieved with a 1.12 mm sieve to produce particles of two size distributions: Type M.H(a) particles with a size distribution of 1.19 ± 0.04 mm and Type M.H(b) particles with a size distribution of 1.08 ± 0.04 mm. Type M.H(b) particles were used in **Figure** 10 (d)(iii). For a comparison, another set of "heavy" particles with a reduced density was purchased from Silibeads. These ceramic particles had a density of 4000 kg/m^3. The size range of these Type M.Hr particles was 1.2-1.4 mm with an optically determined size distribution of 1.31 ± 0.05 mm.

c. Determination of Minimum Fluidization Velocity

The minimum fluidization velocity was determined by vigorously fluidizing the bed under vibrating conditions and then slowly decreasing the gas flow rate over time while measuring the pressure drop across the bed. A pressure probe flush with the side wall was placed at the bottom of the bed to measure the pressure drop across the bed. The minimum fluidization velocity, U_{mf}, was determined from the "fluidization curve" of the pressure drop (ΔP) normalized by the weight of the particles in the bed (W) per unit horizontal cross sectional area of the bed (A_{bed}) versus superficial gas velocity, U (volumetric flow rate divided by the horizontal cross-sectional area of the bed). A linear regression was calculated through the linear portion of the graph between normalized pressure drops of 0.5 and 0.75. U_{mf} was determined based on the value of U at which the linear regression matched a normalized pressure drop of 1.0. **Figure 16** shows the fluidization curve for the case of the Type M.L particles at vibration conditions of amplitude A = 0.05 mm and frequency f = 30 Hz. The minimum fluidization velocities under non-vibrating and vibrating conditions for the different particle types used are shown in **Table 1**.

d. Determination of Granular Fingering Regime Maps

To create **Figure 10** (E), particles were arranged in an R-T configuration, and a prescribed vibration amplitude and frequency were applied. The superficial gas velocity was increased slowly until fingers began to form, marking the delineation between the "no interfacial motion" and "granular fingering" regimes. The gas velocity was increased further until gas bubbles began moving through the system, demarcating the dividing point for the "granular fingering" and "gas bubbling" regimes. **Figure 10** (E) used the same particles as in **Figure 9** and a vibration frequency of 30 Hz; different vibration strengths were achieved in different experiments by changing the amplitude of vibrations. **Figure 18** used particles of different sizes, and some experiments varied the vibration frequency while others varied the vibration amplitude as indicated in the figure legend and caption.

e. Optical Imaging

Optical images were taken of the vibrofluidized bed through the front wall using a high speed CCD camera (Photron Fastcam SA Z). Images were taken at a frame rate of 50 images per second. Images were acquired for up to 30 minutes to see the full range of motion induced by vibration and gas flow at specified conditions.

f. Image Processing

Optical images were processed using Matlab. A threshold was applied to the light signal from the images to determine heavy particles from light particles in the granular "bubble" experiments. The position of the uppermost part of the bubble was determined as the position of the uppermost pixel in the interconnected pixels of light particles. This position was tracked over successive frames to determine the uppermost position of the bubble over time. A plot of position versus time, as shown in **Figure 13**, was made and the slope of a linear regression through the points was used to determine the rise velocity of the bubble.

Particle image velocimetry (PIV) was used to produce **Figure 15**. To do this, heavy particles were colored white, while the majority of light particles were colored black with 10 % of light particles colored white. The displacement of the patterns created by white particles mixed in the black particles was tracked between successive images to assess the particle velocities. The particle velocities were calculated using the MAT- PIV 1.6.1 software. The size of the PIV interrogation window was iteratively reduced from 64 × 64 to 32 × 32 pixels, using four iterations. Once the velocities were determined, a signal-to-noise filter (s/n =1.3) and global and local mean filters were applied to detect outliers [41]. The particle velocities were then calculated between every two successive frames taken at 2.5 Hz. The snapshots in **Figure 15** were made by averaging together the particle velocities calculated between two individual frames for a succession of 9 frames. The particle velocities are then overlaid onto the middle frame of each snapshot. The resulting snapshots are the average particle velocities over 3.4 seconds.

g. Numerical Simulation

The numerical simulation was conducted using CFD-DEM (Computational Fluid Dynamics – Discrete Element Method) [42], in which molecular dynamics involving contact forces between particles are used to track the motion of each particle. The motion of particles is governed by Newton's laws of motion. The gas phase is modeled using computational fluid dynamics with volume-averaged equations [43] to account for the void fraction of particles, and the coupling between gas and particles is accounted for using buoyant force and a drag law [44]. The simulation was conducted with $U = 0.9$ m/s and vibration conditions with an amplitude of 0.5 mm and a frequency of 10 Hz. Vibration was modeled by oscillating the gravitational force, rather than physically moving the bottom plate. The fluid grid size was 5 mm (horizontal) by 5 mm (vertical) by 5 mm (depth). The dimensions of the bed were identical to those of the experimental bed. The simulation was run for 15 s. The time step for the particles was 5×10^{-6} s and the time step for the gas phase was 2.5×10^{-4} s. For both particle types, the coefficient of restitution was 0.66, the coefficient of friction was 0.4 and the Poisson ratio was 0.22. The gas had a kinematic viscosity of 1.8×10^{-5} Pa s and a density of 1.2 kg/m^3. The light particles had a diameter of 1.7 mm and a density of 2500 kg/m^3. The heavy particles had a diameter of 1.1 mm and a density of 6000 kg/m^3. The particle position, gas velocity, drag force on particles and net contact force on particles was output to create **Figure 11**. A separate simulation was run using the same protocol, except the coefficient of friction was set to zero to turn off interparticle friction in the simulation.

Table 1 Properties and minimum fluidization velocities of the particles used.

Particle Type	Diameter (mm)	Density (kg/m^3)	Geldart Group	U_{mf} (m/s)	U_{mf} vibrated (m/s)	Vibration Frequency (Hz)	Vibration Amplitude (mm)
S.L	0.61 ± 0.06	2500	B/D	0.29	0.23	30	0.05
S.H	0.41 ± 0.03	6000	B/D	0.29	0.21	30	0.05
M.L	1.70 ± 0.07	2500	D	1.08	0.84	30	0.05
M.H	1.17 ± 0.06	6000	D	1.00	0.87	30	0.05
M.Hr	1.31 ± 0.05	4000	D	1.02	0.88	30	0.05
L.L	2.75 ± 0.13	2500	D	1.75	1.37	30	0.05
L.H	1.89 ± 0.06	6000	D	1.77	1.50	30	0.05
M.L(b)	1.64 ± 0.05	2500	D	1.03	0.79	30	0.05
M.H(b)	1.08 ± 0.04	6000	D	0.99	0.85	30	0.05

5.5 Results and Discussion

Figure 9 reveals that when light particles are placed below heavy particles in the system and vibration and gas flow are initiated, an R-T-like instability is observed, with "granular bubbles" of less dense particles pinching off from "fingers" and rising to the surface, until a complete inversion and segregation of particles is reached. We define "granular bubbles" as locally concentrated ensembles of light particles surrounded by heavy particles through which the granular bubbles rise. **Figure 10** shows that this R-T-like instability is not limited to the conditions in **Figure 9**, but rather persists across different particle sizes, vibration conditions, and ratios of minimum fluidization velocity for the heavy and light particles ($U_{mf,H}/U_{mf,L}$). **Figure 10** further shows that the size and growth rate of the fingers increases with increasing gas flow rate, vibration strength and particle size. Experiments with only gas flow or only vibration were unable to produce the phenomenon (see **Figure 17**) and **Figure 10** (E) shows that the window of gas velocities which enables fingering without gas bubbling increases with increasing vibration strength.

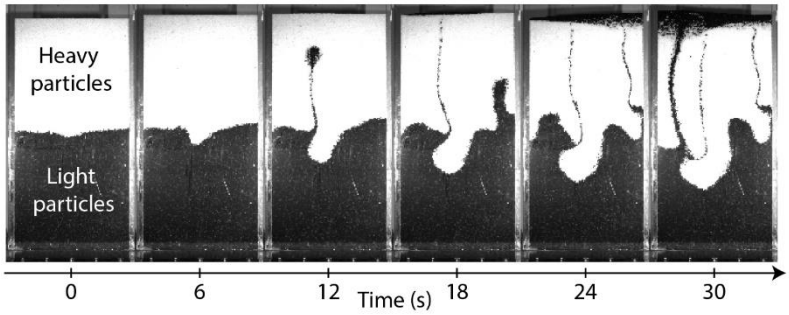

Figure 9 Time series of optical images of the R-T instability forming after denser particles are placed initially above lighter particles. Diameter of light particles: d_L = 1.70 ± 0.15 mm; density of light particles: ρ_L = 2500 kg/m3; ratio of heavy-to-light particle diameters and densities: d_H/d_L = 0.65 ± 0.10, ρ_H/ρ_L = 2.40; Geldart (38) grouping of both types of particles: Group D; vibration frequency: ω = 188 rad/s; vibration strength: $\Gamma = \frac{A\omega^2}{g} = 0.18$, where A is the amplitude of the vibration; height, width and depth of the cell: H/d_L = 235; W/d_L = 118; D/d_L = 4.7; gas: humid air at ambient conditions, density: ρ_g = 1.19 kg/m3, viscosity: η_g = 1.8 Pa s; minimum superficial gas velocity needed to suspend the particles at these vibration conditions for light and heavy particles: $U_{mf,L}$ = 0.84 m/s, $U_{mf,H}/U_{mf,L}$ = 1.03; superficial gas velocity: $U/U_{mf,L}$ = 1.17.

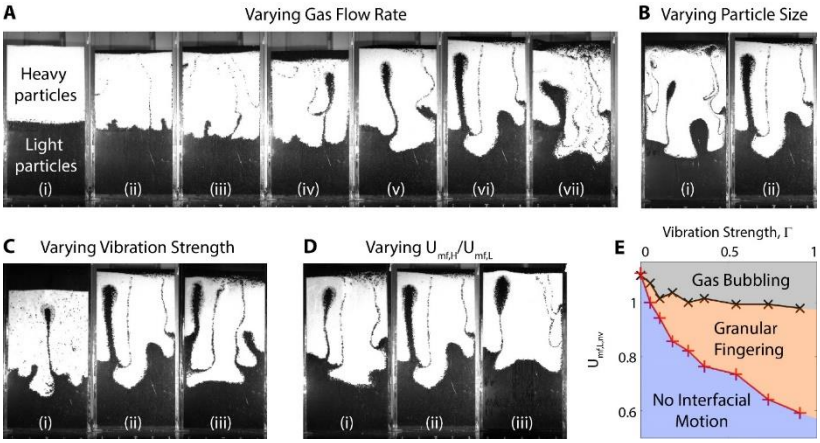

Figure 10 Structures formed for R-T experiments under different flow conditions: (A) varying gas flow rate, (B) varying particle size, (C) varying vibration strength, (D) varying ratio of minimum suspension velocities of the two particles ($U_{mf,H}/U_{mf,L}$). Differences in experimental conditions from Figure 9: (A): $U/U_{mf,L}$: (i) 0.88, (ii) 0.94, (iii) 1.00, (iv) 1.05, (v) 1.11, (vi) 1.17, (vii) 1.35; (B): (i) dL = 0.63 ± 0.12 mm, d_H/d_L = 0.71 ± 0.13; Geldart (38) grouping of both sets of particles: Group B/D border (C): (i) $\Gamma = 0.09$, (iii) $\Gamma = 0.36$; (D): (i) d_H/d_L = 0.68 ± 0.10, $U_{mf,H}/U_{mf,L}$ = 1.10, (iii) d_H/d_L = 0.62 ± 0.10, $U_{mf,H}/U_{mf,L}$ = 0.98. (E) shows a regime map for gas bubbling occurring, granular fingering occurring without gas bubbles and no interfacial motion as a function of vibration strength and the ratio of superficial velocity to $U_{mf,L,nv}$, the value of U_{mf} of the light particles without vibration.

The conventional R-T instability involves buoyancy acting as a driving force for inversion and surface tension acting as a stabilizing force for the interface, resulting in the formation of fingers of a characteristic wavelength or width. The mechanism driving the formation of these structures in fluidized grains is perplexing because the grains are suspended by gas flow and have no significant cohesive forces to create surface tension. The phenomenon can be explained as follows: Buoyancy drives the inversion, since the two particle-gas mixtures have different bulk densities. This difference in bulk density has been used to describe a homogeneous "layer inversion" in particles suspended by upward liquid flow [39] as well as wavy deformation structures in liquid-saturated sediments subject to vibration [27]. Initially, a high effective "viscosity" of the grains acts to stabilize the interface, leading to perturbations of a characteristic wavelength forming instead of a homogeneous inversion. Particle-phase viscosity arises due to interparticle friction and has been used to explain finger formation when granular particles sediment in a liquid [45], a process which also lacks surface tension. The wavelength producing the maximal finger growth rate predicted by viscous potential flow theory for viscous fluids with no surface tension [45] is given by $\lambda = 2\pi\left(\frac{8(\eta_H+\eta_L)^2}{g(\rho_{B,H}^2-\rho_{B,L}^2)}\right)^{1/3}$ where g is the acceleration due to gravity. Assuming a viscosity of $\eta \sim 1$ Pa s for both sets of fluidized particles [25] and using the bulk densities of both particle/air mixtures ($\rho_{B,H}, \rho_{B,L}$) gives a wavelength of λ ~40 mm, which is in-line with the width of perturbations which develop into fingers in **Figure 9**. Thus, the competition between buoyant and viscous forces describes the initial formation of fingers in the model binary granular system. The ratio of gas flow rate to the minimum fluidization velocity (U/U_{mf}) is also key to the formation of these perturbations because gas flow is needed to suspend the particles, enabling them to act like a mobile viscous fluid, rather than a stationary solid. The regime map in **Figure 10** (E) shows that vibration strength is another key dimensionless group for characterizing this phenomenon because vibration is needed to lower the gas velocity at which the particles become suspended, allowing fingers to form without the presence of gas bubbles. **Figure 18** shows that U/U_{mf} and the normalized vibration strength Γ are the appropriate non-dimensional parameters for describing the excitation mechanisms necessary for the R-T-like phenomenon, since these two parameters collapse data for the fingering regime map across different particle sizes and vibration conditions.

While these mechanisms and non-dimensional groups properly describe the initial perturbation of the interface, they do not fully describe the behavior of fingers after the initial formation stage. The fact that the description is incomplete is demonstrated by the trend that finger width increases with gas velocity, as shown in **Figure 10** (A). The effective viscosity of the suspended particles decreases with increasing gas flow rate due to a decrease in the number of interparticle contacts. Thus, the wavelength equation given earlier predicts a decrease in wavelength with increasing gas velocity, yet developed fingers are wider at higher gas velocities.

To uncover the missing physics underlying this R-T-like phenomenon after the initial perturbation stage, we simulate a system with the same size and particle properties as in the experiments in **Figure 9** and **Figure 10** using a numerical model which couples gas and particle motion [42]. **Figure 11** shows that there is a competition between a net buoyant force pushing light particles at the interface up, while a net contact force pushes them down. Due to the gas flow and vibrations, small amplitude waves are able to form at the interface, and the width of these perturbations which grow into fingers is approximately 40 mm, consistent with those observed experimentally. Upon formation of these wavy perturbations, the drag force acting on particles at the crest of a wave increases dramatically, causing the wave to grow into a finger and ultimately pinch off as a granular bubble. This increase in drag force occurs due to gas channeling through the light particles (second column of **Figure 11**) because they are larger than the heavy particles, and thus have a higher permeability to gas flow [46], $k \propto d^3$. Such gas channeling has been used to explain vertical band structures forming in binary gas-fluidized systems with different particle size, but of the same particle density [26]. With an increasing gas flow rate, more gas can channel through wider waves, allowing wider fingers to form and grow, explaining the trend seen in **Figure 10** (A) and distinguishing the instability from that seen in conventional fluids. The ratio of gas velocity through fingers and surrounding heavy particles will be equal to the ratio of gas permeability between the two types of grains $(\frac{u_L}{u_H} = \frac{k_L}{k_H})$(25), which scales with the ratio of particle diameters $k_L/k_H \propto \left(\frac{d_L}{d_H}\right)^3$. Importantly, when the same simulation was run, but with interparticle friction turned off, large gas bubbles appeared which caused particle motion which was very different from the R-T-like instability, demonstrating the importance of interparticle friction and thus effective viscosity on the formation of granular fingers.

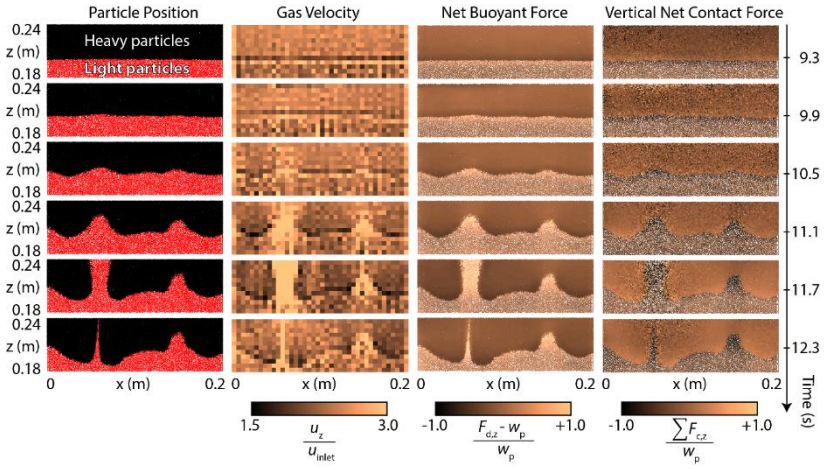

Figure 11 Numerical simulation results near the interface for the Rayleigh-Taylor configuration. Each dot corresponds to an individual particle. The system size is the same as that used experimentally in Fig. 1, but the images zoom in on the interface to provide more detail. Rows show progression over time. The first column shows the positions of particle types. The second column shows the vertical component of gas velocity normalized by the inlet gas velocity. The third column shows the net buoyant force determined by the sum of the vertical component of drag, $F_{d,z}$, and gravitational, $F_{g,z} = -w_p$, forces normalized by particle weight, w_p. The fourth column shows the sum of frictional and normal contact forces, $\sum F_{c,z}$, in the vertical direction on each particle normalized by the particle weight. Diameter of light particles: d_L = 1.70 mm; density of light particles: ρ_L = 2500 kg/m^3; ratio of heavy-to-light particle diameters and densities: d_H/d_L = 0.65, ρ_H/ρ_L = 2.40; Geldart (38) grouping of both sets of particles: Group D; vibration frequency: ω = 63 rad/s; vibration strength: Γ =0.20; height, width and depth of the cell: H/d_L = 235; W/d_L = 118; D/d_L = 5.8; gas density: ρ_g = 1.2 kg/m^3, gas viscosity: η_g = 1.8 Pa s; ratio of minimum suspension superficial velocities: $U_{mf,H}/U_{mf,L}$ = 1.10; superficial gas velocity: $U/U_{mf,L}$ = 1.25.

Figure 12 shows how differences in bulk density and permeability between light and heavy particles lead to a variety of other interesting instabilities under the same gas flow and vibration conditions. When a "granular bubble" of light particles is surrounded by a sea of heavy particles (**Figure 12** (A)), gas channeling through the light particles causes them to rise together as a bubble to the top, leaving behind a trail of particles due to the lack of surface tension. **Figure 14** (A) shows that the rise velocity increases with granular bubble diameter, but it does not follow the correlation $u_b \propto D_b^{1/2}$ observed in classic fluids and gas bubbles in fluidized grains [47]. Additionally, the rise velocity also increases monotonically with superficial gas velocity (**Figure 14** (B)), further emphasizing the deviation from traditional fluid flow. This monotonic increase deviates from the non-monotonic change in rise velocity of an intruder particle with increasing gas velocity in a bed of vibrated granular material [48]. Since the R-T-like phenomenon and the granular bubble rise phenomenon have the same underlying mechanisms, the trends and governing parameters for granular bubble rise are expected to be the same between both phenomena.

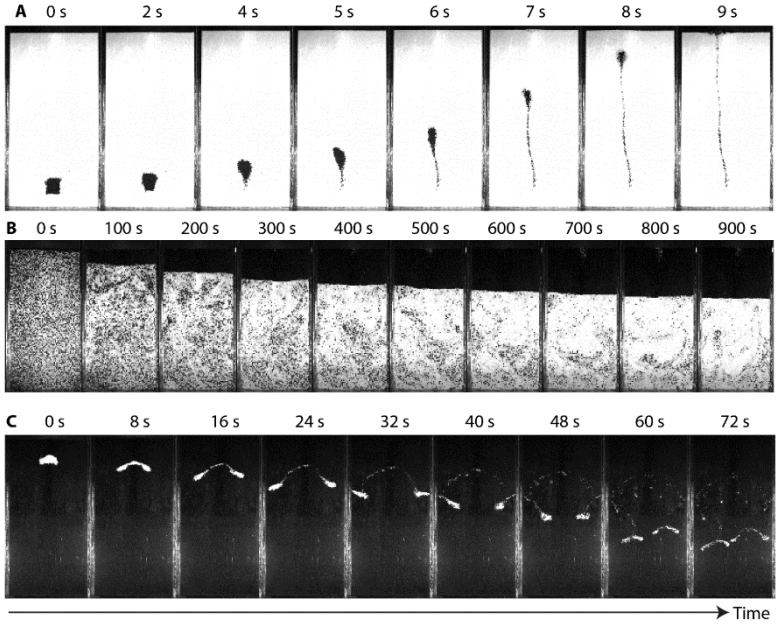

Figure 12 Optical images of instabilities in suspended granular flows in three configurations: (A) a "granular bubble" of lighter particles below a sea of denser particles, (B) a homogenous mix of denser and lighter particles and (C) a "droplet" of denser particles above a sea of lighter particles. Other than the initial configuration of particles, the conditions are identical to those in Figure 9.

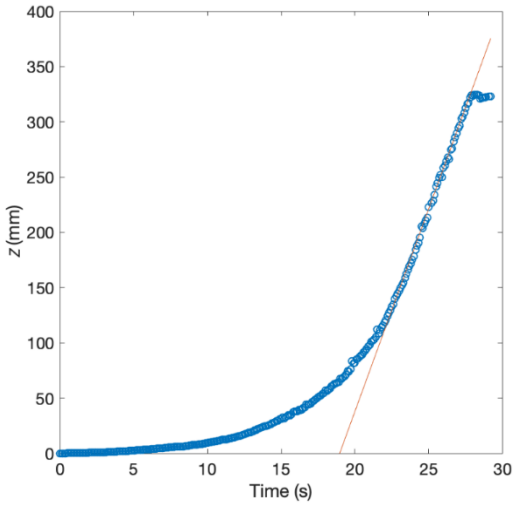

Figure 13 Position of the uppermost point in the bubble versus time for the granular bubble shown in Figure 4 (A) with Types M.L and M.H particles, $U/U_{mf,L}$ = 1.03, f = 30 Hz, A = 0.05 mm and L_b = 30 mm. The diagonal line is a linear regression through the data during bubble rise, and the slope of this line is used to determine the bubble rise velocity.

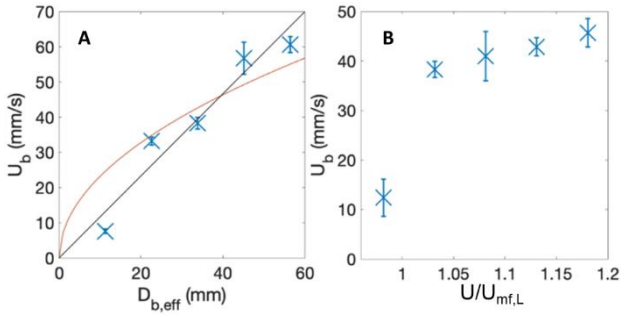

Figure 14 Bubble rise velocity (u_b) versus (A) the effective bubble diameter ($D_{b,eff}$), which is calculated using $D_{b,eff} = L_b\sqrt{\frac{4}{\pi}}$, where L_b is the side length of the initial square of light particles at $U/U_{mf,L}$ = 1.03 and (B) normalized superficial gas velocity ($U/U_{mf,L}$) with $D_{b,eff}$ = 34 mm. For both (A) and (B), the same particles and vibration conditions as in Fig. 4 were used. Error bars show the standard deviation from three repetitions of each experiment. The lines show least square regressions through the data: the black line is a linear fit and the orange line is a square root fit.

Table 2 demonstrates that the rise velocity of a granular bubble increases with increasing density ratio and decreasing diameter ratio. This result affirms that increased buoyant driving force and increased gas channeling due to increased permeability ratio lead to increased upwelling rates of granular bubbles and granular fingers. Varying particle size has a non-monotonic effect on granular bubble rise velocity, demonstrating the complexity of the phenomenon.

Table 2 Rise velocity of granular bubbles with different particles, vibration frequency of 30 Hz, vibration strength of $\Gamma = 0.18$, $U/U_{mf,L} = 1.13$ under these vibration conditions and a light particle density of $\rho_L = 2500$.

Light Particle Diameter (d_L)	Diameter Ratio (d_H/d_L)	Density Ratio (ρ_H/ρ_L)	Granular Bubble Rise Velocity (mm/s)
0.61 ± 0.06	0.67 ± 0.06	2.40	13.0 ± 2.7
1.70 ± 0.07	0.69 ± 0.03	2.40	42.9 ± 1.9
2.75 ± 0.13	0.69 ± 0.04	2.40	11.0 ± 3.4
1.70 ± 0.07	0.77 ± 0.04	1.60	4.5 ± 1.1

When the heavy and light particles are initially mixed (Figure 12 (B)), light particles ultimately reach the top due to buoyancy. During segregation, finger- and granular bubble-like structures form because gas channels through regions with a higher concentration of light particles, causing these regions to rise and further increase in concentration of light particles as they rise.

When a "droplet" of heavy particles is surrounded by a sea of light particles (Figure 12 (C)) the droplet does not fall straight to the bottom as in immiscible fluids, but rather it immediately splits into two daughter droplets which fall on an angle through the light particles and undergo subsequent binary splitting events. The observed binary splitting of granular droplets exhibits striking similarity to the bifurcations of falling dye droplets in miscible fluids [46, 47, 70 – 72]. However, the physical mechanisms behind these two phenomena are different. When a droplet of dye is placed in a miscible fluid, it forms a vortex ring. This ring becomes unstable and fragments into smaller droplets which undergo the same instability and may fragment again [49]. The Rayleigh-Taylor instability is suspected to cause the fragmentation of the vortex ring [71, 72]. The mechanism underlying the granular binary splitting reported here can be explained as follows: gas channels around the granular droplet because of the lower permeability of the heavy particles. The lack of gas flow to suspend the light particles just below the granular droplet causes a region below the droplet to solidify, or become stationary, due to force chains under the weight of the droplet. The solidification of particles below the droplet is confirmed experimentally using particle image velocimetry [50] in Figure 15. The droplet cannot fall through these solidified particles, but it still can descend through the suspended particles, and thus it splits and falls at an angle through the suspended light particles just above the solidified particles. At a certain point, a solidified region forms just below the daughter droplets for the same reason of gas channeling, and thus they undergo a subsequent splitting event. Thus, the mechanism of gas channeling and solidification of particles makes this branching phenomenon distinct from that observed in conventional miscible fluids.

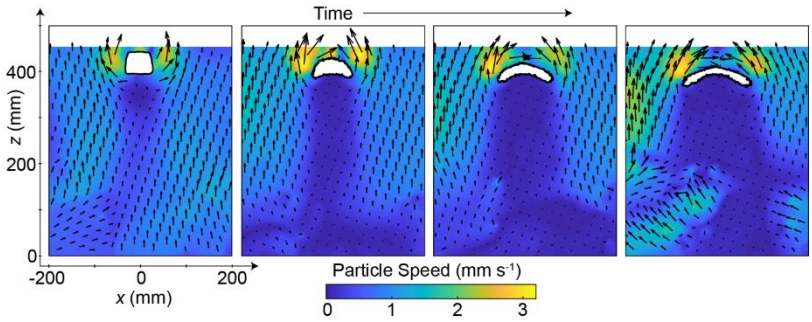

Figure 15 Particle image velocimetry images of the velocity field of light particles surrounding heavy particles under the same fluidization and vibration conditions as in Figure 12 (C). The white region surrounded by black lines demarcates the "granular droplet" of heavy particles.

Thus, the combination of gas channeling and differences in bulk density provides a mechanistic explanation of the physics underlying heterogeneous flow behavior observed in the newly discovered gravitational instabilities in suspended binary granular flows reported here. Due to similarities and differences in governing physics, the resulting patterns sometimes mimic those observed in conventional fluids, but have different underlying mechanisms.

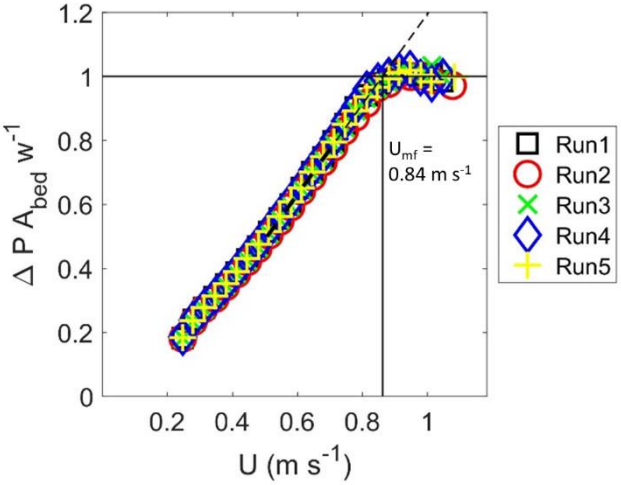

Figure 16 Fluidization curve for the case of the Type M.L particles at vibration conditions of amplitude A = 0.05 mm and frequency f = 30 Hz. The horizontal line marks a normalized pressure drop of 1.0, and the diagonal line marks the linear regression to the fluidization curve. The vertical line marks the superficial velocity at the meeting of the horizontal and diagonal lines, which marks the minimum fluidization velocity.

5.5.1 Behavior with Only Vibration or Gas Flow

Figure 17 (a) shows time series of images of heavy and light particles in the same initial setup as **Figure 9** (a), but with only vibration and no upward gas flow. The vibration conditions were A = 0.25 mm and f = 30 Hz. Without gas flow to suspend the particles, frictional contacts prevent the particles from flowing and the interface does not move.

Figure 17 (b) shows a time series of images of a layer of light particles below a layer of heavy particles with a slight upward tilt at the right side of the interface. Without any vibration, no motion occurs until the gas flow is brought to $U = 1.08\ U_{mf,L}$. At this point, the gas channels through the right side of the interface due to the higher permeability of the larger light particles. Gas bubbles rise through the heavy particles on the right hand side of the bed, and over the course of several seconds, a granular bubble of light particles rises to the top of the system. The granular bubble leaves a trail of light particles behind it, and gas channels through this trail with gas bubbles continuing to form surrounding it. After the rise of the initial granular bubble, the interface between the heavy and light particles does not move anymore.

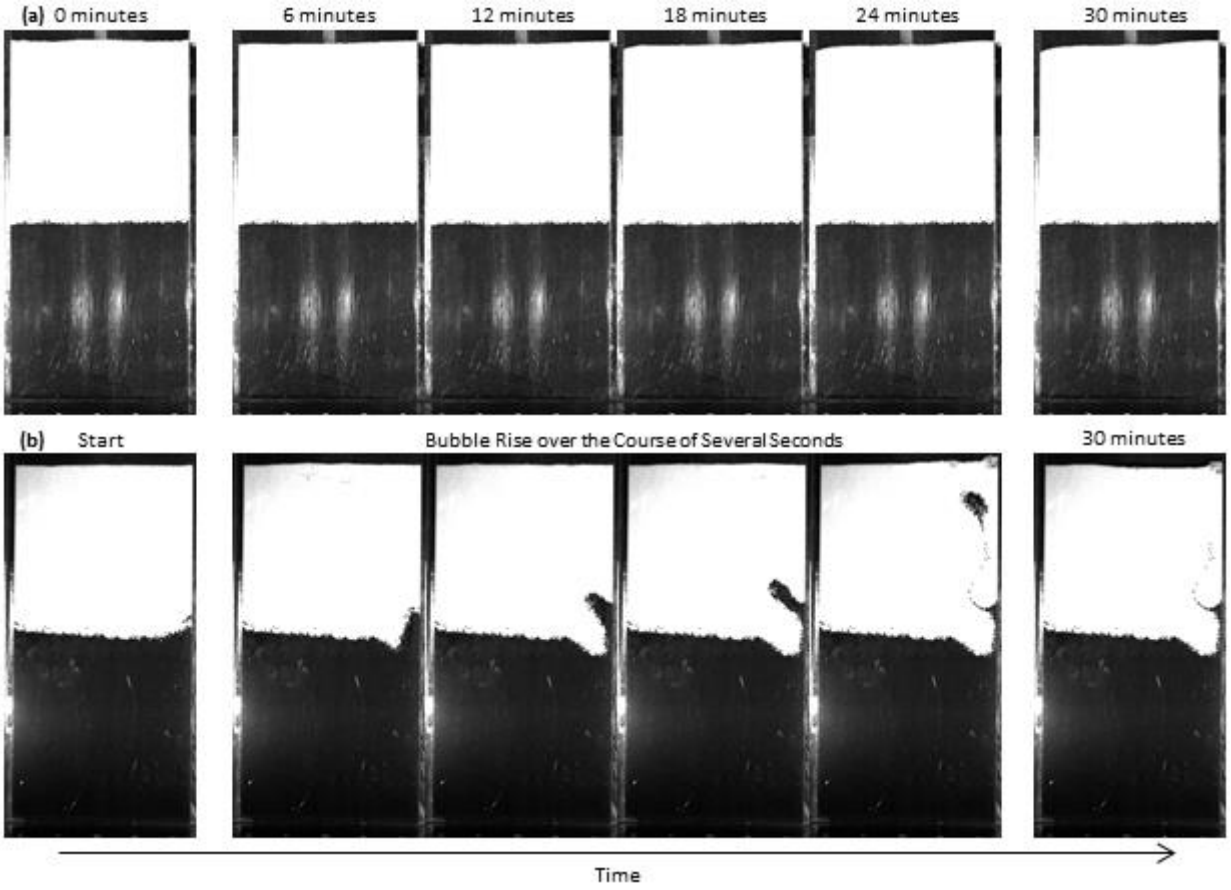

Figure 17 Time series of images of Type M.L particles (black) below Type M.H particles (white) with (a) no gas flow and vibration conditions $A = 0.25$ mm and $f = 50$ Hz and (b) no vibration and gas flow at $U/U_{mf,L,nv} = 1.08$.

h. Granular Fingering Regime Maps

Figure 18 shows the effects of (a) varying particle size and density and (b) varying the vibration frequency or vibration amplitude to achieve different vibration strengths on the granular fingering regime map based on $U/U_{mf,L,nv}$ and vibration strength. Results show that $U/U_{mf,L,nv}$ and vibration strength can collapse data for the onset of granular fingering and gas bubbling across particle properties and vibration conditions, validating their use as dimensionless parameters for characterizing the granular fingering phenomenon reported here. At high values of vibration strength, there is a significant difference for the onset of granular fingering based on constant frequency versus constant amplitude vibration conditions, indicating that other factors must be included in non-dimensionalization. We leave the determination of these factors for future work.

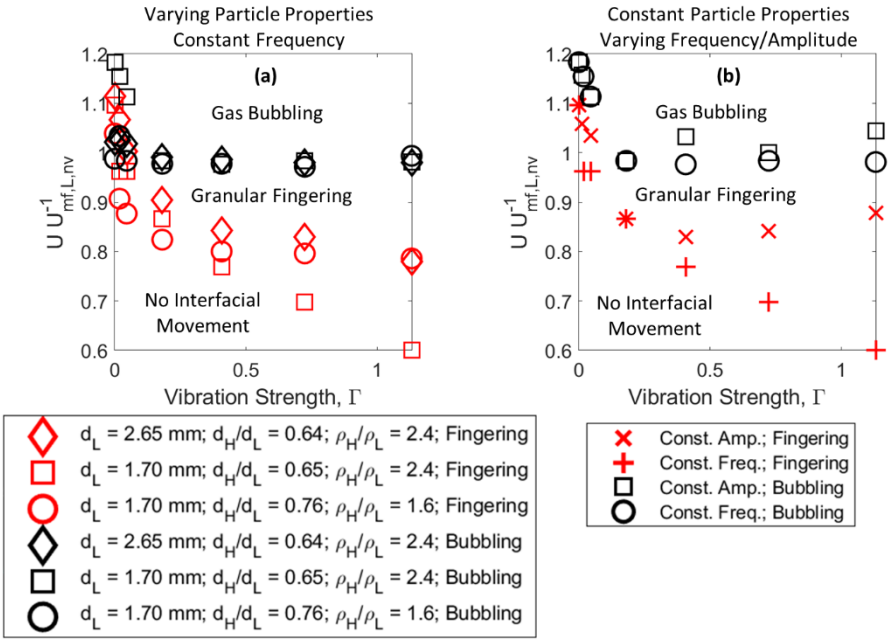

Figure 18 Regime map of R-T behavior: (i) no interfacial movement, (ii) granular fingering, (iii) gas bubbling, based on U/U_{mf} with U_{mf} based on the U_{mf} of the light particles under non-vibrating conditions ($U_{mf,L,nv}$) and vibration strength with (a) varying particle sizes and densities and (b) varying modes for varying vibration strength (amplitude or frequency).

6 Reduction in Minimum Fluidization Velocity and Minimum Bubbling Velocity in Gas-Solid Fluidized Beds due to Vibration

Adapted from: McLaren, C. P., Metzger, J. P., Boyce, C. M., & Müller, C. R. (2021). Reduction in minimum fluidization velocity and minimum bubbling velocity in gas-solid fluidized beds due to vibration. Powder Technology, 382, 566-572.

6.1 Abstract

Vibration of gas-solid fluidized beds is often used to enable fluidization of cohesive particles; however, it has also been shown to reduce the minimum fluidization velocity (U_{mf}). Here, we show via experiments that vibration can reduce both U_{mf} and the minimum bubbling velocity (U_{mb}) in Geldart Group B and D particles. We observe that U_{mf} is reduced more than U_{mb}, thereby creating a densely packed, bubble-free fluidization state when the superficial gas velocity is in between U_{mf} and U_{mb}. U_{mf} and U_{mb} decrease with increasing vibration frequency and amplitude and the results for U_{mf} and U_{mb} across a variety of vibration conditions could be plotted along a single curve when plotted versus vibration strength, i.e. the ratio of peak vibration acceleration to gravitational acceleration. U_{mf} and U_{mb} increase when moving from a 3D cylindrical system to a pseudo-2D system. Changes in U_{mf} and U_{mb} due to vibration are not affected significantly by changing particle density, but these changes are affected in a non-monotonic way by changing particle diameter.

6.2 Introduction

Gas-fluidization is used in a variety of industrial processes to induce motion of granular particles when superficial gas velocity (U) is raised above the minimum fluidization velocity (U_{mf}). Further particle convection is induced by gas voids or "bubbles" rising through the particles, which occurs when U is greater than the minimum bubbling velocity (U_{mb}). For Geldart Group B (particle diameter, d_p ~ 100-800 μm) and D ($d_p \gtrsim 800$ μm) particles, $U_{mf} \approx U_{mb}$ [51], and thus there is no significant range of gas velocities for which particles can mix without gas bubbles forming. Bubbles in fluidized beds can diminish gas-solid contact as compared to fixed beds. Geldart Group A (d_p ~ 20-100 μm) particles have $U_{mf} < U_{mb}$ [51], and when $U_{mf} < U < U_{mb}$, a homogenous fluidization state forms in which the bed volume expands, producing a higher void fraction state with decreased gas-solid contact as compared to a fixed bed state. Geldart Group C ($d_p \lesssim 20$ μm) particles are difficult to fluidize due to cohesive interparticle forces [51].

Vertically vibrating gas-fluidized beds have long been used to enable fluidization of Group C particles via vibrational forces breaking up cohesive forces [52]. Studies have also shown that vibration can reduce the U_{mf} in Group C and A particles [53] as well as Group B and D particles [54]. A prior study [55] has accounted for the decrease in U_{mf} in Group C and A particles (which allow for bed expansion) based on an decrease in bed void fraction at U_{mf} with increasing vibration strength, $A(2\pi f)^2/g$ where A and f are vibration amplitude and frequency, respectively, and g is gravitational acceleration. For Group B and D particles (which do not allow for bed expansion), prior work has shown that the pressure drop needed to fluidize particles reduces when $\Gamma > 1$, causing a reduction in U_{mf} due to vibration [54] Although most studies use only the vibration strength to quantify the influence of vibration, this approach might be an over-simplification because different combinations of frequency and amplitude can result in the same vibration strength but have very different effects on fluidization [79, 80].

Recently, the authors and co-workers have reported that fluid-like gravitational instabilities can form in Group B and D granular particles of different densities subject to combined gas flow and vibration ($\Gamma < 1$) [56]. These gravitational instabilities formed in a fluidized state in which particles could move and mix, while bubbles did not form and the bed volume did not expand significantly [56], avoiding issues with reduction in gas-solid contact seen in conventional homogeneous and bubbling fluidized beds. Here, we investigate the changes in U_{mf} and U_{mb} induced in Group B and D particles by vibration with $\Gamma \lesssim 1$ in order to shed light on the conditions necessary to produce a bubble-free, densely packed fluidizations state.

The minimum fluidization velocity necessary to "unlock" the particles and bring a packed bed to a fluidized bed is higher than the minimum fluidization velocity, $U_{mf,}$ when starting from a fluidized bed and lowering the gas velocity until the bed is no longer fluidized [57, 58] At higher gas velocities a hysteresis in the jet–spout transition in packed beds can also be seen, the jet height while decreasing the gas velocity is higher than the jet height during an increase in the gas velocity [59]. A similar hysteresis could occur in vibro-fluidized beds; a packed bed that has been fluidized at the minimum velocity by help of vibration may stay in fluidized state, even once the vibration is removed although the bed would not have fluidized without this activating vibration [14]. In this work the U_{mf} is only determined by starting with a fluidized bed and lowering the gas velocity, and therefore hysteresis is not examined.

6.3 Experimental

Two gas-solid fluidized beds were used: (i) a pseudo-2D fluidized bed and (ii) a 3D cylindrical fluidized bed. Both beds were made of polymethyl methacrylate (PMMA); the pseudo-2D bed had a width of 200 mm, a height of 500 mm and a depth of 10mm, while the cylindrical fluidized bed had an inner diameter of 74 mm and a height of 300 mm. In all experiments, the bed was filled to a height of 120 mm with particles. The beds were vibrated using a Labworks shaker (Labworks Inc., ET-139), which generated a vertical sinusoidal displacement, $\delta = A \sin(2\pi f t)$, using a controller (Labworks Inc. VL-144), an amplifier (Labworks Inc., PA-138-1) and an

accelerometer (PCB Piezotronics Inc., J352C33). The amplitude and frequency were inputted as the parameters of the shaker via Vibelab. To determine U_{mf}, the gas velocity was slowly decreased over time while monitoring the pressure at the base of the bed. The gas velocity was controlled using a F-203AV, Bronkhorst mass flow controller and the pressure was monitored using a pressure probe; the two were monitored together using a LabView interface. The pressure probe is a Honeywell 40PC001B1A pressure sensor placed 1mm above the distributor. **Figure 19** shows how U_{mf} was determined for (a) a non-vibrated case and (b) a vibrated case by matching a linear fit through the curve, between normalized pressure drops of 0.5-0.8 to a normalized pressure drop of 1.0 in the de-fluidization curve. The recorded pressure was normalized by the weight of the particles per unit cross-sectional area. U_{mp} was determined by careful visual observation of bubbles in the de-fluidization experiments to determine the gas velocity below which bubbles were no longer observed. The top of the bed was zoomed in upon using a high speed CCD camera (Photron Fastcam SA Z.) The airflow was lowered at a rate of 0.25 % of the estimated U_{mb} per second. Three runs were taken for each U_{mb}. An average standard deviation of 2 % between runs was found, showing a high reproducibility. Spherical particles were used; particle details are shown in **Table 3**. After passing through the mass flow controller, the air passed through a humidifier to ensure a constant relative humidity of 87-91 % in the air and to keep electrostatic forces from building up on the surfaces of the particles. The humidity of the air was measured exiting the humidifier by a Sensirion SHT31 sensor. The calculated density change due to humidity is less than 1 %. No signatures of liquid bridging were observed. The void fractions were calculated by measuring the height of the bed using the high-speed camera. The air enters the 2D bed through a distributor with 20 holes of 1.1 mm diameter spaced evenly apart and the 3D bed through a distributer with 42 holes of 1.1 mm spaced evenly apart. The choice of distributor effects the formation of bubbles within a fluidized bed The choice of distributor effects the formation of bubbles within a fluidized bed [18, 85]. For a perforated plate distributor, as used in this study, air enters the bed in the form of jets before breaking up into bubbles. As we concentrate on the surface of the fluidized bed to identify the onset of bubbling, we believe the exact specification of the distributor plate does not affect appreciably the onset of bubbling.

Table 3 Particle properties: Properties and minimum fluidization velocities of the particles used.

Particle Diameter Range (mm)	Particle Density (kg/m^3)	Geldart Group	$U_{mf,nv}$ (m/s)	Particle Material
1.55-1.85	2500	D	0.86	Glass
1-1.3	2500	D	0.54	Glass
0.5-0.75	2500	B/D	0.26	Glass
0.4-0.6	2500	B	0.17	Glass
0.25-0.5	2500	B	0.11	Glass
1-1.2	4100	D	0.72	Zirconium Silicate
0.4-0.6	4100	B/D	0.31	Zirconium Silicate
1-1.2	6000	D	0.89	Zirconium Oxide
0.6-0.8	6000	D	0.48	Zirconium Oxide
0.4-0.6	6000	D	0.34	Zirconium Oxide

6.4 Results and Discussion

Figure 19 shows how U_{mf} decreases in a vibrated bed as compared to a non-vibrated bed; however, the shape of the de-fluidization curves stays generally the same and the pressure drop when fluidized is the same, unlike the trends seen for vibrated fluidized beds with $\Gamma > 1$ reported previously [54]. Thus, we do not attribute the decreases in U_{mf} due to vibration with $\Gamma < 1$ to vibration causing the pressure drop needed to fluidize the bed to decrease. Further, inspection of the fluidized bed during vibration did not show significant bed expansion or compaction, and thus we do not attribute the decrease in U_{mf} to a decrease in void fraction at minimum fluidization.

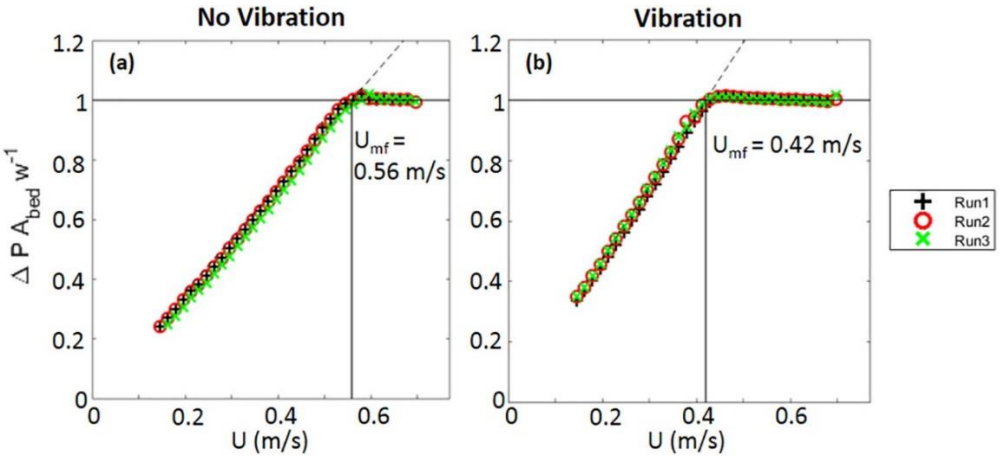

Figure 19 De-fluidization curves (pressure drop normalized by bed weight per unit cross sectional area vs. superficial gas velocity as gas velocity is reduced gradually) used to evaluate U_{mf} under (a) non-vibrated and (b) vibrated (A = 0.05 mm, f = 30 Hz, Γ = 0.18) gas-fluidization conditions. Each experiment was run 3 times (different markers). The diagonal dashed line indicates a linear fit through data points for normalized pressure drops in the range 0.5 - 0.8. The horizontal line corresponds to a normalized pressure drop of 1.0 and the vertical line corresponds to the value of U_{mf}.

Figure 20 shows the ratio of the U_{mf} (first row) and U_{mb} (second row) for vibrated vs. non-vibrated cases as well as U_{mf}/U_{mb} under vibrated conditions (third row) versus vibration strength for constant vibration frequency (first column) and constant vibration amplitude (second column) conditions. Results show that both U_{mf} and U_{mb} decrease with increasing vibration strength and in most cases this decrease plateaus at $\Gamma \sim 0.5$. At the same vibration strength, $U_{mf}/U_{mf,nv}$ and $U_{mb}/U_{mb,nv}$ do not vary much with changing particle density or vibration frequency or amplitude. In contrast, particle diameter has a significant and non-monotonic effect on the reduction in U_{mf} and U_{mb} caused by vibration. We are currently unable to explain this non-monotonic behavior.

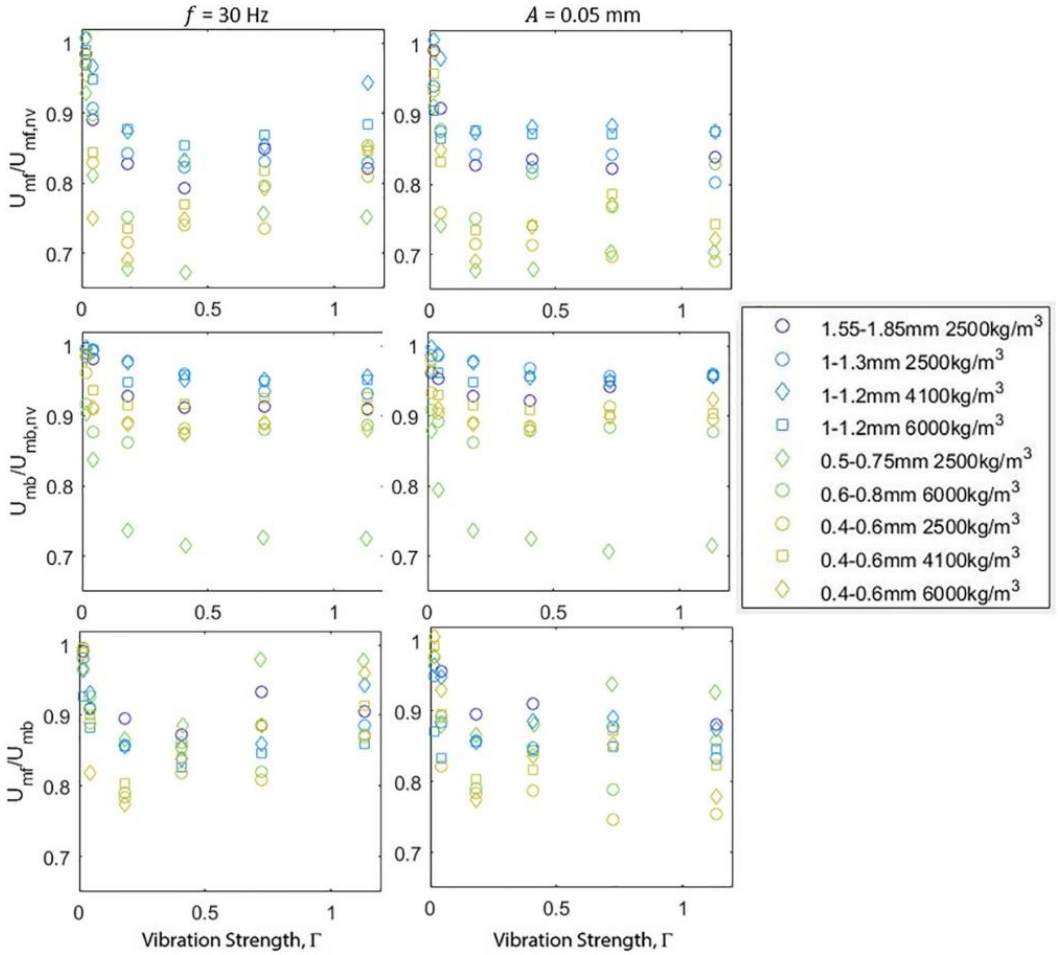

Figure 20 $U_{mf}/U_{mf,nv}$ (non-vibrated) (first row), $U_{mb}/U_{mb,nv}$ (second row) and U_{mf}/U_{mb} under vibrated conditions versus vibration strength for a vibration frequency of 30 Hz (first column) and a vibration amplitude of 0.05 mm (second column). Different color markers indicate different particle sizes and different marker shapes indicate different particle densities. Markers are based on the average of 3 separate measurements with error bars not shown for clarity, but generally smaller than the marker size. Experiments were conducted in a 74 mm diameter, cylindrical fluidized bed.

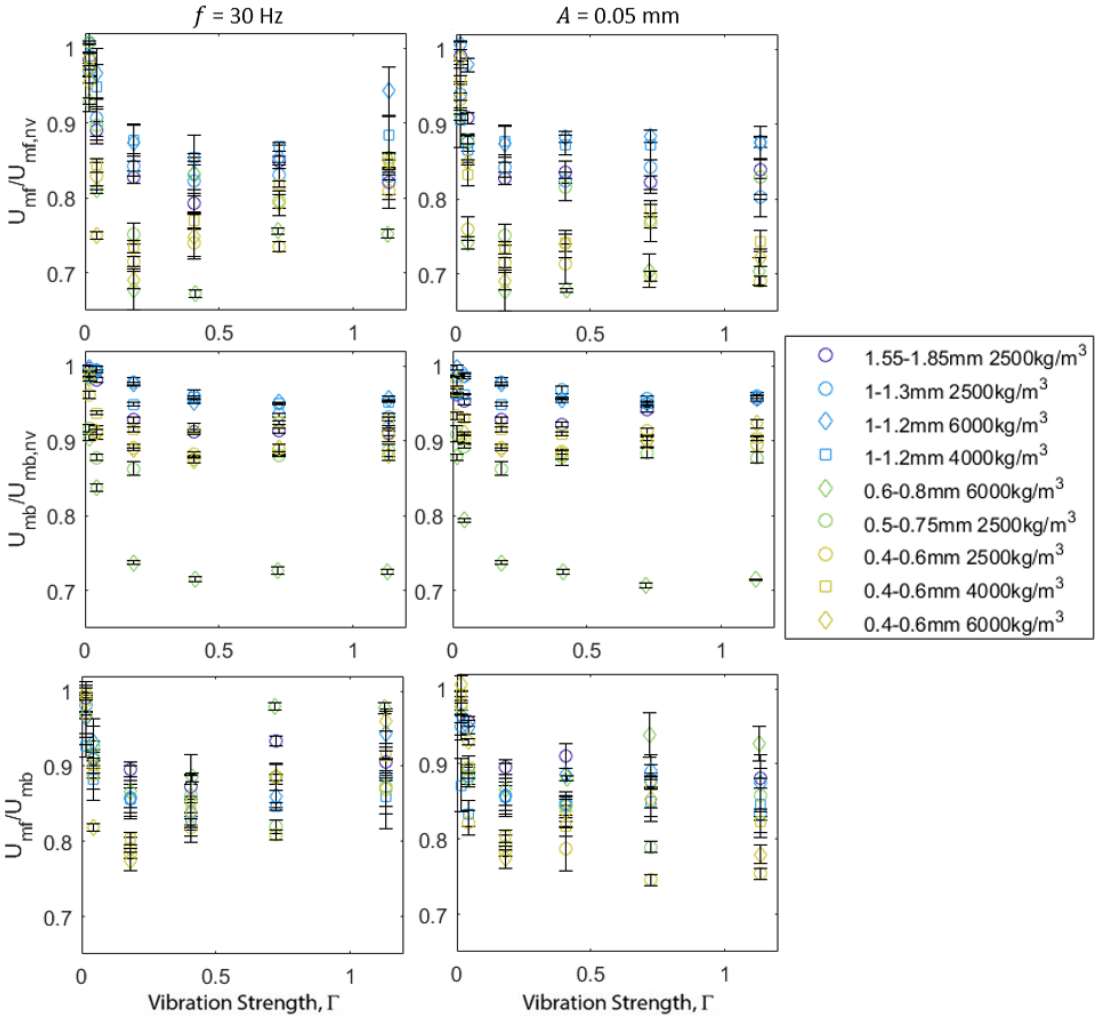

Figure 21 $U_{mf}/U_{mf,nv}$ (non-vibrated) (first row), $U_{mb}/U_{mb,nv}$ (second row) and U_{mf}/U_{mb} under vibrated conditions versus vibration strength for a vibration frequency of 30 Hz (first column) and a vibration amplitude of 0.05 mm (second column). Different color markers indicate different particle sizes and different marker shapes indicate different particle densities. Markers are based on the average of 3 separate measurements with error bars not shown for clarity, but generally smaller than the marker size. Experiments were conducted in a 74 mm diameter, cylindrical fluidized bed. Error bars show the standard deviation of 3 separate runs.

Wang et al. [60] and Barletta et al. [61] have shown that when the fluidized bed is vibrated at resonance frequency the minimum fluidization velocity is decreased. Here we have explored if the resonance frequency explains the non-monotonic decrease of U_{mf} for increasing vibration strength. The equation $f = (2n + 1)c/4H$ with n = 0,1,2… from Barletta et al. [61] was used to calculate the resonance frequencies. Here, H is the fill height, which was set at 10 cm and $c = \sqrt{E_g \varepsilon \rho}$. E_g is the elastic modulus of the air, ε is the void fraction, and ρ is the average density of the fluidized bed corresponding to the bulk density of each of the particle types used. Because the system compression for a fluidized bed is an isothermal process [62] the elastic modulus is equal to the gas pressure p ≈ 0.1 MPa [61]. The resonance frequencies determined are shown in **Figure 23** . Of the resonance frequencies calculated, three are within 3 Hz of the excitation frequencies: The first resonance frequency of glass particles at 32.3 Hz, the second resonance frequency of zirconium oxide particles at 61.6 Hz and the second resonance frequency of zirconium silicate particles at 76.5 Hz. In **Figure 20** it can be seen that different particle materials follow the same pattern for rising vibration strength with a local minimum of U_{mf} / $U_{mf,nv}$ at vibration strengths Γ = 0.181 or 0.408. For a fixed amplitude of 0.05 mm the vibration strengths Γ = 0.181 and 0.408 correspond to frequencies of 30hz and 45hz respectively. Thus the 1st resonance frequency of glass corresponds to the local minimum of U_{mf} / $U_{mf,nv}$ for Γ = 0.181. This however does not explain the local minima during rising vibration strengths for other the materials nor the local minima of some glass particles at

Γ = 0.408. When the frequency is held constant at 30 Hz, a minimum in $U_{mf}/U_{mf,nv}$ is also observed at either Γ = 0.181 or 0.408. Therefore, it seems that if the resonance frequency plays a role in the non-monotonic behavior of U_{mf} for increasing vibration strengths it is covered up by the larger effect of the vibration strength on U_{mf}.

In all cases, vibration causes a larger reduction in U_{mf} than U_{mb}, and thus U_{mf}/U_{mb} is less than unity, demonstrating that vibration with low values of Γ can create a densely packed, bubble-free fluidization state.

Figure 22 shows (a) U_{mf}, (b) U_{mb} and (c) U_{mf}/U_{mb} under vibrated conditions versus vibration strength for conditions in a pseudo-2D bed and a 3D cylindrical system. Results show that the shape of the U_{mf} vs vibration strength and U_{mb} vs vibration strength curves are fairly similar across different bed geometries and particle properties. Further, at the same vibration strength, U_{mf} and U_{mb} are fairly similar even if different values of f and A are used as shown by a comparison of the two columns of plots. However, U_{mf} and U_{mb} increase in moving from a 3D cylindrical to a pseudo-2D bed across all vibration conditions studied. The ratio of U_{mf}/U_{mb} generally decreases with increasing vibration strength, but it does not change in any noticeable systematic way in changing particle properties or changing from a 3D cylindrical to a pseudo-2D system.

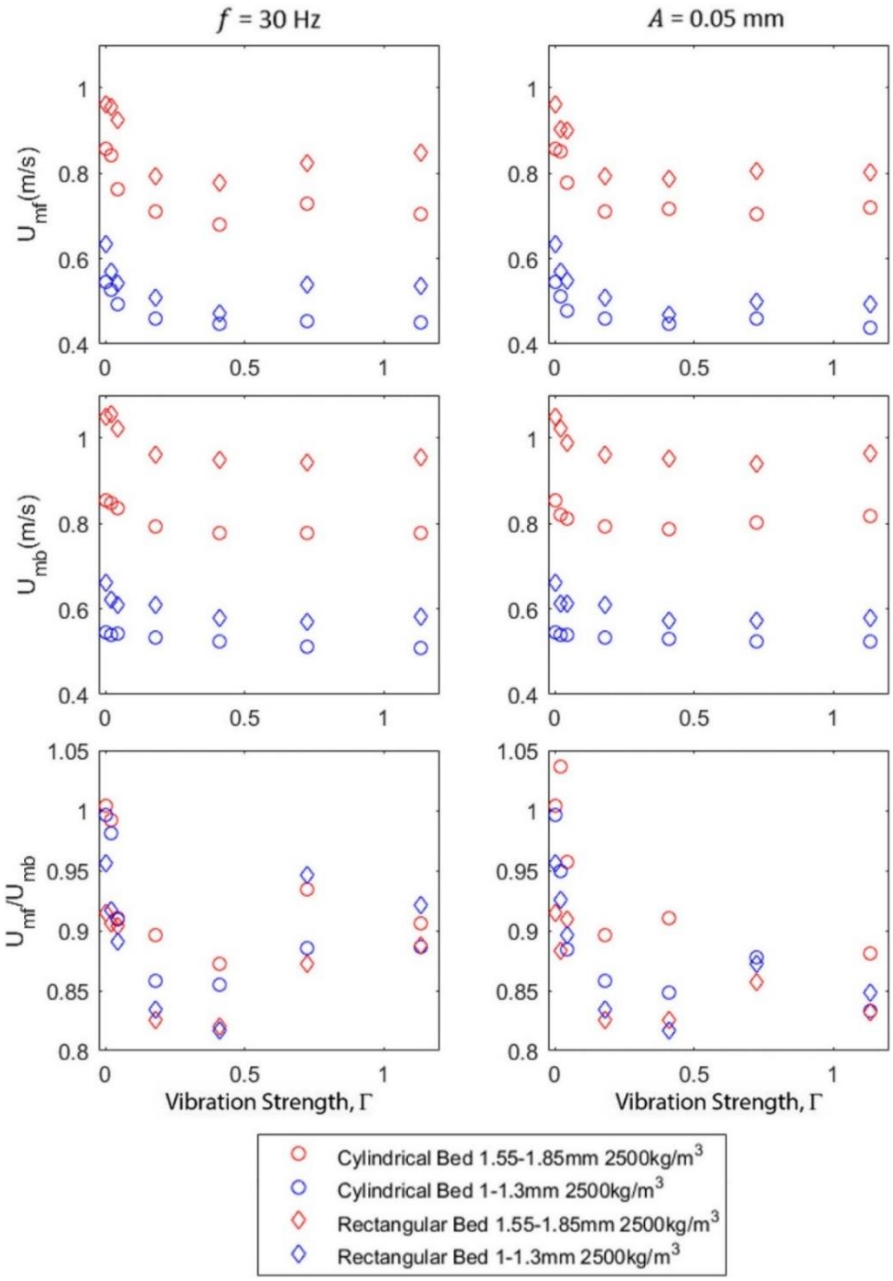

Figure 22 U_{mf} (first row), U_{mb} (second row) and U_{mf}/U_{mb} under vibrated conditions versus vibration strength for a vibration frequency of 30 Hz (first column) and a vibration amplitude of 0.05 mm (second column). Different color markers indicate different particle types and different marker shapes indicate different bed shapes. Markers show the average from three separate experiments and error bars are not shown for clarity, but were generally smaller than the marker size. Experiments were conducted in a pseudo-2D fluidized bed (rectangles) or a cylinder (circles).

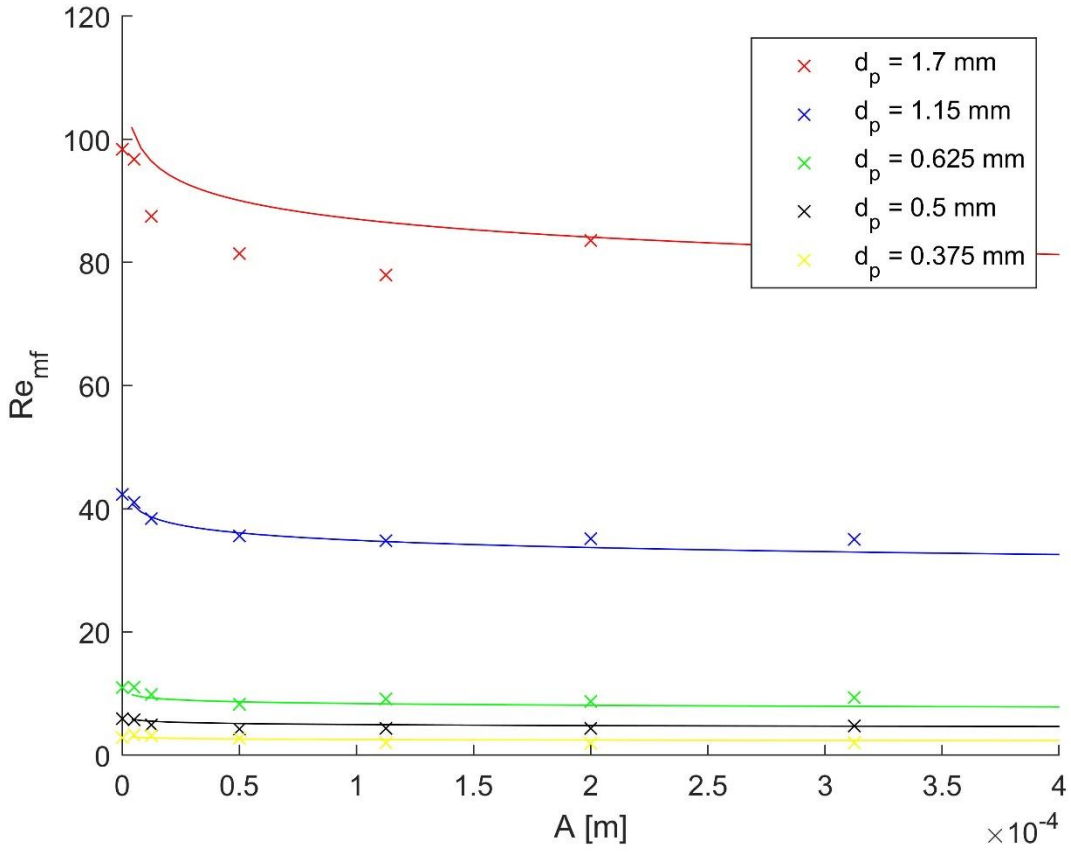

Figure 23 A comparison of experimental Re_{mf} values with the calculated values for glass particles varying the amplitude. The lines represent the calculated values and the markers the actual values.

Prior studies have noted that U_{mf} increases in non-vibrated 2D gas-solid fluidized beds due to wall effects. Rojo et al. [63] found that the ratio of particle-particle contacts to particles-wall contacts influenced the electric charge on the particles. The study found that the electric charge on particles is higher in a 2D bed than a 3D bed, and this higher electric charge causes U_{mf} to be higher in a 2D bed than a 3D bed. Ramos Caícedo et al. [64] attributed the higher value of U_{mf} in a 2D bed as compared to a 3D bed due to greater friction at the wall in a 2D bed and demonstrated the effect of particle-wall interactions on U_{mf} by showing that U_{mf} increases with bed height in 2D beds. On the other hand, U_{mf} is unchanged by bed height in 3D beds. Sánchez-Deglado et al. [65] found the U_{mf} of a 2D bed to be a function of the particle size and bed thickness; the greater the ratio of particle size to bed thickness the larger the value of $U_{mf,2D}$. In **Figure 24**, the ratio of $U_{mf,2D}/U_{mf,3D}$ for the 1-1.3mm and 1.55-1.85mm diameter glass beads without vibration is respectively 1.12 and 1.17. These values are similar to the results obtained by Ramos Caícedo et al. [64] for the same bed height of 10 cm. For vibration strengths considered in this work, the ratio of $U_{mf,2D}/U_{mf,3D}$ stays between for 1.05 and 1.21 without any noticeable trend.

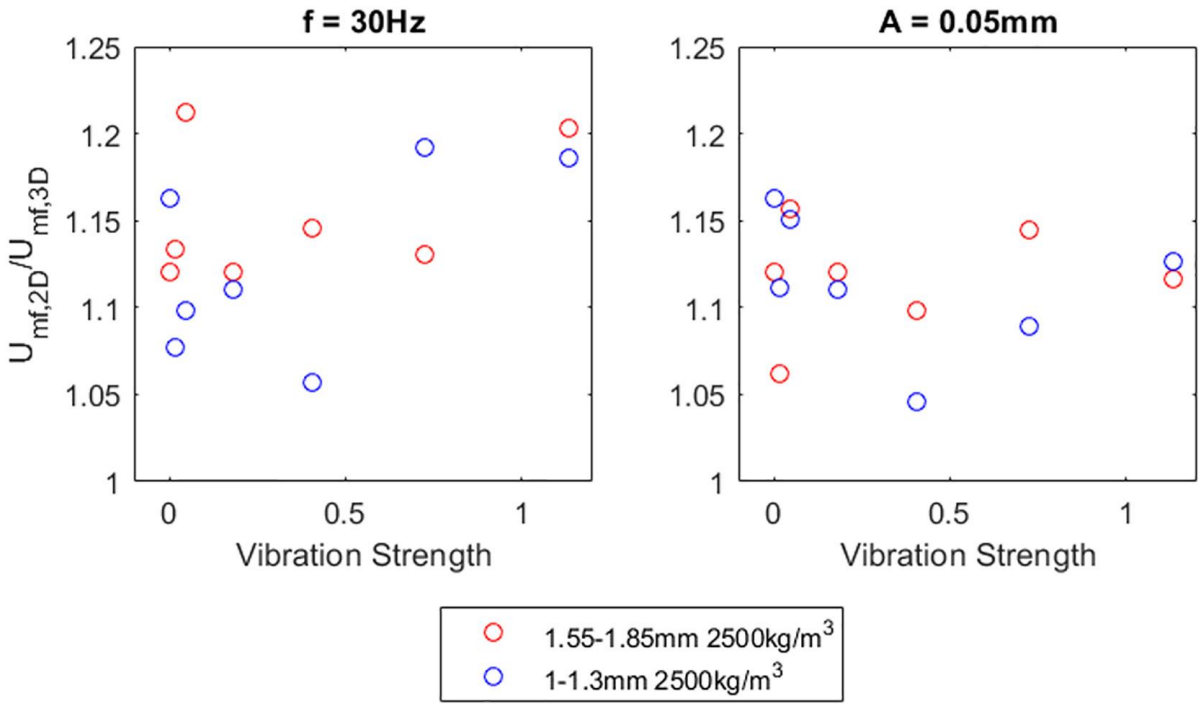

Figure 24 $U_{mf,2D}/U_{mf,3D}$ under vibrated conditions versus vibration strength for a vibration frequency of 30 Hz (first column) and a vibration amplitude of 0.05 mm (second column). Different color markers indicate different particle sizes. Markers show the average from three separate experiments and error bars are not shown for clarity but were generally smaller than the marker size. The experiments were conducted in a pseudo-2D fluidized bed and a cylindrical bed.

Table 4 Shaker input settings, the frequency and amplitude were set resulting in a given vibration strength.

Amplitude (mm)	Frequency (hz)	Vibration Strength
0,050	0	0,000
0,050	9,5	0,018
0,050	15	0,045
0,050	30	0,181
0,050	45	0,408
0,050	60	0,725
0,050	75	1,133
0,000	30	0,000
0,005	30	0,018
0,013	30	0,045
0,050	30	0,181
0,113	30	0,408
0,200	30	0,725
0,313	30	1,133

A dimensional analysis is performed to find a set of dimensionless parameters. These parameters form the basis of a simple power law function, estimating U_{mf} as a function of vibration. At fluidization, the pressure drop of the fluid flow across the packing balances gravitational and vibrational force. Analogous to the Ergun-equation [66] the pressure drop of the vibro-fluidized bed also depends on the packing and fluid properties. Hence, nine variables influence the system: particle diameter d_p, void fraction ε_{mf}, minimum fluidization velocity U_{mf}, gas density ρ_g, density difference between solid and gas phase $\Delta\rho$, gas viscosity μ_g, vibration amplitude A, vibration frequency ω, and gravitational acceleration g. Buckingham theorem dictates six independent dimensionless groups $\Pi_1 \dots \Pi_6$ to fully describe the physical system. Here, the following groups are chosen:

$$\Pi_1 = \frac{d_p u_{mf} \rho_g}{\mu_g} = Re_{mf},$$

$$\Pi_2 = \frac{d_p^3 \rho_g \Delta\rho g}{\mu_g^2} = Ar,$$

$$\Pi_3 = \varepsilon_{mf},$$

$$\Pi_4 = \frac{A\omega^2}{g} = \Gamma,$$

$$\Pi_5 = \frac{\omega \Delta\rho d_p^2}{\mu_g},$$

$$\Pi_6 = \frac{A}{d_p}.$$

$\Pi_1 \dots \Pi_3$ are the Reynolds number, Archimedes number, and void fraction; all being established groups in fluidization engineering. $\Pi_4 \dots \Pi_6$ represent acceleration, frequency and amplitude of the vibration scaled by gravity, particle relaxation time, and particle diameter, respectively. The formation of dimensionless groups allows finding a dimensionless function $Re_{mf} = f(\Pi_2, \dots, \Pi_6)$ to predict the minimum fluidization velocity. As starting point for the function f, a power law is assumed:

$$Re_{mf} = k\, \Pi_2^a\, \Pi_3^b\, \Pi_4^c\, \Pi_5^d\, \Pi_6^e. \tag{5.1}$$

This power law enables an easy access to the sensitivity of Re_{mf} to changes of any of the other groups. In order to find the unknown exponents $a \dots e$, the equation is transformed into a linear form by taking the logarithm. A Moore-Penrose pseudoinverse finds the least-square fit on the experimental data. The fit results in the following equation:

$$Re_{mf} = 0.075\, Ar^{0.910}\, \varepsilon_{mf}^{2.373}\, \Gamma^{0.074} \left(\frac{\omega \Delta \rho d_p^2}{\mu_g}\right)^{-0.257} \left(\frac{A}{d_p}\right)^{-0.123} \tag{5.2}$$

The quality of the parameter fit is evaluated in **Figure 25** comparing the experimental Re_{mf} values with the values calculated according to Eq. (5.2). The graph shows a good quantitative agreement between the experimental data and the model for Reynolds numbers ranging over two orders of magnitude. Until now most vibro-fluidization experiments have been performed with Geldart group A and C particles. Results using these type of particles from the works of Mawatari et al, Xu and Zhu, and Zhou et al. are also shown for comparison [78, 93, 94]. **Figure 23** and **Figure 26** further demonstrate, that the model equation is able to quantitatively capture the descending trend of U_{mf} with increasing A and ω for a series of particle diameters. Evaluation of the resulting equation indicates that Ar and ε_{mf} have a major influence on the fluidization velocity of vibro-fluidized beds due to their large exponents. The increase of U_{mf} with increasing Ar is well known in fluidization engineering and is due to an increasing gravitational effect, e.g. with increasing particle size or density. Comparing the determined exponent of Ar (0.91) with the exponent of Ar (0.5) for non-vibrating coarse particle beds as found by Chitester et al. [2], the fluidization velocity seems to be more sensitive to Ar in vibrated beds. The voidage, ε_{mf} is effected by vibration as seen in Geldart particles type A and C. [55] In our experiments with Geldart particle types B and D an almost constant value of 0.4 was found. Thus, despite its large exponent, the influence of ε_{mf} on Re_{mf} is less pronounced when the bed is subjected to vibration.

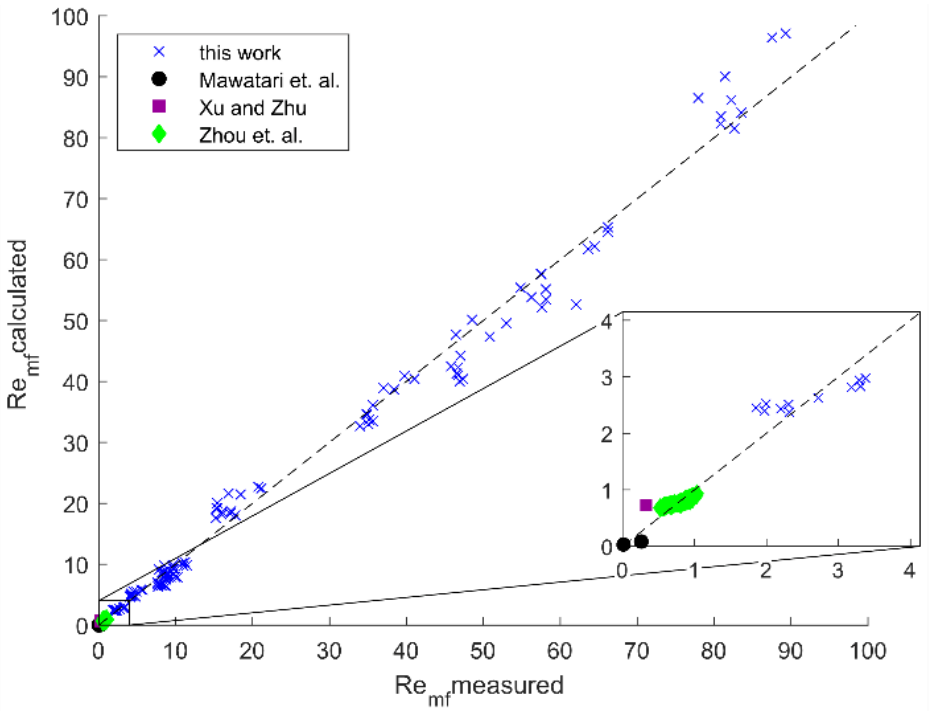

Figure 25 Comparison of experimental Re_{mf} values with Eq. 5.2. Different markers indicate different studies. Results from Mawatari et al., Xu and Zhu, and Zhou et al. are also shown for comparison. The sole point from Xu and J. Zhu is the only Geldart type B particle from their study [78, 93, 94].

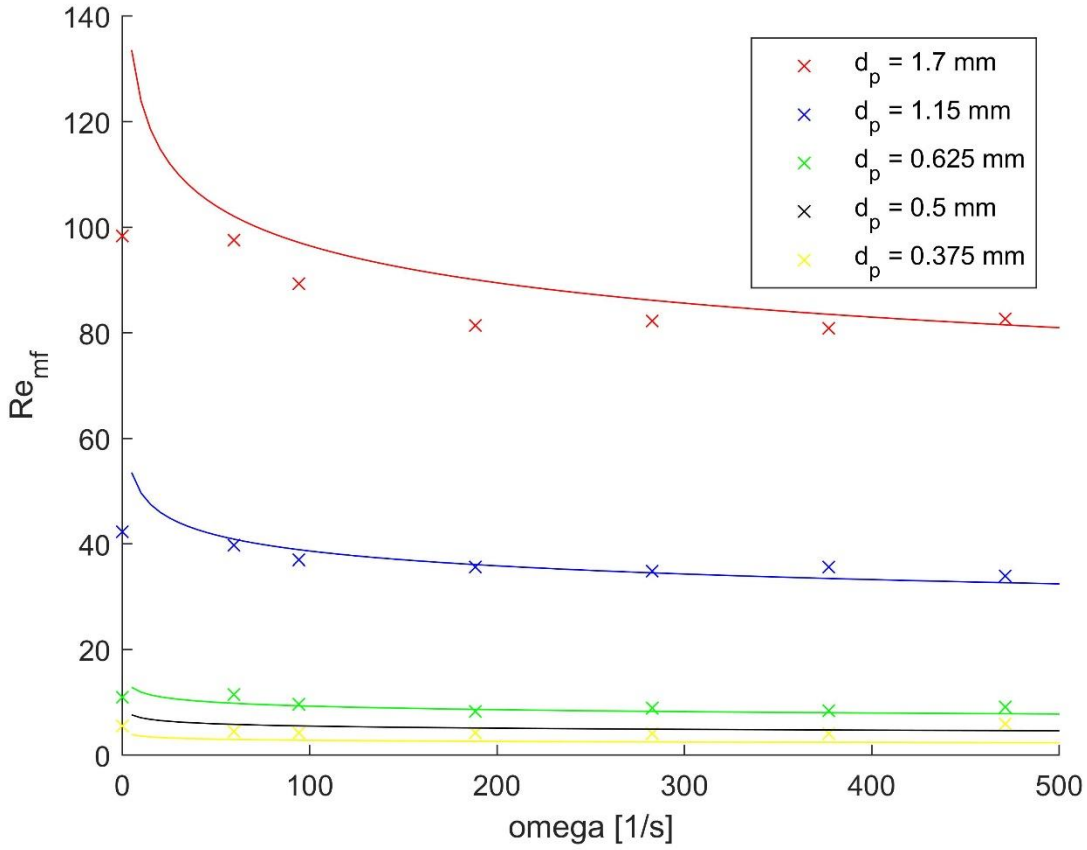

Figure 26 A comparison of experimental Re_{mf} values with the calculated values for glass particles varying the frequency. The lines represent the calculated values and the markers the actual values.

In order to isolate the effect of vibration amplitude and frequency, the model equation needs to be rearranged, since both variables are included in multiple dimensionless groups. A rearrangement leads to $Re_{mf} \propto A^{-0.049}\ \omega^{-0.109}$. This dependency shows that Re_{mf} decreases with both, increasing amplitude and frequency, which is in accordance with experimental observations.

The shortcoming of the power law ansatz lies in regions, where the dimensionless amplitude and frequency approach zero values. Due to the negative exponents the derived equation possesses pole points for A→0 and ω→0. Thus, it fails to reach the correct values of Re_{mf} at zero vibration. However, the non-vibration case is outside of the scope of the present model, as there already exist well-established correlations for Re_{mf} for no vibration systems. Except for this case, the power law can reproduce the experimental observations over a large range of particle sizes, densities, and vibration settings.

6.5 Conclusions

De-fluidization experiments of vibrated gas-solid fluidized beds show that vibration decreases U_{mf} and U_{mb} in Geldart Group B and D particles for vibration strengths less than 1. Vibration decreases U_{mf} more than U_{mb}, creating a densely packed, homogeneous fluidization state when $U_{mf} < U < U_{mb}$. Plotting vibration strength, Γ, vs. U_{mb} or U_{mf} allows the values across various vibration frequencies and amplitudes to fall onto the same curve. Particle density does not have a strong effect on the extent of reduction in U_{mf} or U_{mb} due to vibration; however, particle size has a significant and non-monotonic effect on the extent of this reduction. The reduction in U_{mf} and U_{mb} due to vibration is observed in both 3D cylindrical and pseudo-2D fluidized beds; however, pseudo-2D beds have higher values of U_{mf} and U_{mb} for both vibrated and non-vibrated cases. The ratio of $U_{mf,2D}/U_{mf,3D}$ does not change with the addition of vibration. A dimensional analysis has been performed taking vibration into account, and we are able to find a power law that describes accurately the effect of vibration on U_{mf}.

7 The sinking dynamics and splitting of a granular droplet

Adapted from: Metzger, J. P., McLaren, C. P., Pinzello, S., Conzelmann, N. A., Boyce, C. M., & Müller, C. R. (2022). Sinking dynamics and splitting of a granular droplet. Physical Review Fluids, 7(1), 014309.

7.1 Abstract

Recent experimental results have shown that binary granular materials fluidized by combined vibration and gas flow exhibit Rayleigh-Taylor-like instabilities that manifest themselves in rising plumes, rising bubbles and the sinking and splitting of granular droplets. This work explores the physics behind the splitting of a granular droplet that is composed of smaller and denser particles in a bed of larger and lighter particles. During its sinking motion, a granular droplet undergoes a series of binary splits resembling the fragmentation of a liquid droplet falling in a miscible fluid. However, different physical mechanisms cause a granular droplet to split. By applying particle-image-velocimetry and numerical simulations, we demonstrate that the droplet of high-density particles causes the formation of an immobilized zone underneath the droplet. This zone obstructs the downwards motion of the droplet and causes the droplet to spread and ultimately to split. The resulting fragments sink at inclined trajectories around the immobilized zone until another splitting event is initiated. The occurrence of consecutive splitting events is explained by the re-formation of an immobilized zone underneath the droplet fragments. Our investigations identified three requirements for a granular droplet to split: 1) frictional inter-particle contacts, 2) a higher density of the particles composing the granular droplet compared to the bulk particles and 3) a minimal granular droplet diameter.

7.2 Introduction

Granular motion leads to a series of natural phenomena such as sand dunes [32], rock slides [67] or avalanches [33]. In addition, a variety of industries, including the pharmaceutical and food industries [34] rely on granular materials and the handling thereof to manufacture their desired products. Granular materials are complex as they can exhibit solid-like, liquid-like or gas-like properties depending on the degree of external agitation [68]. One example is a fluid flowing upwards through a particle packing. At low fluid velocities, the packing is stationary and solid-like, yet if the fluid velocity is faster than the so-called minimum fluidization velocity (U_{mf}), the drag forces overcome gravity and the granular particles are in a fluidized state, i.e. the granular material exhibits liquid-like properties such as the rise of gas bubbles [97 – 100] in the bulk phase.

A prominent example of a classic fluid phenomena is the Rayleigh-Taylor (RT) instability in which dense and light fluids mix due to differences in buoyancy [17]. When two fluids of different density are layered, with the denser fluid on top of the lighter one, the RT instability creates interpenetrating “fingers” at the fluid interphase. Such fingering patterns, reminiscent of RT instabilities have been observed also in granular media [19, 36]. For example, RT-like patterns have been found to occur when a closed container is filled with either a liquid [20] or a gas [21] and the container is suddenly inverted, bringing previously sedimented particles to the top of the container. More recently, McLaren et al. [56] observed RT-like instabilities in a binary set of dry granular materials that are simultaneously mobilized by fluidizing air and vibration in a pseudo-two-dimensional setup. In this work, a layer of larger and lighter particles below a layer of smaller and denser particles forms interpenetrating fingers. Moreover, McLaren et al. [56] found that a granular “bubble” made of lighter particles will rise in a bed of smaller and denser particles which are vibrated and gas fluidized.

The RT-like instability discovered by McLaren et al. [56] gives rise to another phenomenon that is typically also observed in fluids, i.e. the fragmentation of a liquid droplet falling in another miscible liquid [28]. In miscible fluids, a dense liquid droplet falling in a miscible but less dense liquid forms a torus. This torus increases in diameter until the RT instability creates discrete circumferential aggregations that become large enough to separate and form new toroidal structures [46 – 50]. Such fragmentation instabilities have also been observed in two-phase granular materials. When droplets of a suspension of glycerol-water and glass spheres sink in a glycerol-water solution at very low Reynolds numbers, the droplet transforms into a ring with

increasing radius [69]. In some cases, these droplets even exhibit a ring instability as seen in pure liquids [31]. McLaren et al. [56] demonstrated the presence of a fragmentation instability in dry granular materials when a so called “granular droplet” falls in another granular material. A granular droplet is an aggregation of smaller particles with diameter d_d and higher density ρ_d surrounded by a bulk of particles with a larger diameter d_b but lower density ρ_b. When the granular system is agitated by a fluidizing gas flow and vertical vibration, the granular droplet sinks through the bulk phase. Instead of sinking downwards in a straight motion, the granular droplet splits into two daughter droplets, which descend along inclined paths whereby the daughter droplets formed repeat the process. The structures observed show a striking similarity to a vertical cross section through a ring fragmentation formed by liquid droplets. However, unlike liquids, granular particles interact via frictional contact forces which can readily solidify the granular material and counteract a fluid-like motion, unless the particles are sufficiently agitated [68]. Therefore, the underlying mechanism driving granular droplet splitting must be different from the RT instability found in their liquid counterpart.

McLaren et al. [56] argued that a heterogeneous gas flow pattern forms around a granular droplet due to size differences between the granular droplet particles and bulk particles. They hypothesized this heterogeneity to cause locally solidified regions that initiate a droplet to split. However, gas heterogeneities alone cannot fully explain the dynamics of the splitting phenomenon, e.g. why the fragments formed during the first split descend further without splitting and then suddenly perform another split. Furthermore, it is unclear, if any fragmentation occurs when the gas flows homogeneously through the droplet and the surrounding bulk phase. Therefore, this study aims to elucidate the detailed mechanisms driving the motion and splitting of a granular droplet. In addition, we will determine the droplet properties that are necessary for a granular droplet to split. To this end, we combined experimental investigations applying a high-speed camera and particle image velocimetry (PIV) and numerical simulations to probe the effect of contact forces and gas flow dynamics.

7.3 Methods

7.3.1 Experimental setup, digital image analysis and particle image velocimetry

A pseudo-two-dimensional fluidized bed with a width of 400 mm, a height of 500 mm and a transverse thickness of 10 mm was used. The walls were made of polymethyl methacrylate (PMMA) sheets. Air for fluidization entered the bed through 40 evenly spaced holes of diameter 1.1 mm drilled into a PMMA distributor plate. The granular material consisted of two sets of spherical particles (Sigmund Lindner GmbH, SiLibeads): (i) Black colored glass particles with density ρ_b = 2500 kg/m³ and mean diameter d_b = 1.7 mm (referred to as bulk particles, index b) and (ii) white zirconium oxide particles with density ρ_d = 6000 kg/m³ and mean diameter d_d = 1.1 mm (referred to as droplet particles, index d), see **Table 5**. The bulk and droplet particles were chosen to have close minimum fluidization velocities in the non-vibrated state (U_{mf}). U_{mf} of the bulk particles is 0.9 m/s. The initial particle packing was prepared by first filling the bed with the less dense bulk particles to a height of 410 mm. The granular droplet was constructed on top of the bulk particles with its bottom edge located at a height of 410 mm. For this, two thin retaining walls were inserted into the freeboard of the bed dividing it into three vertical compartments. The central compartment had a width of D and was filled with droplet particles to a height D to construct a square-cuboid granular droplet of edge length D. Bulk particles were added on top of the granular droplet and in the outer two compartments to yield a final packing height of 460 mm. Once all three compartments were filled, the retaining walls were removed. By varying the distance between the two retaining walls as well as the height D to which the droplet particles were poured in, granular droplets of variable edge length (D = 10, 20, 30, 40, 50 mm) were constructed. The first panel in **Figure 28** shows the initial state of a bed containing a granular droplet with D = 50 mm. The experiment was started by simultaneously vibrating and fluidizing the bed. To impose a defined vibration on the system a Labworks shaker (Labworks Inc., ET-139) was used generating a vertical sinusoidal displacement $\delta = A\sin(2\pi f t)$. Besides the shaker, the vibration system contains a controller (Labworks Inc. VL-144), an amplifier (Labworks Inc., PA-138-1), and an accelerometer (PCB Piezotronics Inc., J352C33.). In the experiments, the amplitude A and frequency f were varied in the range of A = [0.05 mm, 1 mm] and f = [10 Hz, 47.4 Hz]. The frequency and amplitudes used, resulted in a span of dimensionless vibration strengths $\Gamma = A(2\pi f)^2/g$ = [0.18, 0.45], where Γ is the peak acceleration of the vibration

normalized by the magnitude of the gravitational acceleration g. The fluidization airflow was controlled using a mass flow controller (Bronkhorst AG, F-203AV). After the mass flow controller, the air passed through a humidifier to ensure a constant relative humidity of 87-91 % in order to keep electrostatic forces from building up on the surfaces of the particles and bed walls. A sensor (Sensirion AG, SHT31) measured the humidity at the exit of the humidifier. Despite the addition of humidity, the calculated density change of air is less than 1 % and signatures of liquid bridging between the particles were not observed. The superficial gas velocity U was close to the minimum fluidization velocity U_{mf} of the bulk particles in the non-vibrated state. U_{mf} was determined via pressure drop measurements between the top of the distributor plate and the freeboard of the bed. The values of U ranged from U/U_{mf} = [0.95, 1.04]. The combined use of vibration and fluidizing air created a fluidization state of the granular matter, in which the particles were sufficiently mobilized while avoiding the emergence of gas bubbles that would usually appear if the granular particles were fluidized by gas alone [56] [70]. By combining vibration and fluidization by gas allows for a granular droplet to evolve without being disturbed by gas bubbles that can e.g. induce convective flow patterns. This particular fluidized state of the granular matter caused by combined gas flow and vibration will be further referred to as "vibro-gas-fluidized bed".

A CCD camera (Photron GmbH, Fastcam SA Z.) with a framerate of 50 Hz was used to record the experiment. After recording, a digital image analysis was performed in order to track the position of the granular droplet and its daughter droplets. For this purpose, a MATLAB script tracked the leading edges of the granular daughter droplets and calculated their sinking speed. The tracking routine is shown in **Figure 27**. Additionally, the script calculated the splitting angle of the granular daughter droplets, i.e. the angle enclosed by the two lines connecting the leading edges of the granular daughter droplets and the center of the initial position of the granular droplet (see inset of **Figure 40** (a)). The splitting angle was determined as a function of the distance travelled y_h, whereby y_h is calculated as the mean vertical distance travelled by the left (y_{hl}) and right (y_{hr}) granular daughter droplet, see inset of **Figure 40** (a). For all of the recorded repetitions of an experiment, the function $\alpha(y_h) = k_1 e^{-k_2 y_h} + \alpha_{asym}$ was fitted to determine the asymptotic splitting angle α_{asym}. A series of experiments were performed varying either the droplet size D, the airflow U/U_{mf} or the vibration strength Γ. For each setting of the parameters D, U/U_{mf} and Γ, three experiments were performed and averaged to calculate the sinking trajectory of the granular droplet and its fragmentation into daughter droplets. These experiments were complemented by particle image velocimetry (PIV) measurements allowing us to calculate velocity maps of the bulk particles. As tracer particles for PIV, 10 % of the bulk particles were white glass particles with otherwise identical properties as the black bulk particles. The MATPIV 1.6.1. software [71] was used to calculate the velocity maps from consecutive image frames. The size of the PIV interrogation window was iteratively reduced from 64×64 to 32×32 pixels, using four iterations. The PIV data were then averaged over three frames i.e. a period of 0.3 s to reduce noise.

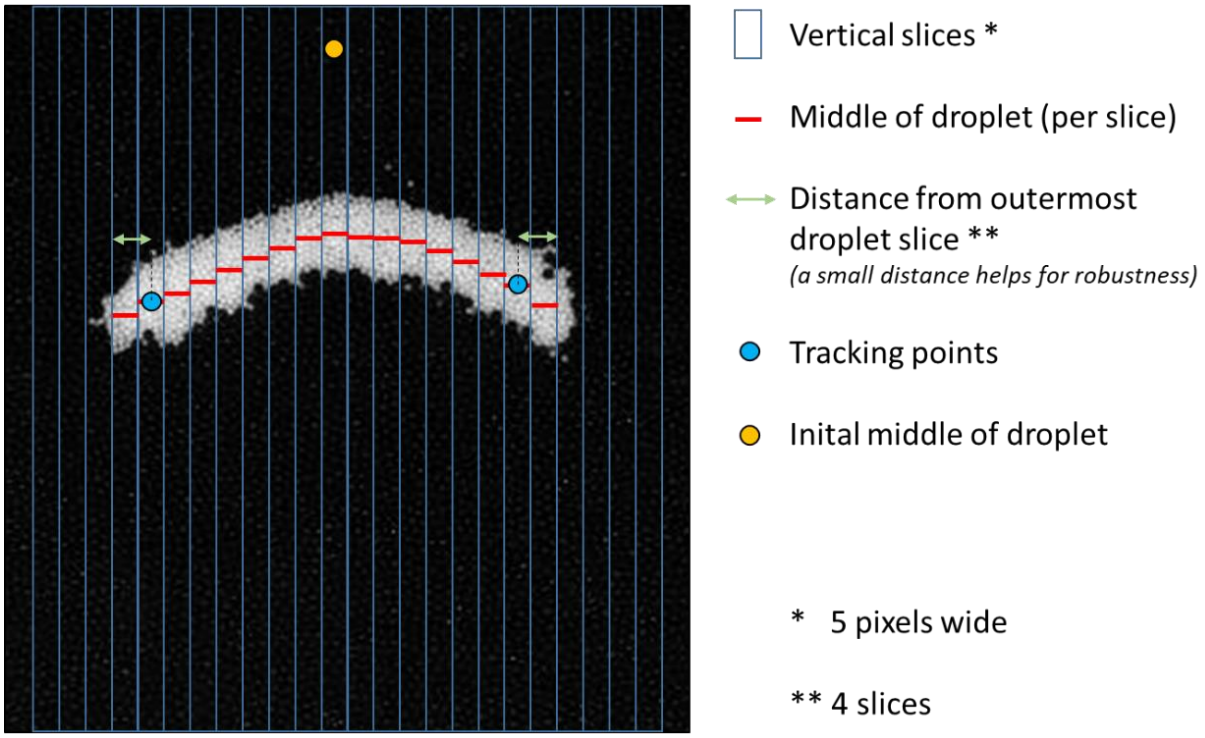

Figure 27 Digital image analysis on a sinking granular droplet (white particles) about to form the two daughter droplets. The bed is divided into equally spaced vertical slices (each 5 pixels wide) to identify the leading edges of the daughter droplets formed from the initial granular droplet. For sake of tracking robustness, the tracking points (representing the leading edges) were set with a distance from the outermost slices that contain droplet particles.

7.3.2 Euler-Lagrange simulations of the granular droplet

i. Modeling strategy: CFD-DEM

To numerically model the dynamics of granular droplets, a combined computational fluid dynamics and discrete element method (CFD-DEM) was used (open-source framework *CFDEM®Coupling*) [72]. CFD-DEM treats the particles as discrete entities (Lagrangian approach) that are immersed in a finite volume description of the fluid phase providing detailed information on the trajectories of each particle as well as inter-particle forces [104 – 108].

The DEM approach has been introduced by Cundall & Strack [73] and applies Newton's second law of motion to calculate the trajectory of each particle through force and torque balances. For any given particle *i* of mass m_i the force balance reads

$$m_i \frac{\partial^2 \boldsymbol{x}_i}{\partial t^2} = \boldsymbol{F}_{c,i} + \boldsymbol{F}_{fp,i} + \boldsymbol{g} m_i, \tag{6.1}$$

where $\boldsymbol{F}_{c,i}$ and $\boldsymbol{F}_{fp,i}$ represent, respectively, the sum of all contact forces and the sum of all fluid-particle interaction forces acting on the particle and $\boldsymbol{g}$ is the gravitational vector. In the present work, particles were modelled as perfect spheres with elastic and isotropic material properties. The coefficient of restitution *e* and the coefficient of friction μ for both materials are given in **Table 5**. Particle contacts were described using the soft-sphere approach, whereby the normal contact forces follow the Hertz-Mindlin law expressed by a non-linear spring-dashpot model [105, 110]. The tangential contact forces were also modelled by a non-linear spring-dashpot model, but were limited by the Coulomb criterion [74]. The gas flowing through the particle bed gave rise to various fluid-particle interaction forces $\boldsymbol{F}_{fp,i}$. This work considered three fluid interaction forces: viscous force, pressure force, and drag force. Viscous and pressure forces stem from global variations in the fluid stress

tensor on a length scale that is significantly larger than the particle size, whereas the drag force is due to flow variations in the vicinity of the particles [43]. It has been shown that the drag force dominates particle fluidization. The drag force was calculated by the Koch-Hill closure model [111, 112]. Other fluid-particle interaction forces such as virtual mass force or Basset force are negligible as the density of the gas is small compared to the particle density.

Table 5 Particle properties.

		Simulation		Experiment	
Property	Symbol (unit)	bulk	droplet	bulk	droplet
Particle diameter	d (mm)	1.7	1.1	1.7 ± 0.06	1.1 ± 0.06
Density	ρ (kg/m³)	2500	6000	2500	6000
Young's modulus	E (MPa)	5	5	63	210
Poisson ratio	ν	0.2	0.3	0.2	0.3
Coefficient of restitution	e	0.88	0.7	0.88 ± 0.09	0.7 ± 0.1
Coefficient of friction	μ	0.47	0.38	0.47 ± 0.01	0.38 ± 0.05
Minimum fluidization velocity[1]	U_{mf} (m/s)	1.11	1.22	0.92 ± 0.01	0.90 ± 0.04

Two-way coupling between the dispersed particles and the continuous gas phase was established through an "unresolved" CFD-DEM approach. Here, a finite volume method solves volume-averaged Navier-Stokes-equations for the gas phase on a numerical grid (CFD grid) with cell size larger than the particle diameter, so that a no-slip boundary condition cannot be resolved on the particles, and thus a drag law must be used. This method accounts for the presence of the immersed particles by calculating the void fraction ϵ_{f} and a momentum exchange term $\boldsymbol{R}_{\mathrm{pf}}$ in each CFD cell. ϵ_{f} is the volume fraction of a CFD cell that is occupied by the gas phase and is determined by the particle positions from the DEM. $\boldsymbol{R}_{\mathrm{pf}}$ is the sum of the drag forces $\boldsymbol{F}_{\mathrm{d,i}}$ acting on all particles that are located in a given CFD cell of volume ΔV [64, 103, 113]. Owing to its constant temperature and the low Mach number involved, an incompressible solver with constant gas density ρ_{f} was used to model the gas flow, simplifying the volume-averaged Navier-Stokes-equations to [71]

$$\frac{\partial \epsilon_f}{\partial t} + \nabla \cdot \left(\epsilon_f \boldsymbol{u}_f\right) = 0, \tag{6.2}$$

$$\frac{\partial \left(\rho_f \epsilon_f \boldsymbol{u}_f\right)}{\partial t} + \nabla \cdot \left(\rho_f \epsilon_f \boldsymbol{u}_f \boldsymbol{u}_f\right) = -\epsilon_f \nabla p - \boldsymbol{R}_{pf} + \epsilon_f \nabla \cdot \boldsymbol{\tau}_f + \rho_f \epsilon_f \boldsymbol{g}, \tag{6.2}$$

$$\boldsymbol{R}_{pf} = \frac{1}{\Delta V} \sum_{i=1}^{n} \boldsymbol{F}_{d,i}. \tag{6.3}$$

The shear stress tensor $\boldsymbol{\tau}_f$ in Eq. (6.2) was calculated as for an incompressible Newtonian fluid [26]. To resolve the particle collisions and to ensure numerical stability, the DEM part used a Verlet-integration scheme with a time step of 10^{-5} s. As such a high temporal resolution was not required for the CFD part, the time step of the

[1] In the text, U_{mf} refers to the value of the minimum fluidization velocity of the bulk particles. The respective value of the droplet particles is given for sake of completeness.

CFD solver was 10^{-4} s. Hence, every 10^{th} DEM time step a phase coupling was performed. More details concerning the two-way coupling can be found in the literature [72] .

ii. Model setup

Setting up a simulation involved two steps: (i) the initialization of the DEM packing and (ii) the initialization of the CFD domain. For the DEM part, a box of width 400 mm, transverse thickness 10 mm and height 600 mm was created representing the sidewalls of the fluidized bed. Bulk particles were inserted from the top of this box to build up a random packing of 480 mm height. A square cuboid volume (width 50 mm, height 50 mm, transverse thickness 10 mm) was removed from the bulk particle packing and filled with granular droplet particles to initialize, as in the experiments, a square shaped granular droplet of D = 50 mm. Subsequently, additional bulk particles were added to create a flat bed surface at a height of 480 mm. **Table 5** lists the properties of the particles used in the simulation. After initialization of the packing, the box was subjected to a vertical sinusoidal motion with A = 1 mm and f = 10 Hz. All frictional and collisional contacts between the particles and the walls of the box are fully resolved in the DEM. The collision properties of these walls are identical to those of the bulk particles. To model the gas phase, a CFD grid of cubic voxels with 5 mm edge length was generated covering the same space as the DEM box. At the bottom of the CFD grid, gas was injected with a constant speed. The gas had a constant density and viscosity of 1.2 kg/m³ and 18 µPas, respectively, resembling properties of air. **Table 6** summarizes all boundary conditions used for the CFD grid. Due to the coarse resolution of the CFD grid (2.94×d_b), a no-slip boundary condition would exaggerate the influence of the walls on the gas flow field; instead, a full-slip boundary condition was used [114, 115].

Table 6 Boundary conditions used in the CFD part.

Quantity	Symbol (unit)	inlet	outlet	wall
Reduced pressure	p/ρ_f (m²/s²)	zero gradient	10^5	zero gradient
Gas velocity	$\boldsymbol{u}_f$ (m/s)	$(0, U, 0)^T$	zero gradient	full slip

7.4 Results and Discussion

7.4.1 Fragmentation of a granular droplet

Both experiments and numerical simulations were applied to elucidate the underlying physics behind the phenomenon of granular droplet fragmentation. **Figure 28** (a) shows a comparison between experimental measurements and numerical simulations of the fragmentation dynamics of a granular droplet with D = 50 mm. Upon the start of vibration and fluidization, the square-shaped granular droplet flattens into a cap-shaped droplet (1.7 s). With time the cap-shaped droplet thins further, with the left and right ”edges” penetrating the bulk phase, starting to form two daughter droplets that are, however, still connected by a thick band of particles (3.7 s). The daughter droplets descend along inclined trajectories with a similar inclination angle. During the descent, the connecting band between the two daughter droplets thins out and they eventually fully detach from each other (7.5 s). The entire process that leads to the formation of two separated daughter droplets is referred to as a binary split. After the detachment, each daughter droplet flattens and thins out, forming again two leading edges at each droplet (11.2 s) with each undergoing eventually another binary split and forming again two fragments for each daughter droplet. The series of binary splits continuous until the formed fragments are too small to split further or the bottom of the bed is reached. As can be seen from **Figure 28** (a), the numerical simulations agree well with the experimental data with regards to droplet shape and timescale of the splitting.

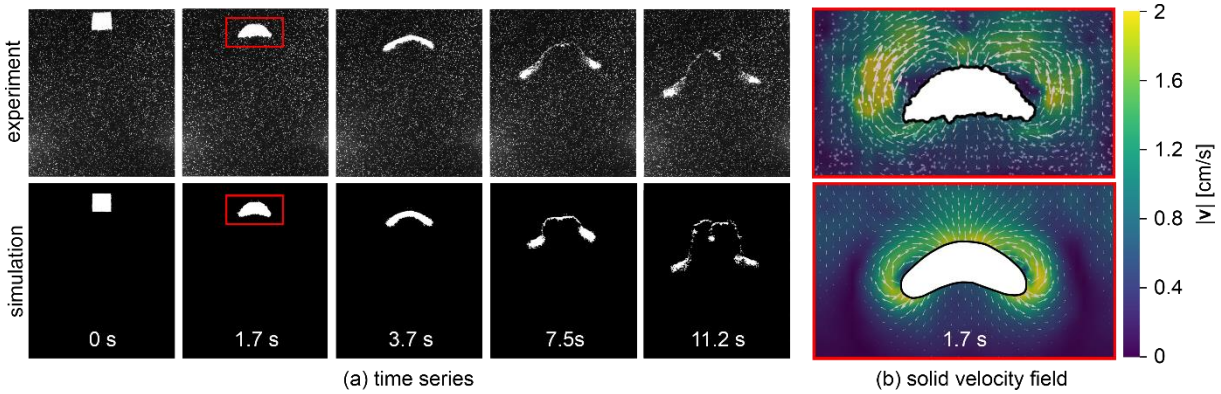

Figure 28 Comparison between experimental measurements (top row) and simulation results (bottom row) on the dynamics of the splitting of a granular droplet (D = 50 mm) in a vibro-gas-fluidized bed using f = 10 Hz, A = 1 mm, and U/U_{mf} = 0.95 (exp.) or U/U_{mf} = 0.97 (sim.). (a) Time series showing the evolution of a granular droplet during fragmentation. Bulk particles are black, droplet particle are white (particle properties according to **Table 5**). In the experiments, white tracer particles were added to the bulk phase for PIV measurements. (b) Velocity field of the bulk particles around the granular droplet as extracted from the red-framed region in (a) at 1.7 s. The granular droplet is white. The bulk particle phase is color-coded according to the velocity magnitude of the bulk particles. The velocity data was averaged over a period of 0.3 s to reduce noise in the PIV data.

In order to elucidate the underlying physics that drive the deformation and ultimately the splitting of the square-shaped granular droplet, the velocity field of the bulk particle phase is probed. **Figure 28** (b) shows the velocity field of the bulk particles in the vicinity of the granular droplet shown in **Figure 28** (a) at 1.7 s, as obtained by PIV measurements (top) and CFD-DEM simulations (bottom). In both cases, the velocity field of the bulk particles exhibits one vortex on each side of the granular droplet. At the center of the vortex, there is no granular movement. Overall, the bulk particles move from the leading edges to the roof of the granular droplet with the highest velocities (20 mm/s) being reached on a circular path with a radius of 20 mm from the vortex center. This motion pattern indicates that the displacement of bulk particles that drive the sinking motion of the droplet occurs primarily at the leading edges of the droplet. Due to conservation of mass, the displaced bulk particles move along circular paths towards the top of the droplet filling the space that has been occupied previously by the sinking droplet particles. In contrast to the rapid particle motion along the circular paths at the sides of the droplets, the bulk particle phase directly underneath the granular droplet appears to be largely immobile. This immobility is in contrast to what would be expected from an analogy of droplets falling in a liquid, where the displacement of the surrounding liquid is strongest underneath the sinking droplet. The immobility of this zone points to a frictional mechanism that locally reduces the fluidity of the bulk particle phase (immobilization) and obstructs the direct downward motion of the granular droplet. In the following, this region of particles of reduced particle motion due to frictional contacts and local solidification will be referred to as the "immobilized zone". The existence of an immobilized zone also seems to be the main driver behind the splitting of the granular droplet. However, to support this hypothesis further insight into inter-particle contacts is required, which however is not accessible by PIV measurements and necessitates CFD-DEM data. Due to the good qualitative and quantitative agreement of the numerical and experimental results, see **Figure 28** (a) and **Figure 28** (b) respectively, CFD-DEM data was used to investigate the immobilized zone and the requirements for granular droplet fragmentation to occur.

7.4.2 Formation of an immobilized zone and the cause of fragmentation

To understand better the formation of an immobilized zone and its effect on the granular droplet fragmentation, a CFD-DEM simulation was performed that tracked the particle motion with a temporal resolution of 2.5 ms. The high temporal resolution allows identifying different stages of particle motion within a single vibration cycle. In addition to the particle trajectories, the simulation provides information on the magnitude of the inter-particle forces for each particle contact. Here, the normal contact force $\mathbf{F}_{c,n}$ was used to localize force networks that constrain the motion of particles.

Figure 29 shows snapshots of a granular droplet and the surrounding bulk particle phase for five consecutive stages of a vibration cycle. The first column visualizes the normal contact forces acting on each bulk particle by connecting contacting particle centers with a black line. The darker the line, the higher the magnitude of the normal contact force. The second column shows the particle velocity *v* calculated in the reference frame of the vibrating bed, i.e. the *y*-component of *v* is reduced by the instantaneous vertical velocity of the confining walls. The third column of **Figure 29** sketches the overall motion of the granular droplet (gray) and the bulk phase (green). Each row of **Figure 29** (a-e) corresponds to one particular stage (vibration phase φ) in a vibration cycle.

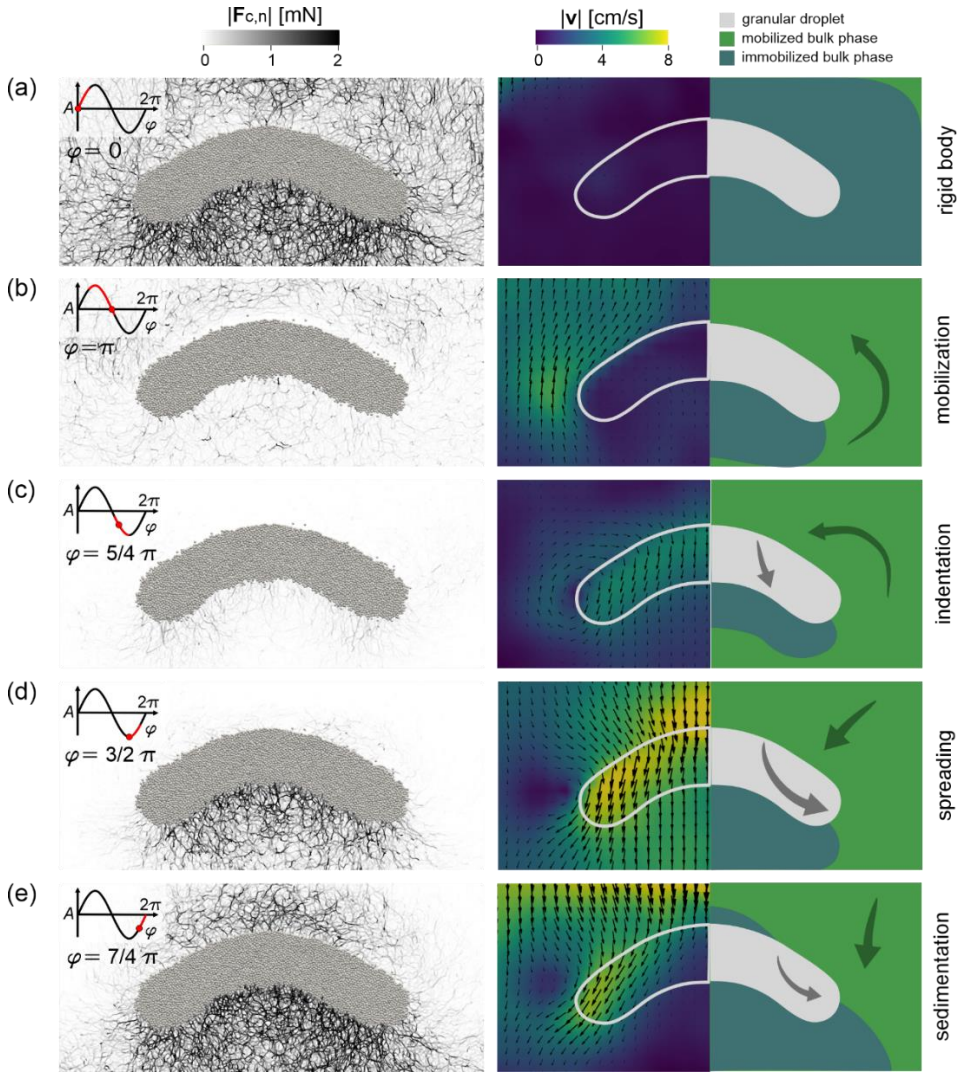

Figure 29 The dynamics of the bulk and granular droplet particles at different stages of the vibration cycle (phase φ). Each row illustrates one of the five stages of motion identified with increasing φ from (a) to (e). The sketch in the left top corner of each row indicates the vertical displacement of the bed at the given phase (red dot) and the extent of the corresponding stage of motion (red part of the sine curve). In the first column, the droplet particles are gray and the normal contact force $\mathbf{F}_{c,n}$ acting between contacting bulk particles is shown as black lines. The opacity of the black lines increases with increasing contact force magnitude. In the second column, the granular droplet is shown as a gray contour and the particle velocity $\boldsymbol{v}$ is visualized via color-coding and vector fields. Here, $\boldsymbol{v}$ is calculated in the reference frame of the vibrating bed, i.e. the *y*-component of $\boldsymbol{v}$ is reduced by the instantaneous vertical velocity of the confining walls. All results are obtained in a CFD-DEM simulation using A = 1 mm, f = 10 Hz, and U/U_{mf} = 0.97. The third column sketches the overall motion of the granular droplet (gray) and the bulk particle phase (green); light green indicates a mobilized and dark green an immobilized bulk phase.

Row (a) shows the vibration cycle at φ = 0, i.e. when the bed moves upwards, as indicated in the displacement sketch in the top left corner. Here, a network of strong inter-particle forces pervades almost the entire bulk phase, as can be seen in the contact force panel. This network inhibits any individual motion of the particles, hence the particles move in accordance with the imposed vibration of the bed with $\boldsymbol{v} = \mathbf{0}$, i.e. the particle velocity relative to the wall velocity is zero as shown in the second column of row (a). This rigid body movement lasts from φ = 0 to π/4 up to the point when the mobilization of the bulk particles is initiated.

In the mobilization stage (φ = π/4 to π), the bed has passed the cusp of the sinusoidal vibration and moves downwards again. This downwards movement combined with the effect of the fluidizing gas causes a loosening of the bulk phase and the bulk particles above and at the sides of the granular droplet move upwards relative to the walls as illustrated in the particle velocity panel of row (b). Simultaneously, the loosening is accompanied by a reduction of the contact force network in the entire bed. In contrast to the mobilized bulk phase above and besides the granular droplet, the particle velocity $\boldsymbol{v}$ within the granular droplet is almost zero, i.e. the granular droplet particles remain stationary relative to the walls. This is due to a smaller degree of fluidization of the droplet particles compared to the bulk particles (vide infra II.4), i.e. the droplet particles are not fully fluidized by the gas flow and the dominating gravity leads to the droplet following the movement of the walls (see also **Figure 30**). Moreover, the stationary droplet particles inhibit the motion of the bulk particles directly below the granular droplet, which can be inferred from $\boldsymbol{v}$ being comparably small in this region.

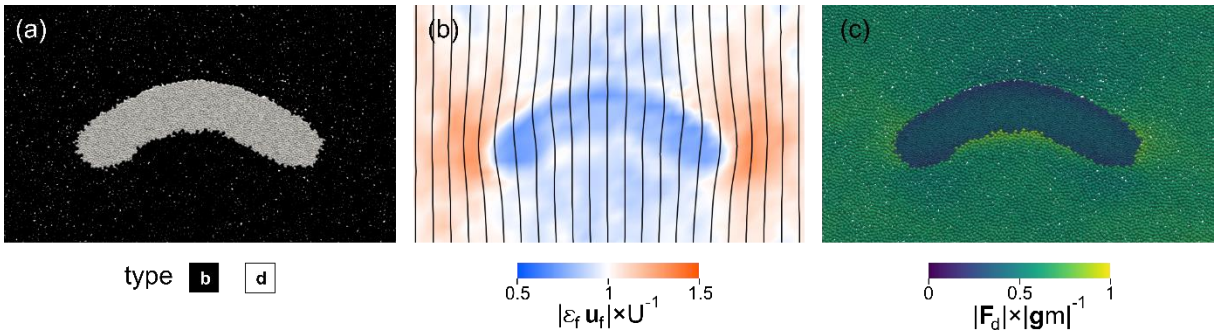

Figure 30 (a) A granular droplet (white) spreads in the bulk phase (black) after t = 2.6 s of simulated time. (b) Gas flow field in the vicinity of a granular droplet. The magnitude of the superficial gas velocity |εuf| is averaged over two vibration periods (0.2 s) and normalized by the inlet velocity U of the fluidized bed. Due to the lower permeability of the granular droplet compared to the bulk phase, the gas shifts around the droplet generating low flow velocities inside the granular droplet (blue field) and high flow velocities in the bulk phase left and right of the droplet (orange fields at the edges of the droplet). (c) Particle based drag force Fd normalized by the weight of the particle |gm|. The lack of gas flow inside the granular bubble reduces the drag force acting on the droplet particles and thus reduces the fluidization level |Fd |×|gm|-1 compared to the bulk particles. The results are taken from simulations with the same settings as described in Figure 29.

During the indentation stage (φ = π to 3/2π) illustrated in row (c) at φ = 5/4π, the bulk particles on top of the granular droplet exhibit nearly no inter-particle contact forces, indicative of a highly mobilized state. Since at φ = 5/4π, $\boldsymbol{v}$ is small in this zone, the mobilization has been completed at this stage of the vibration cycle and the bulk particles do not move relative to the walls anymore. However, the granular droplet clearly exhibits a downward velocity $\boldsymbol{v}$ and starts to indent the subjacent bulk phase as seen in the second column of row (c). This indentation is caused by two contributions: 1) At φ = π the direction of the vibrational acceleration has inverted and points upwards. Thus, the imposed acceleration acts in the opposite direction of the downwards motion of the vibro-gas-fluidized bed and inertially compresses the bed from the bottom. 2) Due to their reduced fluidization during the mobilization stage, the granular droplet particles gain a higher momentum than the surrounding bulk particles and thus start to penetrate the subjacent bulk phase as the bed decelerates, see second column of row (c).

In the subsequent spreading stage (φ = 3/2π to 7/4π), the granular droplet pushes down the bulk phase underneath the droplet and simultaneously compacts this region, forming a dense contact force network as shown in row

(d). Due to this strong force network, the region below the granular droplet consolidates and forms an immobilized zone of growing size. This resembles the jamming process as observed in dense suspensions. For example a rod impacting the surface of a dense suspension creates a solidification front [75]. The immobilized zone obstructs the further vertical penetration of the granular droplet and redirects the droplet particles to penetrate into less consolidated and still mobilized bulk phase regions at the sides of the granular droplet. This can be seen from the particle velocity fields in row (d) and (e), where the droplet particles exhibit considerable lateral motion. The lateral spreading of the granular droplet forms leading edges of the droplet that progress along inclined paths, which - at a later stage - will transform into daughter droplets. Lastly, in the sedimentation stage ($\varphi = 7/4\pi$ to 2π) shown in row (e), the contact force network in the immobilized zone has strengthened further, leading to essentially stagnant particles in the region below the granular droplet. The propagation of the granular droplet particles occurs exclusively at its edges. Bulk particles in the mobilized regions at the sides and on top of the droplet move down and sediment as the vibro-gas-fluidized bed moves up again. The emerging contact forces above the granular droplet provide further evidence for the solidification of the bulk phase due to sedimentation. Finally, the cycle is repeated by the bed reentering the rigid body motion stage shown in row (a). All five stages (a-e) repeat in each vibration cycle leading to the spreading and ultimately splitting of a granular droplet. The motion of particles within and around a granular droplet during a vibration cycle shows similarities to the motion seen in Faraday heaping experiments [117 – 119]. Van Gerner et al. [76] simulated a vibrated box that contained small particles and observed the formation of heaps from an initially flat surface (Faraday heaps). These heaps are due to particle circulation patterns induced by changes in the gas pressure during a vibration cycle. However, in their simulations the particles contact a solid, flat surface and are forced by the gas pressure gradient to circulate back to the center of a heap. In case of a granular droplet, the droplet particles push onto an immobilized zone of particles and can migrate laterally into mobilized regions leading to droplet splitting.

The previously described formation of an immobilized zone is independent of the initial shape of the granular droplet. As confirmed in **Figure 31**, immobilized zones form underneath a granular droplet independent of its shape. All investigated droplet shapes yield ultimately a concave shape comparable to the one seen in **Figure 29** and undergo a binary split. Furthermore, the initial position of the granular droplet only affects the starting time of sinking and splitting but has no significant effect on the splitting behavior itself, as seen in **Figure 32** in section. This observation was made in additional simulations in which a square shaped granular droplet ($D = 50$ mm) was initialized at different positions in the granular bed. With increasing depth of the granular droplet, the droplet sinking/splitting starts with increased delay compared to a droplet located higher up the bed. This is because a fluidization front propagates downwards through the bed once the vibration and the gas flow has been turned on. Since the splitting of a granular droplet only occurs once the vicinity of the droplet is sufficiently fluidized to allow for its lateral spreading (i.e. the granular pressure surrounding the particle is sufficiently low), the onset of sinking is delayed longer the further down the bed the droplet is located.

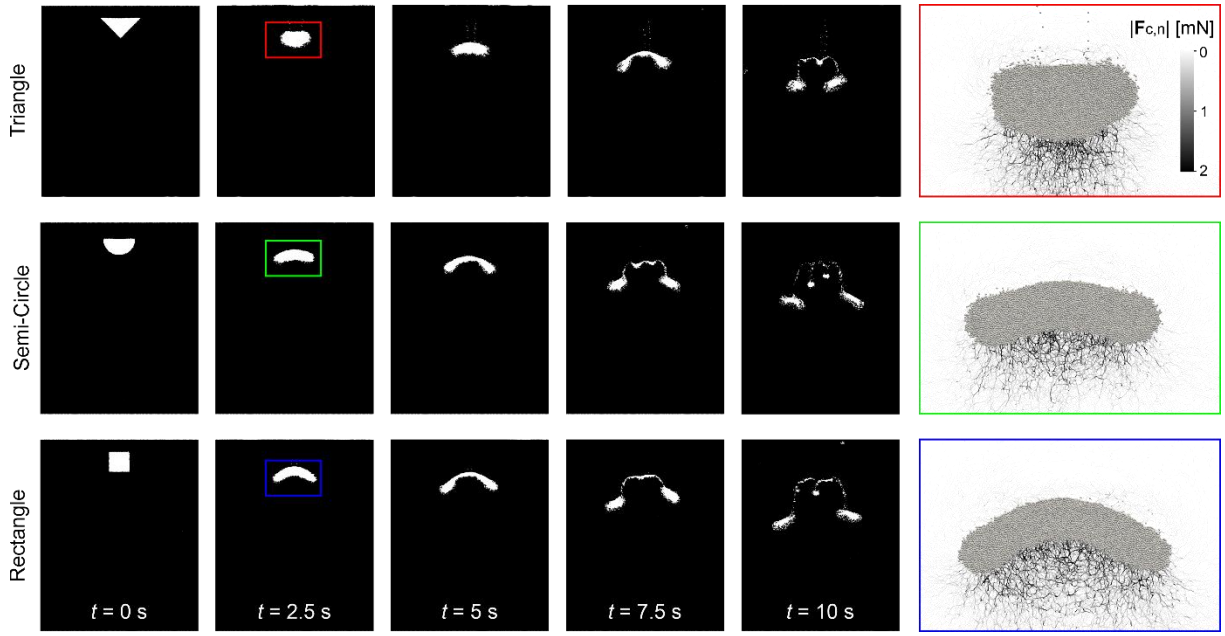

Figure 31 Effect of the initial droplet shape on the splitting of a granular droplet. Three different shapes of a granular droplet (triangle, semi-circle and rectangle) have been studied. The rectangular case is identical to the one in **Figure 29**. All shapes have the same droplet volume, the same distance from the bottom of the bed, and identical particle properties. The bed is agitated with A = 1 mm, f = 10 Hz and U/U_{mf} = 0.97. In all cases the granular droplet yields a concave shape and ultimately performs a binary split. The framed panels on the right show the force chains formed below each granular droplet at t = 2.575 s.

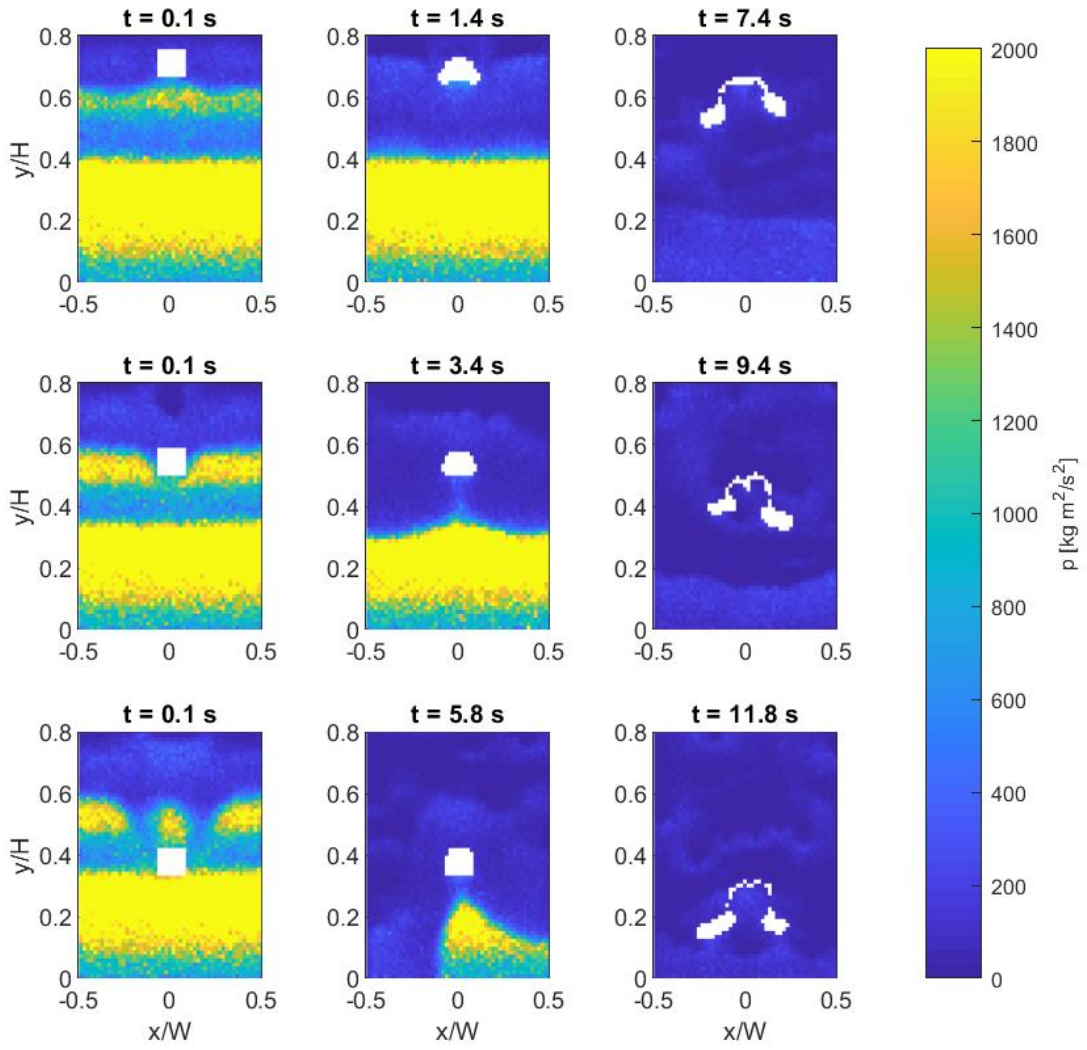

Figure 32 Evolution of the granular pressure field surrounding a granular droplet *(D* = 50 mm) during sinking and splitting. Each row shows a granular droplet (colored white) initialized at the "top" ($y = 2/3H$), "middle" ($y = 1/2H$) or "bottom" ($y = 1/3H$) of a vibro-gas-fluidized granular bed in a box of height H = 0.6 m. The total filling height of the granular bed is $0.77H$. The background color gives the granular pressure spatially averaged on a grid with grid spacing $4.5d_b$ = 7.65 mm and temporally averaged over one vibration period (0.1 s). The results were obtained by CFD-DEM simulations with A = 1 mm, f = 10 Hz and U/U_{mf} = 0.92.

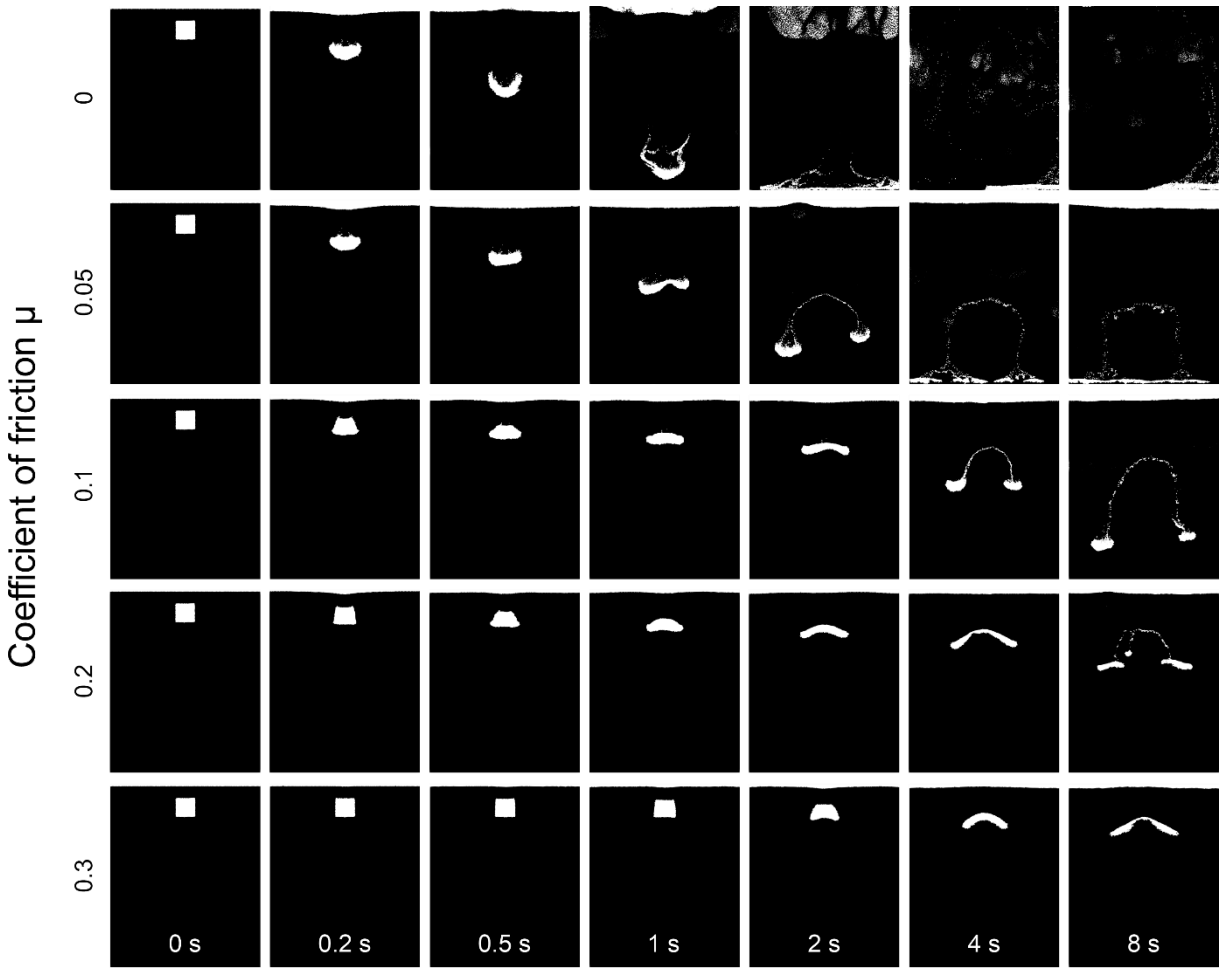

Figure 33 Effect of the coefficient of friction μ on the temporal evolution of sinking granular droplets. Each row shows an individual time series (with increasing μ from top to bottom), where droplet particles (white) and bulk particles (black) share the same value of μ. The results are obtained by CFD-DEM simulations with A = 1 mm, f = 10 Hz and U/U_{mf} = 0.92. For μ = 0, gas bubbles emerged at the top half of the bed after 1 s of simulated time.

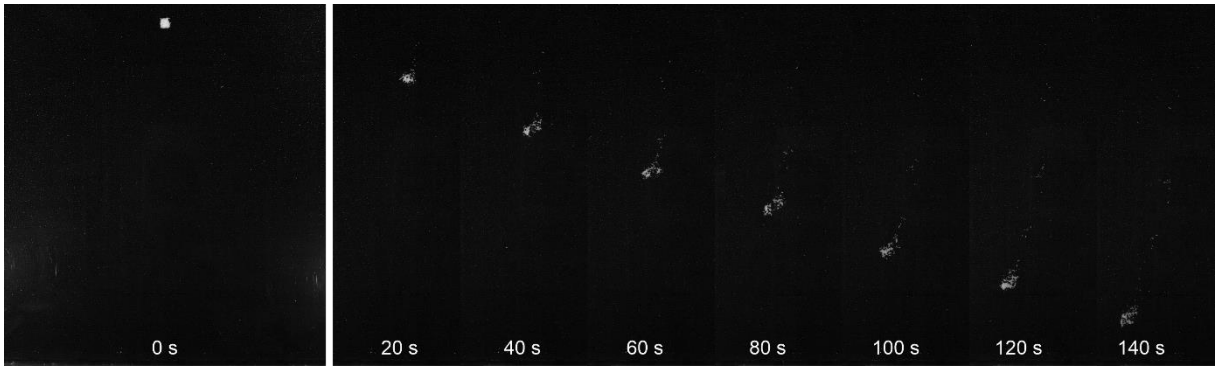

Figure 34 Sinking of a granular droplet with D = 10 mm in a vibro-fluidized bed. The fluidizing gas flow is set to U/U_{mf} = 0.96 and the vibration is set to f = 30 Hz and A = 0.05 mm. Results are obtained by experiments. Particle densities and particle sizes of the granular droplet (white) and the bulk phase (black) are according to **Table 5**.

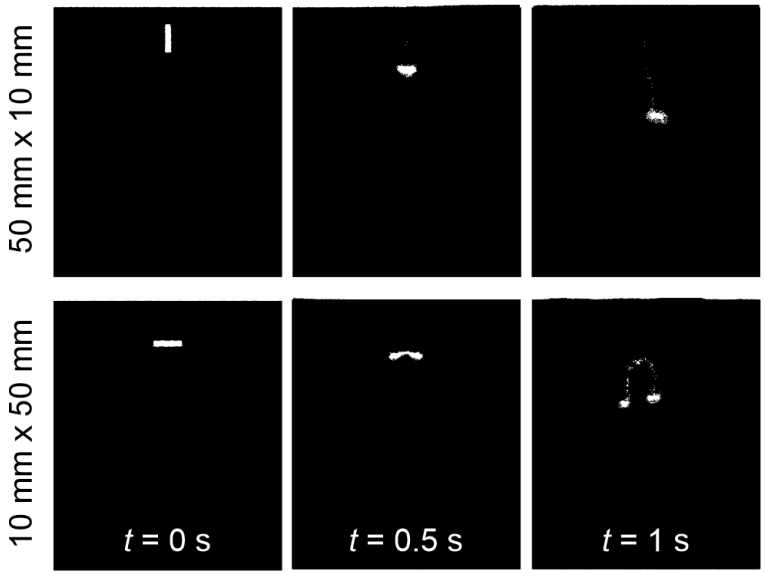

Figure 35 Effect of the aspect ratio of a rectangular granular droplet. A droplet of 10 mm width and 50 mm height sinks and reforms into a single droplet without splitting (top row). A granular droplet of 50 mm width and 10 mm height splits into two daughter droplets. The formed daughter droplets sink without further splitting (bottom row). All results were obtained by CFD-DEM simulations with A = 1 mm, f = 10 Hz and U/U_{mf} = 0.92.

7.4.3 Second binary split

The previous section has demonstrated that underneath a granular droplet there is an immobilized zone characterized by particles with a strong contact force network. This immobilized zone obstructs the direct sinking of the droplet particles and forces the granular droplet to spread and ultimately to split, leading to the formation of two daughter droplets. However, we also observed that the daughter droplets themselves can be subject to another binary split. The data shown in **Figure 36** provides further insight into the mechanism at play during the second split. The top row in **Figure 36** visualizes the velocity of the bulk particles $\boldsymbol{v}$, near the right daughter droplet in the mobilization stage ($\varphi = \pi$) of a vibration cycle. The bottom row in **Figure 36** displays the density and strength of the normal contact forces acting between the bulk particles in the spreading stage ($\varphi = 3/2\pi$) of the vibration cycle. Each row illustrates the temporal evolution of the daughter droplet in the same phase of the vibration cycle. In frames 5.05 s and 7.55 s, the velocity of the bulk particles underneath the spreading granular droplet is lower than the velocity of the mobilized particles above the granular droplet. This implies that although thin, the connecting band of particles between the daughter droplets maintains a stationary zone underneath the center of the connecting band and prevents this zone from mobilizing. The contact force networks in the corresponding frames 5.08 s and 7.58 s demonstrate the existence of strong contact forces in the region underneath the connecting band. Particles in the immobilized zones are strongly consolidated such that the droplet particles contained in the right daughter droplet can only penetrate into the mobilized bulk phase to their right. Analogously, the left daughter droplet particles can only penetrate to their left. Comparison of the first three frames in **Figure 36** (5.05 s, 7.55 s and 10.55 s) reveals that the laterally advancing daughter droplets deplete the connecting band between the two daughter droplets until it ultimately thins out and the connection "ruptures". Simultaneously with the thinning of the connecting band, the velocity of the bulk particles underneath the connection band increases appreciably (see 7.55 s and 10.55 s). The corresponding frames in the bottom row (7.58 s and 10.58 s) show that the strong contact force network underneath the connecting band disappears once the connecting band between the daughter droplets is only a few particles thick or has partially ruptured while networks of dense contact forces prevail directly underneath the granular daughter droplet that has detached. Combining the velocity and contact force information, we observed that once the connecting region between the two daughter droplets is thinner than 10 droplet particles (10.55 s), it can no longer suppress the mobilization of the bulk particles underneath, and the immobilized zone is limited to the region directly

below the forming daughter droplet. After the formation of the new, individual daughter droplets (10.85 s), the same particle flow pattern as the one sketched in **Figure 29** (b) forms around each detached daughter droplet, i.e. the bulk particles at the outer side of each of the daughter droplet mobilize and a strong contact force network is only maintained underneath each daughter droplet but not on its sides (see 10.58 s). Thus, the daughter droplets start to spread towards both sides, reshaping themselves and eventually leading to another binary split of the daughter droplet as seen in the frames 17.55 s and 20.55 s.

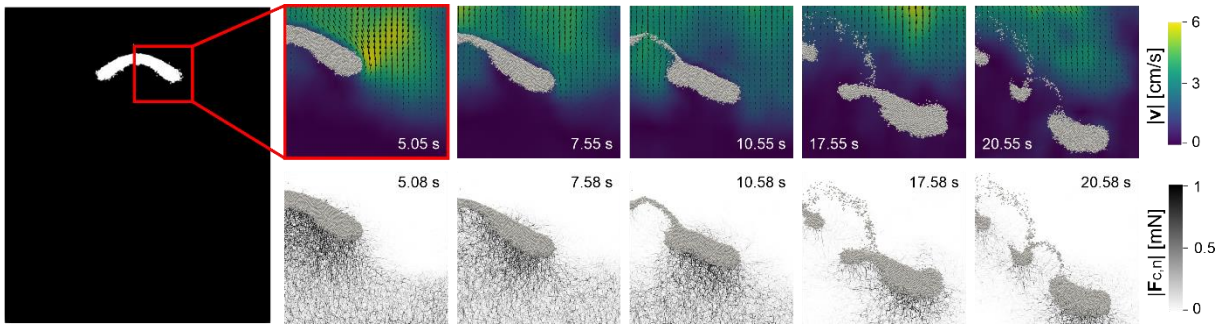

Figure 36 Detachment process of the right daughter droplet and the initiation of a secondary split. The droplet particles are shown in gray; frames in the top row show the particle velocity field at the mobilization stage ($\varphi = \pi$), whereas the frames at the bottom row show the normal contact forces between the bulk particles and are taken in the corresponding spreading stage ($\varphi = 3/2\pi$). Each frame shows the same phase in the vibration cycle. The simulation was performed using A = 1 mm, f = 10 Hz and U/U_{mf} = 0.92. U/U_{mf} is smaller than in **Figure 29** to make the second binary split to occur faster.

7.4.4 Particle requirements for granular droplet fragmentation to occur

In this section, we explore to what extent particle properties such as the coefficient of friction, the particle diameter, and the particle density influence the fragmentation of a granular droplet and the formation of daughter droplets. As these properties are difficult to control experimentally, a numerical parameter study was performed.

A systematic study of the effect of the coefficient of friction μ is presented in **Figure 33**. **Figure 36** summarizes the key observations by comparing a reference case using a coefficient of friction μ = 0.3 (top row) with a case using μ = 0 (bottom row). In both cases, μ is identical for the bulk and droplet particles. In **Figure 36** (a), the time series for μ = 0.3 shows how the initialized square droplet deforms to a cap-shaped droplet, leading to a continuously thinning connection between the two daughter droplets. As already visualized in **Figure 28** (b), also **Figure 36** (b) shows the presence of an immobilized zone underneath the droplet and high solid velocities at the outer regions of the granular droplet allowing for a lateral spreading and ultimately a binary split of the droplet. In contrast to the familiar behavior of the droplet for μ = 0.3, the granular droplet evolves very differently for μ = 0. Here, the droplet deforms in an opposite fashion as for μ = 0.3, yielding a U-shaped granular droplet. The droplet sinks unimpededly through the bulk phase with a high velocity until, after only 1.1 s, it reaches the bottom of the bed. While sinking, the droplet broadens to some extent whereby thin trails of particles shed from the outer corners into the bulk phase. Importantly for μ = 0, the granular droplet does not undergo a binary split, but instead, the droplet behaves very similar to a large liquid droplet sinking in an immiscible liquid of smaller density; see [28] [77] [78] [79] for comparison. The velocity field of the bulk phase for μ = 0 in **Figure 36** (b) reveals the absence of an immobilized zone underneath the granular droplet and a high downward directed velocity at the top of the granular droplet, allowing the granular droplet to rapidly migrate downwards. The displaced bulk particles flow in a large vortex structure to the top of the droplet. The centers of these vortices are located at the trailing edges of the granular droplet. This liquid-like behavior of the granular droplet is explained by the fact that the dense and less fluidized particles in the granular droplet can easily push aside the lighter particles of the bulk phase due to the absence of inter-particle friction. As soon as inter-particle friction is introduced, the sinking speed of the granular droplet is reduced and binary droplet splits occur; see **Figure 33**. Hence, we can conclude that inter-particle friction is critical for the formation of an immobilized zone underneath the droplet and for a binary split to occur.

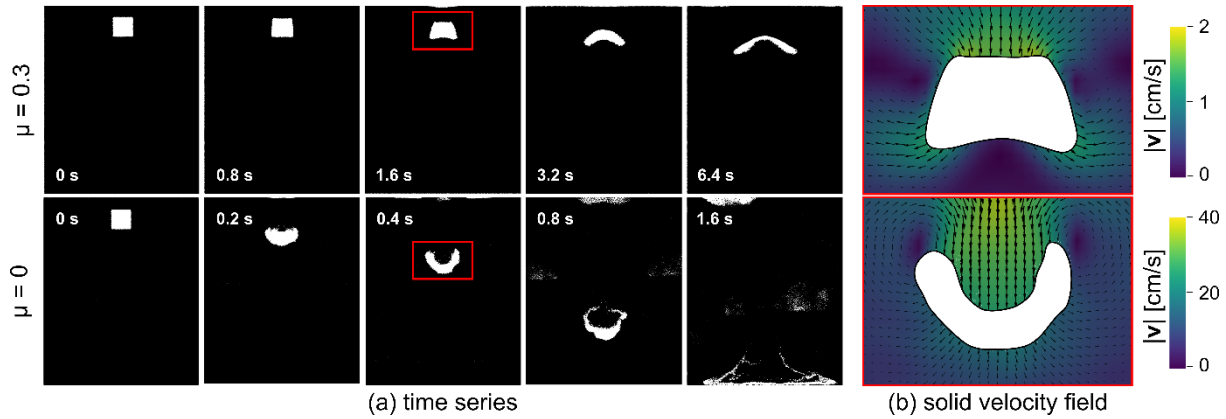

Figure 37 Influence of the coefficient of friction μ on the sinking and fragmentation dynamics of a granular droplet of D = 50 mm. (a) Time series of granular droplet dynamics as obtained by CFD-DEM simulations using A = 1 mm, f = 10 Hz, U/U_{mf} = 0.84. Top row: simulation with a friction coefficient of μ = 0.3; Bottom row: Friction coefficient μ = 0. (b) Velocity of the bulk particles surrounding the granular droplet (white area) in the framed regions at t = 1.6 s (top row) and t = 0.4 s (bottom row). The background color quantifies the magnitude of the bulk particle velocity $|\boldsymbol{v}|$. The velocity data are time averaged over 0.1 s. The simulation used a comparatively low value of U/U_{mf} to reduce the emergence of large gas bubbles in the zero friction simulation.

The influence of particle density and particle size on the splitting behavior is shown in **Figure 39**. This figure contrasts six simulations of varying relative particle size (d_d/d_b, three rows) and particle density (ρ_d/ρ_b, two columns). For each case, the position of the granular droplet and the gas flow field around the granular droplet are shown after a simulated time t. The gas flow field is quantified by the superficial velocity magnitude normalized by the inlet velocity U of the vibro-gas-fluidized bed. The gas velocity is averaged over one vibration period (0.1 s) to compensate for high-frequency gas fluctuations. **Figure 39** (a) shows the already known case of a granular droplet with particles of smaller size (d_d/d_b = 0.645) and higher density (ρ_d/ρ_b = 2.4) than the surrounding bulk particles (standard case as described in **Table 5**). In the standard set-up the granular droplet sinks and splits into two daughter droplets. The corresponding gas velocity field displays the existence of a heterogeneous gas flow, where the gas velocity is higher around than within a granular droplet. In their original work, McLaren et al. [56] have argued that in case there is a size difference between the bulk particles and the particles in the granular droplet a heterogeneity in the gas flow is induced due to the lower permeability of the smaller granular droplet particles compared to the larger bulk particles. They further hypothesized this heterogeneity to be the major reason for the sinking and splitting of a granular droplet. To test this hypothesis, additional simulations varying d_d and ρ_d were assessed. For the case of equal particle size (d_d/d_b = 1) and density (ρ_d/ρ_b = 1), **Figure 39** (d), there is a homogenous bed permeability and thus a homogenous gas velocity across the bed. We further observed no coherent motion of the square-shaped initialized granular droplet over 15 s, but only diffusive mixing of the granular droplet particles with the surrounding bulk. Diffusion is strongest in the vertical direction with a diffusion coefficient of $\mathcal{D}_y$ = 0.97 mm²/s, see **Figure 38**. The absence of any directed motion of the granular droplet indicates that a granular droplet needs a driving size difference or density difference to display coherent motion. More importantly, this reference case confirms that the combination of vibration and gas flow applied does not introduce any large-scale convection patterns in the bed, which could otherwise influence the motion of the granular droplet. **Figure 39** (b) shows a simulation in which a granular droplet contains smaller particles, but of the same density as the surrounding bulk particles. Here, one observes a lower gas velocity in the granular droplet. However, despite this gas flow heterogeneity, the granular droplet does not show the expected sinking and splitting behavior, but instead rises. We hypothesize that this behavior is due to the lower U_{mf} of the particles in the granular droplet. Having the same density but a smaller diameter than the bulk particles leads to a lower U_{mf} of the droplet particles compared to the bulk particles and the droplet particles are more easily fluidized. This increase in fluidization due to the lower U_{mf} overcomes the decrease of gas flow through the droplet, leading the droplet to rise. Thus, a heterogeneous gas flow alone does not result

in a sinking and splitting granular droplet. In a further simulation, **Figure 39** (c), a case is modelled in which the particles in the granular droplet and the bulk have the same diameter, but the particles in the granular droplet have a higher density than the bulk particles. Since all particles have the same diameter, a fairly homogenous gas flow is established in the bed. Nevertheless, the granular droplet sinks, spreads and thins leading ultimately to a binary split. This finding indicates that density differences are the main driver for the splitting of a granular droplet. Only if the droplet particles are appreciably denser than the surrounding bulk particles, the region underneath the droplet can create an immobilized zone that is critical for droplet splitting to occur. To further reinforce this finding, **Figure 39** (e) and (f) show the results of two cases, where the droplet particles are larger than the bulk particles and the droplet particles are either denser than the bulk particles (e) or equally dense (f). In both cases, the gas flows preferentially through the granular droplet and the gas flow field is inverted to the ones found in (a) and (b). Despite this inversion, only in case (e) the granular droplet sinks and spreads laterally, whereas in (f) the droplet forms a plume that rises to the freeboard of the bed. A comparison of **Figure 39** (a, c, e) reveals a longer time until the split of the granular droplet occurs with increasing d_d/d_b. A reason for the accelerated splitting dynamics could be that the heterogeneous gas flow around the droplet (in particular around its outer corners) helps to mobilize the surrounding bulk particles and facilitates the lateral spreading step discussed in **Figure 29** (c) and later in section 7.4.5.

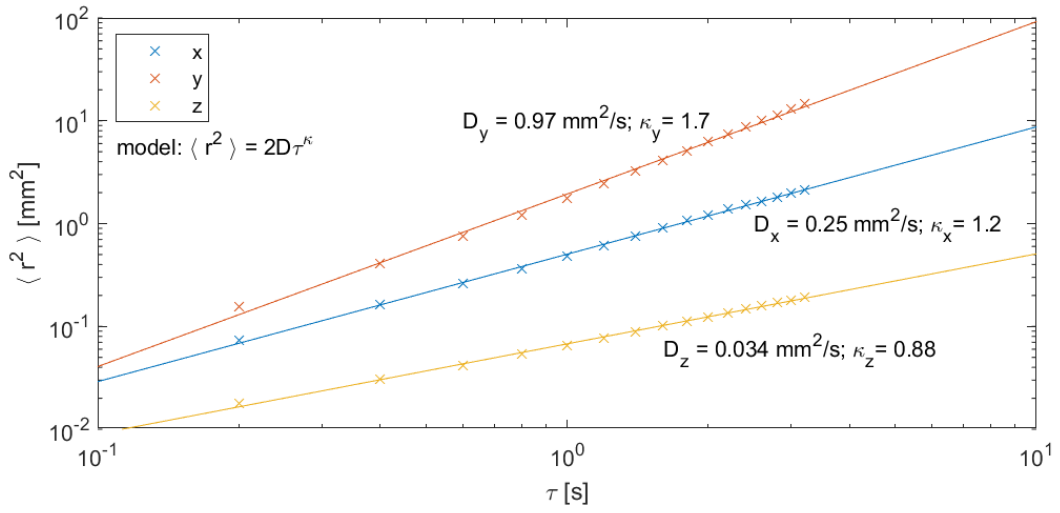

Figure 38 Analysis of the diffusive behavior of a granular droplet in a vibro-gas-fluidized bed in case the granular droplet particles have the same density and diameter as the surrounding bulk particles, as see in **Figure 39** (d) in the manuscript. To this end, the mean square displacement $\langle r_i^2 \rangle$ of all granular droplet particles was evaluated for each direction ($i = x, y, z$) for various lag times (τ), where τ is the elapsed time between consecutive observations of a granular droplet particle. The diffusion coefficients $\mathcal{D}_i$ were calculated from a linear fit according to the model $\langle r_i^2 \rangle = 2\,\mathcal{D}_i\,\tau^{\kappa}$. $\mathcal{D}_i$ is greatest in *y*-direction (0.97 mm²/s) and smallest in *z*-direction (0.034 mm²/s). Thus, the overall diffusion coefficient $\mathcal{D}$ will be dominated by $\mathcal{D}_y$. The power κ of the fitted model indicates that a super-diffusive behavior ($\kappa > 1$) is present in *x*- and *y*-direction, whereas restricted diffusion ($\kappa < 1$) is seen in *z*-direction. This behavior is expected from the setup of the vibro-gas-fluidized bed. Due to the small distance between the front and back wall, the motion of the particles is restricted in *z*-direction. Since the external vibration is applied in the *y*-direction, particles will experience a strong agitation in *y*-direction, leading to super-diffusive motion. Importantly, all exponents κ are smaller than 2, i.e. no convective motion occurring.

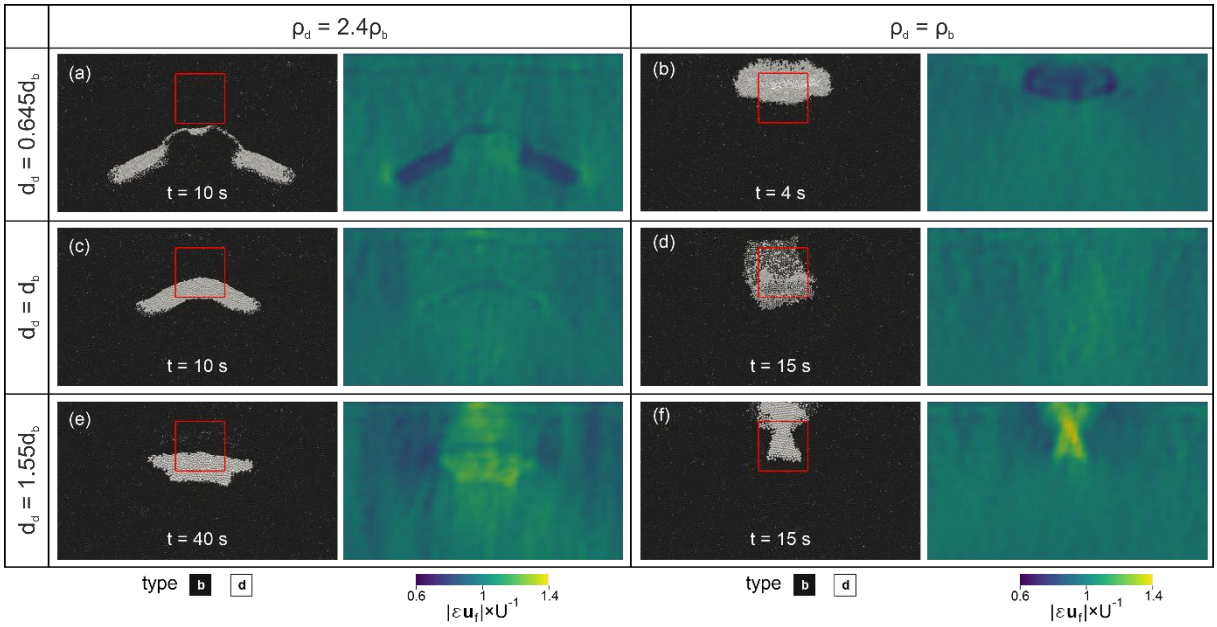

Figure 39 Numerical study of the effect of the density ratio ρ_d/ρ_b and size ratio d_d/d_b between the droplet and the bulk particles on the granular droplet dynamics. Within a row, d_d/d_b is constant (top to bottom: 0.645, 1, 1.55) and within a column ρ_d/ρ_b is constant (left to right: 2.4, 1). In all simulations, d_b = 1.7 mm, ρ_b = 2500 kg/m³, A = 1 mm, f = 10 Hz and U/U_{mf} = 0.92. Each simulation result (a-f) is visualized in two panels: the left panel displays the instantaneous shape of the granular droplet (white) surrounded by the bulk particles (black) after a given time t. The red square marks the initial position of the granular droplet. The right panel shows the normalized superficial velocity of the gas flow $|\varepsilon_f \boldsymbol{u}_f|/U$ (color-coded) around the same granular droplet at t. The gas velocity data was averaged over one vibration period (0.1 s).

7.4.5 Effect of vibration strength, fluidization level and droplet size on the splitting angle

So far, we have established that the formation of an immobilized zone below the granular droplet is critical for droplet spreading and splitting and that this zone originates from frictional inter-particle contacts caused by a density difference between the bulk and droplet particles. Now, we further study the dynamics of a splitting granular droplet and how it is affected by changes in the granular droplet size D and two external agitation parameters, i.e. the vibration strength Γ and the fluidization level U/U_{mf}. As a quantification of the splitting dynamics, we use the splitting angle formed between the trajectories of two granular daughter droplets originating form a splitting event. It is expected that the extent of the immobilized zone will affect the trajectories of the daughter droplets, i.e. a larger extent of the immobilized zone should lead to a higher splitting angle α. Here, we relied on an experimental approach, because the experiments were found to be less prone to gas bubbling than the numerical simulations.

The inset of **Figure 40** (a) shows the trajectories of a splitting granular droplet with D = 30 mm using U/U_{mf} = 1.01, f = 30 Hz and A = 0.05 mm. As can be seen from **Figure 40** (a), the initial value of α is close to 180° while it rapidly decreases with the spreading of the droplet. Once the two daughter droplets have detached from each other fully, α reaches an asymptotic value and the daughter droplets continue to descend at this asymptotic angle until they split again. The value of α_{asym} obtained was subsequently used to qualitatively describe the extent of the immobilized zone that has built up underneath the daughter droplets. A high value of α_{asym} corresponds to a large immobilized zone and vice versa. In **Figure 40** (b-d) the values of α_{asym} are plotted as a function of the vibration strength Γ, the fluidizing gas velocity U/U_{mf}, and the initial droplet size D.

When the vibration strength is increased, α_{asym} decreases monotonically, as shown in **Figure 40** (b). Within the parameter range used in this work, the effect of the vibration strength on the asymptotic angle was the same (within a standard deviation) whether the amplitude or the frequency was changed, while the other was held constant, i.e. only the effective value of Γ is important for the dynamics of the daughter droplets. The assumed likely explanation is that an increase in vibration strength increases the energy input into the vibro-gas-fluidized

bed and increases the overall mobilization of the bulk particles, such that the granular droplet can penetrate the subjacent bulk phase more easily, leading to a decreasing α_{asym}. Further evidence of this facilitated vertical penetration is obtained when probing the sinking velocity of the daughter droplets and decomposing it into a vertical and horizontal velocity component, see **Figure 41**. An increase in Γ accelerates the vertical sinking velocity, whereas the horizontal velocity of the daughter droplets, i.e. their lateral spreading velocity, is less affected. This, in turn, leads to an increase in the ratio of downward motion relative to the lateral motion of the daughter droplets and thus a smaller angle α_{asym} as can be seen from **Figure 41** (a). Unlike the effect of Γ, an increase in U/U_{mf} only leads to marginal changes in the asymptotic splitting angle within the precision of a standard deviation of the experiments, see **Figure 40** (b). The reason for this invariance is that an increase in U/U_{mf} increases the mobility of both, the bulk phase beneath the granular droplet and especially the bulk phase at the leading edges of the splitting droplets due to gas flow heterogeneity. This can be seen in **Figure 41** (b), where an increase in U/U_{mf} increases both the horizontal and vertical velocity of the daughter droplets. Next, the effect of the granular droplet size D on the splitting angle is inspected. **Figure 40** (d) shows that an increasing size of the granular droplet leads to an increase in α_{asym}. This is due to an increasing size of the immobilized zone with increasing droplet size. In fact, we found that a minimum size for the granular droplet is required to observe the splitting of a droplet. A granular droplet with $D \leq 10$ mm does not appear to form a sufficiently large, immobilized zone to give rise to droplet splitting; instead, a droplet of size $D \leq 10$ mm simply sinks vertically without undergoing splitting, as can be seen in **Figure 34**. This observation also explains why daughter droplets can only undergo a limited number of binary splits during their descent. Complementary numerical simulations have confirmed this minimum droplet size to yield droplet splitting. We have performed two additional simulations of granular droplets with a low and large aspect ratio (ratio of droplet height to width) to investigate the effect of the height and width of the droplet: (i) a droplet of 50 mm height and 10 mm width, and (ii) a droplet of 10 mm height and 50 mm width; see **Figure 35**. For the high aspect ratio droplet, the particles reshape into a single droplet that sinks without any splitting. For the droplet with the lower aspect ratio we could observe a binary split into two daughter droplets of almost the same size. After the split, the daughter droplets sink without any further splitting – resembling the case of a sinking droplet with $D = 10$ mm. These observations indicate that not only the height, but also the width of a granular droplet is important for the splitting to occur (and hence also for the formation of an immobilized zone underneath the droplet). It appears that the width of the droplet is directly correlated with the width of the immobilized zone below it. Indeed, both are of comparable width, as seen in **Figure 29**, as long as the droplet is sufficiently high.

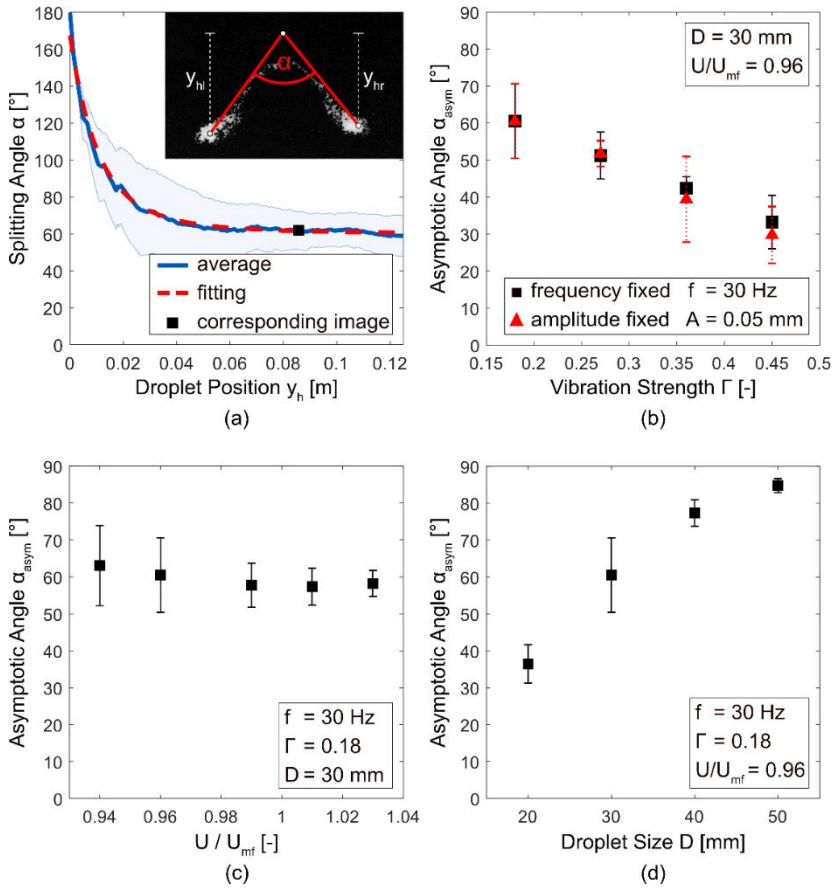

Figure 40 Splitting angle as a function of vibration strength, fluidization level and droplet diameter: (a) Splitting angle α of a granular droplet as a function of vertical distance travelled y_h. The solid blue line represents the average splitting angle and the blue shaded area represents the standard deviation based on three repetitions. The dashed red line is fitted using $\alpha(y_h) = k_1 e^{-k_2 y_h} + \alpha_{asym}$. The inset shows the trajectories of the two daughter droplets evolving from a granular droplet of size D = 30 mm for U/U_{mf} = 0.98, f = 30 Hz and A = 0.05 mm. The red arc shows the construction of α at y_h = 8.5 cm. (b) Effect of vibration strength on the asymptotic angle; the black squares plot α_{asym} for D = 30 mm and f = 30 Hz with varying A and the red triangles plot α_{asym} for D = 30 mm and A = 0.05 mm for varying f. (c) Effect of U/U_{mf} on α_{asym} for D = 30 mm, f = 30 Hz and Γ = 0.18. (d) Effect of granular droplet size D on α_{asym} for f = 30 Hz, Γ = 0.18 and U/U_{mf} = 0.96. The error bars in (b), (c) and (d) represent the standard deviation based on three repetitions.

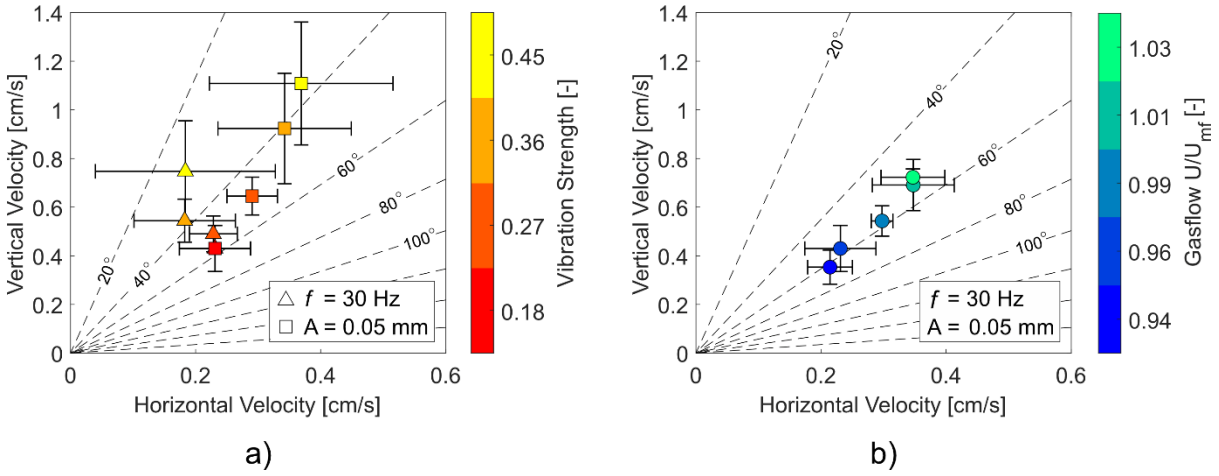

Figure 41 Vertical and horizontal velocities of the sinking daughter droplets during their first split as a function of vibration strength (a) and gasflow (b). The results represent the averaged velocities of the leading edges as obtained by digital image analysis of the experiments (see S1 in [23]). The dashed lines in the background plot the asymptotic angle through $\alpha_{asym} = 2\tan^{-1}\left(\frac{v_{hor}}{v_{vert}}\right)$. The error bars show the standard deviation based on three experimental runs.

The numerical data plotted in **Figure 37** and **Figure 33** reveal that the splitting behavior is affected by the coefficient of friction μ of the particles. Indeed, the asymptotic splitting angle monotonically increases with an increasing coefficient of friction, starting at $\alpha_{asym} = 38°$ for $\mu = 0.05$ and growing up to $\alpha_{asym} = 93°$ for $\mu = 0.3$ as can be seen in **Figure 42**. This result is in agreement with the relevance of an immobilized zone for droplet splitting. An increased coefficient of friction yields a larger immobilized zone underneath the granular droplet such that the droplet spreads out further laterally leading in turn to a flatter trajectory, i.e. a larger splitting angle. A full analysis of the dynamic evolution of the splitting angle with droplet motion can be seen in **Figure 42**.

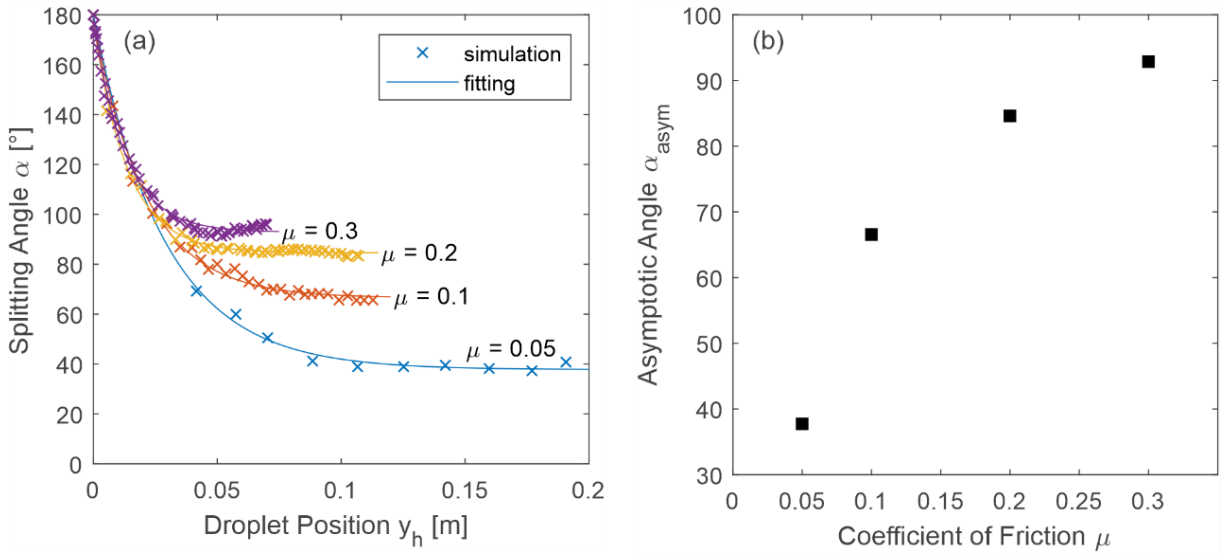

Figure 42 Effect of the coefficient of friction μ on the splitting angle α of a granular droplet with $D = 50$ mm. (a) evolution of α along the distance travelled y_h of a granular droplet for various values of μ. (b) The asymptotic splitting angle α_{asym} increases monotonically with increasing μ. The results in (a) and (b) were obtained by CFD-DEM simulations with $A = 1$ mm, $f = 10$ Hz and $U/U_{mf} = 0.92$.

7.5 Conclusion

In this study, we have explored the physics behind the sinking, spreading and splitting of "granular droplets" in a pseudo-two-dimensional granular bed. To this end, an assembly of granular particles (termed granular droplet) was submersed in a bed composed of bulk particles with a larger particle diameter and lower density. The bed was agitated simultaneously by vertical vibrations and a fluidizing gas flow (vibro-gas-fluidized bed). Our experiments showed that a granular droplet does not sink in a direct downwards motion, but instead, moves preferably laterally, causing a spreading and thinning of the granular droplet and ultimately its splitting into two daughter droplets. These daughter droplets sink further and can undergo subsequent splitting events. Despite visual similarities with the Rayleigh-Taylor-induced fragmentation of liquid droplets falling in a miscible liquid of lower density, the mechanism causing the splitting of a granular droplet is different. Numerical simulations were used to reproduce the phenomenon and demonstrated that the higher density of the particles forming the granular droplet compared to the density of the surrounding bulk particles creates an immobilized zone underneath the granular droplet. This immobilized zone obstructs the direct downwards motion of the droplet and induces the formation of two laterally moving daughter droplets. These daughter droplets stay initially connected, which maintains an immobilized zone underneath the elongated droplet, and thus they descend on inclined trajectories around this zone. Once the connecting band between the two forming daughter droplets is sufficiently thin, the weight of the connecting band is insufficient to sustain further an immobilized zone. The disappearance of the immobilized zone initiates another binary split of each daughter droplet.

Numerical studies demonstrated further that a density difference between the bulk and the droplet particles is a key requirement for a splitting event to occur. Although size differences between the droplet particles and the bulk particles lead to a preferential flow of the gas through the region of the larger particles due to their higher permeability, this heterogeneous gas flow alone is not sufficient to cause a droplet to split. The formation of an immobilized zone further requires both inter-particle friction and a minimum droplet size; otherwise, the denser particles form a single droplet that sinks without fragmentation, similar to a droplet in an immiscible fluid. Additional experimental studies showed that the size of the immobilized zone increases with increasing initial droplet size and decreasing vibration strength, whereas U/U_{mf} does not seem to extent the size of the immobilized zone appreciably.

The presented work has elucidated the physics driving the splitting of a granular droplet in a vibro-gas-fluidized bed. However, there remains one open question: Why do the denser particles remain aggregated in the form of droplets instead of percolating through the bed as individual particles although a binary granular material does not possess any surface tension? Royer et al. [80] have found attractive forces such as van der Waals interactions and capillary bridges to cause the clustering of particles in free-falling streams of granular matter resembling the surface-tension-driven Plateau–Rayleigh instability. However, the aggregation of granular particles as observed in our research must be driven by another mechanism, as neither of these attractive forces have been implemented in the numerical simulations that predict well the experimental work. We hypothesize, that size effects and a difference in inter-particle momentum transfer could contribute to this aggregation behavior. Yet, elucidating the fundamental mechanism behind this aggregation would demand further investigations on granular droplets.

8 The onset and dynamics of avalanches in a rotating cylinder: From experimental data to a new geometric model

Adapted from: McLaren, C. P., Leistner, B. J., Pinzello, S., Cano-Pleite, E., & Müller, C. R. (2022). The onset and dynamics of avalanches in a rotating cylinder: From experimental data to a new geometric model. Physical Review E (Under Review)

8.1 Abstract

Particle image velocimetry has been applied to measure particle velocities on the free surface of a bed of particles within a rotating cylinder during avalanching. The particle velocities were used to examine the validity of existing avalanche models and to propose an alternative model. The movement of particles depends on their location on the surface of the bed: particles located near the center of the bed travel the farthest, while the distance travelled decreases at an increasing rate for particles located farther from the center. The start of an avalanche can be determined to a single initiation point, that can also be located on the bottom half of the bed; the avalanche quickly propagates through the entire free surface, with 90 % of the surface in motion within 257 ms (approximately 20 % of the total duration of an avalanche). The experimental insight is used to formulate a new geometric model, in which three equal sized sections flow down the bed during an avalanche. The predictions of the model are confirmed by experimental mixing measurements.

8.2 Introduction

Rotating drums are key for the processing of materials in the mineral, ceramic, metallurgical, chemical, pharmaceutical, waste and food industries [2 – 15]. A rotating cylinder can operate in different regimes. Among them, the avalanching regime is a quasi-periodic motion that is observed at low rotation speeds. In the avalanching regime the bed rotates as a rigid body until a section of the bed breaks off and moves down the free surface as an avalanche. The avalanche reduces the angle that the free surface of the bed forms with the horizontal. **Figure 43** visualizes a simple geometric model of the bed surface before an avalanche (angle θ_s) and after an avalanche (angle θ_t). Following an avalanche, the bed returns to rigid body rotation and the angle between the bed's free surface and the horizontal increases until the next avalanche is initiated. Following the work of Bak *et al.* [81] of self-organized criticality, avalanching within rotating cylinders has received considerable attention [125 – 127].

Today there exist multiple competing models for the avalanching regime [82]. Metcalfe *et al.* [12] presented a model for particle mixing in the avalanche regime and compared predictions from their model with results from experiments performed in a pseudo two-dimensional rotating cylinder. The basis of their model was a geometric argument that the result of an avalanche event is to transport a wedge of material from the top half of the surface (light blue in **Figure 43**) down the free surface such that after the avalanche it occupies a new wedge at the bottom half of the free surface. The lines defining these wedges are the free surfaces of the bed before and after the avalanche has occurred and it was assumed that no particles outside of this wedge are affected by the avalanche. Based on this model it was argued that the problem of mixing within a system operating in the avalanching regime may be decomposed into two parts: the transport of wedges and mixing within wedges. In the absence of more detailed information, perfect mixing within the wedges was assumed. This wedge model was refined further by McCarthy *et al.* [83] .

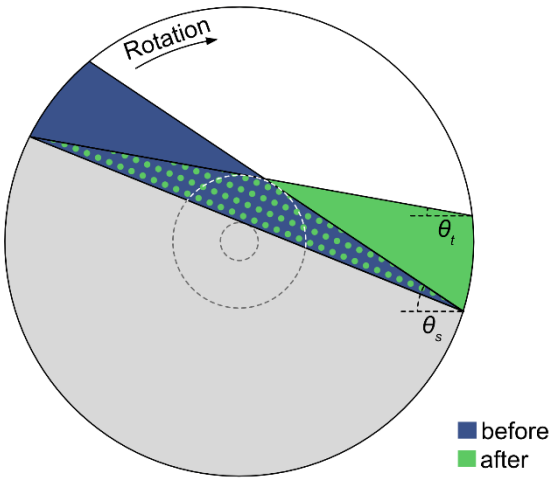

Figure 43 Geometric models of an avalanche where θ_s is the angle between the bed surface and the horizontal before an avalanche and θ_t is the corresponding angle after an avalanche: the model proposed by Metcalfe *et al.* [12] has the purely blue wedge falling down to the purely green wedge. The model proposed by Lim *et al.* [13] starts width a wedge made of all areas containing blue falling down to the wedge of fully green plus green spotted.

Lim *et al.* [13] performed positron emission particle tracking (PEPT) studies of sand rotated in a horizontal cylinder that was operated in the avalanching regime. The PEPT data revealed that, on average, a particle on the free surface was involved in more than one avalanche before it rejoined the bulk of the bed in rigid body rotation. The average number of avalanches required for a particle to traverse the free surface was found to depend on the rotational Froude number (Fr = $\omega^2 R/g$), where ω is the rotational speed, R is the radius of the cylinder and g is the gravitational acceleration. At low values of Fr, particles remained on the free surface for an average of 4.25 avalanches, whereas this number drops to one avalanche when the bed was operated in the rolling regime with Fr = 1.47×10^{-4}. They found the average number of avalanches required for a particle to traverse the free surface to linearly decrease with increasing Fr. These observations do not support the geometric wedge model of avalanches proposed by Metcalfe *et al.* [12] since the geometric model implies that particles traverse the free surface in a single avalanche. In light of their observations, Lim *et al.* [13] proposed a modified wedge model in which the centroid of the avalanching material moves a distance 1/3 of the chord length down the free surface, where l is the length of the free surface (see **Figure 43**).

So far, studies that have investigated mixing in the avalanching regime in rotating cylinders have not tracked the overall motion of all particles. Lim *et al.* [13] tracked only a single particle using PEPT. Du Pont *et al.* [84] tracked the flowing surface averaging the velocities along the surface flow. Kiesgen de Richter *et al.* [85] studied grain rearrangements by using a camera and observing the acoustic amplitude across the bed with using a piezo transducer and receiver, allowing them to observe changes in the weak contacts, i.e. contacts with less than the designated cutoff force. Kiesgen de Richter *et al.* [85], Gravish and Goldmann [86] and Zaitsev *et al.* [87] observed precursors to avalanches whereby small changes in the packing lead to small rearrangements of the free surface but surface flow did not occur. Zaitsev *et al.* [87] observed a slow relaxation of particle displacements to an equilibrium position after the avalanche. Both Kiesgen de Richter *et al.* [85] and Zaitsev *et al.* [87] observed precursors to avalanches, where small changes in the packing lead to instabilities but flow of the surface did not occur.

In order to examine the validity of the geometric models proposed by Metcalfe *et al.* [12] and Lim *et al.* [13], Particle Image Velocimetry (PIV) is applied in this work to investigate the motion of the particles on the bed surface during avalanches in a horizontal rotating cylinder. Utilizing our experimental findings, an alternative geometric model for mixing during avalanching is proposed and compared against experimental measurements.

The DEM modelling of avalanching has been reported with a focus on the initiation mechanism of the avalanches [134 – 136], The modelling of the full avalanching process remains difficult, due to the inherent hysteresis of granular material (e.g. angle of repose) [88] when switching between static and flowing states. Indeed, recent simulation works on avalanching, caution to that the results obtained are qualitative rather than quantitative [89]. DEM simulations also require a large set of pre-determined particle properties such as the elastic modulus and Poisson's ratio, and particle interaction properties such as the coefficients of restitution and friction. On the other hand, our model provides a simple, yet realistic description of mixing during avalanching.

8.3 Experimental Setup

In this work three drums of different diameters, see **Table 7**, were studied. The drums were constructed out of clear Perspex with walls of thickness 10 mm, allowing two cameras an unobstructed view to the top surface and the side of the drums. Drum 2 was filled with particles to fill levels ranging from 20 % to 70 % with 5 % increments. Three differently sized spherical particles, as shown in **Table 8** were studied. In order to perform PIV, 10 % of the particles though otherwise identical, were darker colored, to allow tracking during the PIV image correlation. The light-colored particles are purchased clear but quickly become opaque with usage. When first used the clear particles severely hinder the view on the black ballotini below the very top layer and with usage it becomes completely impossible to see through them. Therefore, we consider only to have filmed the top layer. The cylinder was driven by a motor (Maxon EPOS 2 24/5) and the free surface of the bed was imaged using a high-speed camera (Nikon, 496RC2) with a frame rate of 100 fps and a resolution of 1280x1024 pixels for PIV purposes. A Canon EOS camera filmed the side of the drum, to determine the slope of the free surface of the bed. In order to avoid possible effects of visual distortion caused by the plexiglass walls, the top 5 % of the free surface is discounted for the determination of the distances traveled by the particles. The bottom 10 % will be discounted due to particles overtaking each other, explained later in the manuscript.

The particle velocities were calculated using the MATPIV 1.6.1. software [90]. The size of the PIV interrogation window was iteratively reduced from 64x64 to 32x32 pixels, using four iterations. Once the velocities were determined, a signal-to-noise filter (s/n = 1.3) and global and local mean filters were applied to detect outliers [41]. To ensure statistical significance of the results, 14-20 avalanches were averaged. The onset of avalanching was defined as the time when the first particle assembly (PIV window) exceeded a threshold velocity of 3 mm/s. This threshold velocity was found to have a negligible impact when set between 1mm/s and 20 mm/s.

Table 7 Drums

	Drum 1	Drum 2	Drum 3
Inner diameter *D* [mm]	94	140	290
Length [mm]	400	400	400

Table 8 Spherical particles

	Ballotini 1	Ballotini 2	Ballotini 3
Diameter *d* [m]	1.0 – 1.3	2.0 – 2.4	2.85 – 3.45
Material	glass	glass	glass

8.4 Results

Figure 44 shows the time evolution of the slope of the free surface of the bed for drum diameters of 94 mm, 140 mm, and 290 mm. For all drum diameters the evolution of the slope of the free surface shows a "sawtooth" pattern that is characteristic of the avalanching regime; individual avalanches can be identified as a rapid decrease in the slope of the free surface and between avalanches the slope increases linearly with time, indicating rigid body rotation.

It can be observed that avalanching is a quasi-periodic phenomenon with fluctuations in both the magnitude of the slope change during an avalanche and the time between successive avalanches. In agreement with Daerr *et al.* [33] the avalanches appear to become more regular as the drum diameter is increased. This was also observed by Daerr et al. [33] when increasing the rational speed, i.e., the Froude number. In agreement with Daerr et al. [33] the avalanches appear to become more regular as the drum diameter is increased, i.e. increasing the Froude number. The change in surface angle over an avalanche event increases with decreasing drum size, i.e., rising from 1.5° for D = 290 mm to 2.1° for D = 94 mm. This is consistent with the work of Balmforth and McElwaine, who showed that as d/D increases so does the change in surface angle during an avalanche event [91].

In the following, the particle motion at the start of an avalanche will be considered. Rearrangements on the surface as precursors described in previous studies were observed but are outside of the scope of this of this study [85]. Rearrangements on the surface, described in previous studies [85] as precursors to an avalanching event were observed but no interrogation window exceeded the avalanching threshold velocity of 3 mm/s

The avalanche's initiation time was found to be insensitive to this velocity threshold. When varying the threshold between 1 and 20 mm/s, the initiation time is delayed at most by 20 ms, which is less than 2 % of the duration of an avalanche. Furthermore, the location of the initiation point of the avalanche is unaffected by the variation of the velocity threshold and the propagation of the avalanche at the free surface proceeds at the same rate for thresholds between 1 and 20 mm/s. Panels A and B of **Figure 45** show the time after the initiation of an avalanche, i.e. the elapsed time between the beginning of the avalanche until a specific location of the free surface exceeds v_t. Panel C of **Figure 45** shows the initiation points of each avalanche for a series of avalanches i.e. the first location to exceed v_t. Data are shown from three avalanches for a drum diameter of 140 mm, a particle size range of diameter 1.0 - 1.3 mm and fill level of 25 %.

Both Pohlman *et al.* [92] and Rabaud *et al.* [93] showed that close to the sides of the cylinder the endcaps effect the surface velocity. Therefore, a subregion in the center of the cylinder with a width of 300 mm is examined in the PIV experiments such that a representative behavior of the avalanching dynamics unaffected by the endcaps is presented.

We observe that an avalanche can be initiated at a variety of locations on the free surface, as was also observed experimentally by Balmforth and McElwaine [91]. It can be seen in **Figure 45** panel C that avalanches are initiated at random locations in the axial direction but concentrated in the 3rd quarter of the chord from the bottom. The lowest observed point of initiation is at 0.43 of the chord length from the bottom, the maximum is at 0.84 of the chord length from the bottom, and the mean is at 0.64 with a standard deviation of ±0.13 of the chord length from the bottom of the free surface.

The fraction of the surface in motion increases linearly for roughly 10 % of the duration of the avalanche and then the propagation slows down. On average 90 % of the free surface exceeds v_t within 257 ms ± 98 ms of the start of the avalanche. The average duration of the avalanche is 1.5 seconds, thus roughly the first 1/5 of the

avalanche duration is needed to put the almost entire bed surface in motion. These observations are confirmed in **Figure 46**, which shows the fraction of the free surface that is in motion as a function of time. The fraction of the fee

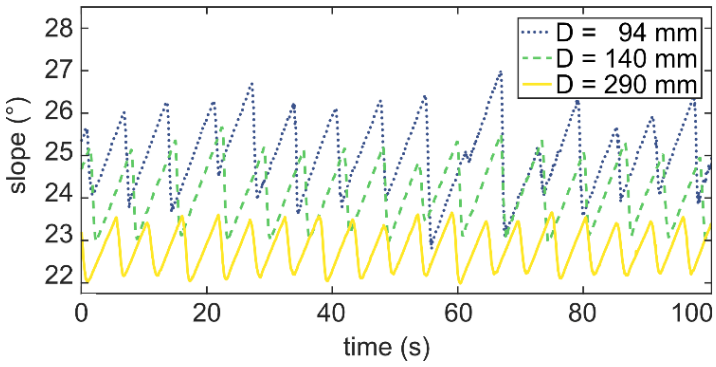

Figure 44 The slope of the free surface as a function of time for three drum diameters: 94 mm (dotted blue), 140 mm (dashed red) and 290 mm (yellow) rotating at 0.066 rpm and a fill level of 25 %. The particles are ballotini with a diameter of 1.0 - 1.3 mm.

Figure 47 shows velocities of the avalanching material at the start of an avalanche, during an avalanche, and at the end of an avalanche. Data are shown for an avalanche with a drum diameter of 140 mm, a particle size range of diameter 1.0 - 1.3 mm and fill level of 25 %. At the start of the avalanche the first movers begin their trajectory down the slope while the other particles do not show any relative motion. The maximal speed averaged across the bed surface (24 mm/s) was attained 0.59 seconds after the start of the avalanche (around 44 % of the duration of the avalanche). At this point the entire bed is in motion and appears to move uniformly down the slope as shown in the middle panel of **Figure 47**. In contrast to the beginning of the avalanche, where the trigger of the avalanche could be traced to an individual starting point, the end of the avalanche has a slow random relaxation of particle displacements to an equilibrium as observed by Zaitsev *et al.* and De Boeuf *et al.* [133, 143].

The high temporal and spatial resolutions of the PIV measurements reported here allow to estimate the trajectories of particles during an avalanche by integrating the PIV data. Note that PIV calculates the displacement of patterns, rather than of individual particles, with the result that the trajectories obtained in this manner do not represent the exact paths of individual particles. Here the term “pseudo particle” will be used to denote a pattern whose trajectory has been calculated by integrating PIV data.

Figure 48 shows the distances moved by pseudo particles during an avalanche as a function of the starting position of the pseudo particle. Data are shown for an avalanche in a drum of diameter 140 mm and fill level of 25 %. The particles are glass ballotini with a diameter of 1.0 - 1.3 mm.

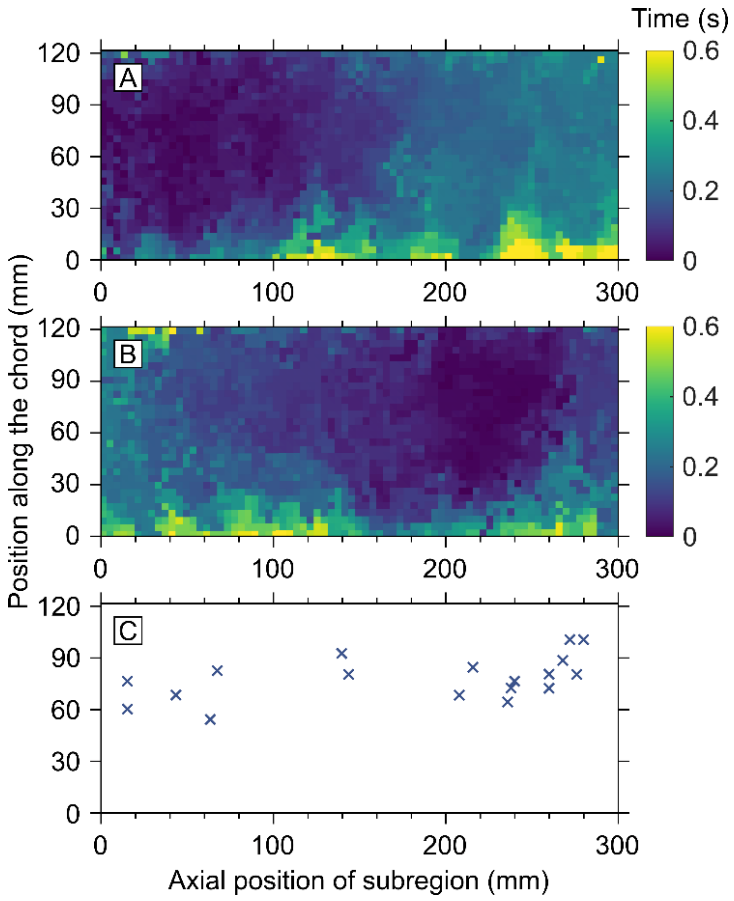

Figure 45 Local avalanche initiation time shown for two independent avalanche events (A and B) and a plot of the location of the avalanche initiation (C). In A and B the color indicates the time after the start of the avalanche for which the velocity at a point on the free surface exceeds 3 mm/s. In C the "×" indicates the location of the avalanche initiation for 18 avalanches. The cylinder has an internal diameter of 140 mm and rotates at 0.066 rpm. The fill level is 25 % and the particles are glass ballotini with a diameter 1.0 - 1.3 mm.

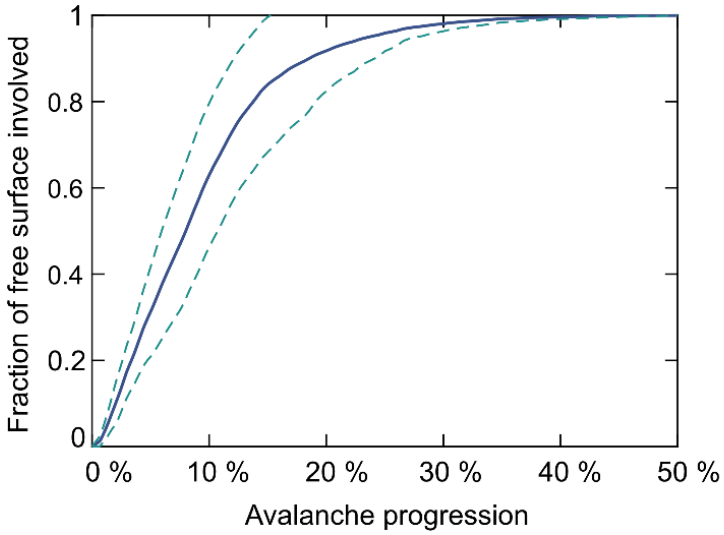

Figure 46 The fraction of the bed surface involved in an avalanching event as a function of the fraction of the duration of an avalanche event. The mean and standard deviation were calculated from the data of 20 avalanches. The cylinder has a diameter of 140 mm and rotates at 0.066 rpm. The fill level is 25 % and the particles are glass ballotini have a diameter of 1.0 - 1.3 mm.

Distances travelled for particles located in the lowest 10 % of the chord are not shown as they could have been overtaken by particles starting higher on the surface of the bed. The top 5 % is not shown to avoid the effect of visual distortion from the Plexiglas walls. PIV is only able to track the velocities of particles that remain on the surface. Thus, when a pseudo particle is overtaken by material flowing over, it is no longer trackable. Any subsequent velocity for this pseudo particle would correspond to the pseudo particle that had overtaken it. To avoid using the velocities of a particle that has overtaken the original particle, a control was set in place. The initial positions of pseudo particles were separated by the size of a PIV interrogation window to the pseudo particle below. In this work a pseudo particle was assumed to have been overtaken if a particle that started higher on the surface of the bed approached to a distance of less than half an interrogation window. It was found that only pseudo particles in the lowest 10 % of the chord could be overtaken.

Figure 49 shows the average distances travelled by particles down the free surface during an avalanche for a series of 16 avalanches. As with **Figure 48**, the distance travelled for particles starting in the lowest 10 % of the chord are not shown.

Figure 49 plots the average distances traveled by pseudo particles down the free surface during an avalanche (average of 16 avalanche events) for three different drum diameters. As in **Figure 48** the distance traveled by particles starting in the top 5 % and the lowest 10 % of the chord are not shown. **Figure 50** and **Figure 51** show respectively the average distances traveled by pseudo particles down the free surface during an avalanche (average of 16 avalanche events) for particle diameter and fill level. **Figure 52** shows the mean fraction of the chord length traveled by pseudo particles for the entire bed surface.

The particles located in the center of the bed surface travel the furthest distance, i.e., on average 20 % of the chord length for the largest drum diameter (290 mm) whereby the distance traveled decreases with decreasing drum diameter. This is expected as the Froude number decreases with decreasing drum diameter [13] .

The farther the particle from the center, the distance travelled by the particle decreases at an increasing rate. Due to the low Froude number, particles here travel less than 1/3 of the chord length as hypothesized in the model of Lim et al. [13] Above 85 % of the chord length from the bottom, there is a dramatic decrease in the distance travelled, with the top 5 % of the bed surface only travelling half as far, i.e. 10 % of the chord length.

As shown in **Figure 53**, the maxima of the mean speed averaged over the entire surface as well as the average distance travelled increase with growing drum diameters. Similar to **Figure 48**, the distance travelled for particles starting in the lowest 10 % of the chord were again not taken into account. When increasing the Froude number by increasing the rotational speed Daerr *et al.* [33] observed an increase in flow speed, which is in accordance with our findings.

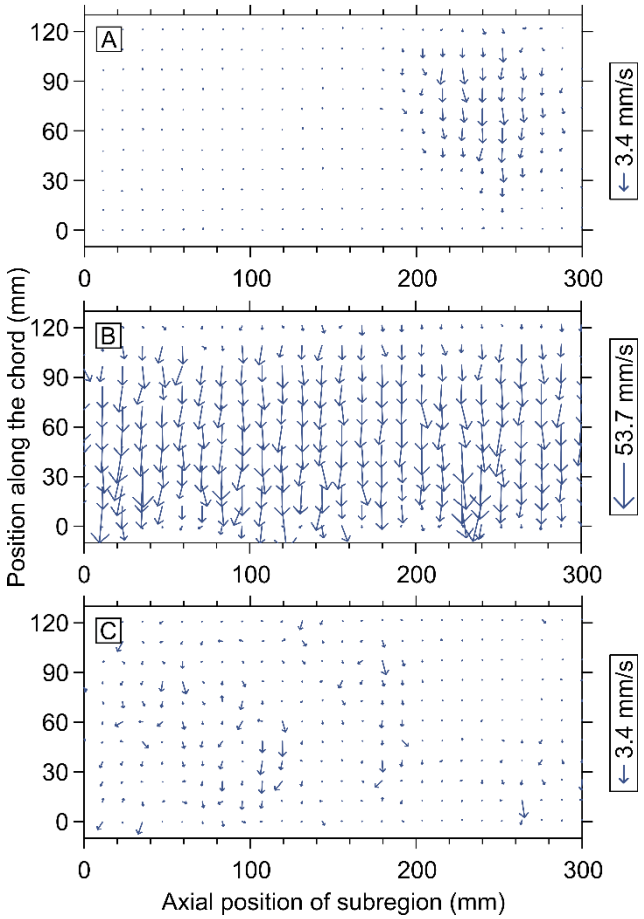

Figure 47 Velocity of particles at the bed surface during an avalanching event: (a) at the start, (b) at the maximal speed and (c) at the end of an avalanche, based on PIV calculations. The beginning of an avalanche is defined as the point in time when the first particles exceeded a velocity of 3 mm/s. The maximal speed attained by the avalanching material in the avalanche shown was 54 mm/s. The end of the avalanche was defined as the point when the speed of all pseudo particles was below 3 mm/s. The cylinder has an internal diameter of 140 mm and rotates at 0.066 rpm. The fill level is approximately 25 % and the particles are glass ballotini with a particle size range 1.0 - 1.3 mm.

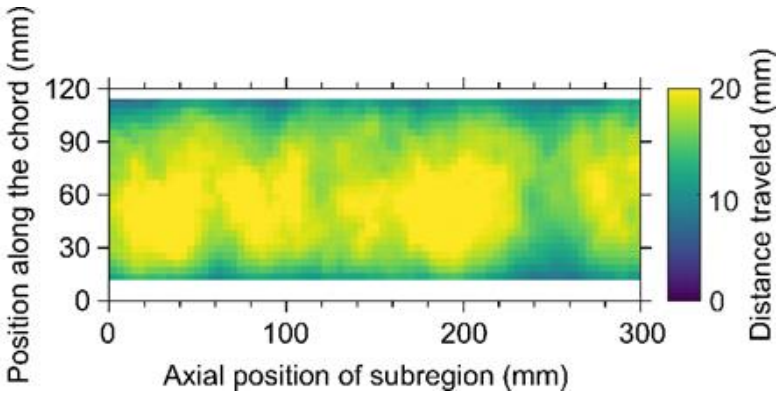

Figure 48 Distance traveled by pseudo particles as a function of the starting position along the chord for an inner drum diameter of 140 mm. The particles used were ballotini with a diameter of 1.0 - 1.3 mm. The drum rotated at 0.066 rpm and was filled to a fill level of 25 %. The top 5% and bottom 10 % of the free surface have been removed to avoid respectively, the possible effect of visual distortion due to the plexiglass walls at the top of the free surface and particles being overtaken at the bottom of the free surface.

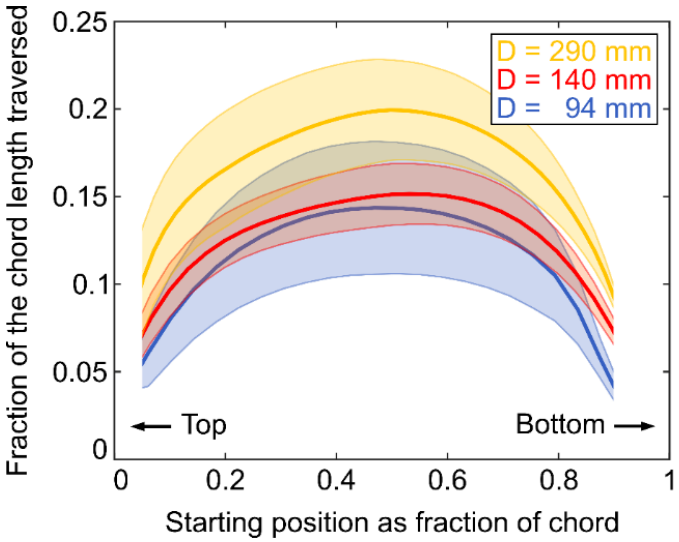

Figure 49 Mean fraction of the chord length traveled as a function of the starting position along the chord for varying drum diameters. The data has been averaged over 16 avalanches for each drum diameter. The cylinder has a diameter of either 94 mm (blue line), 140 mm (red line) or 290 mm (yellow line.) The correspondingly color-shaded areas represent one standard deviation The fill level is 25 % and the particles are glass ballotini with a diameter of 1.0 – 1.3 mm. The drum rotates at 0.066 rpm.

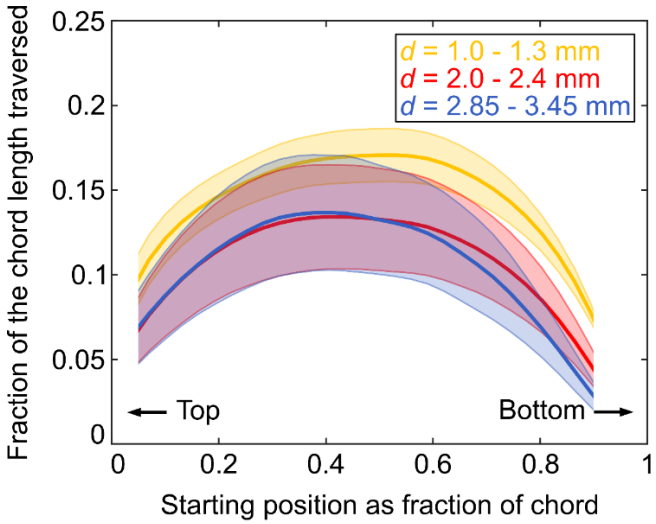

Figure 50 Mean fraction of the chord length traveled as a function of the starting position along the chord for varying particle diameters. The data has been averaged over 16 avalanches for each particle diameter. The particles have a diameter of either 1.0-1.3 mm (yellow line), 2.0-2.4 mm (red line) or 2.85-3.45 mm (blue line.) The correspondingly colored shaded areas represent one standard deviation. The fill level is 25 % and the drum diameter is 140 mm. The rotation speed is 0.066 rpm.

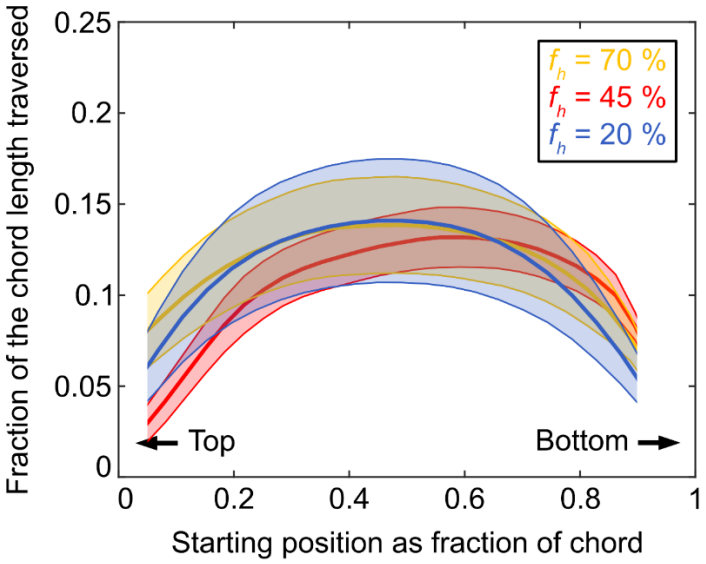

Figure 51 Mean fraction of the chord length traveled as a function of the starting position along the chord for varying fill levels. The data has been averaged over 16 avalanches for each drum diameter. The drum has a fill level of either 20 % (blue line), 45% (red line) or 70 % (yellow line.) The correspondingly color-shaded areas represent one standard deviation. The particles are glass ballotini with a diameter of 1.0 - 1.3 mm and the drum rotates at 0.066 rpm.

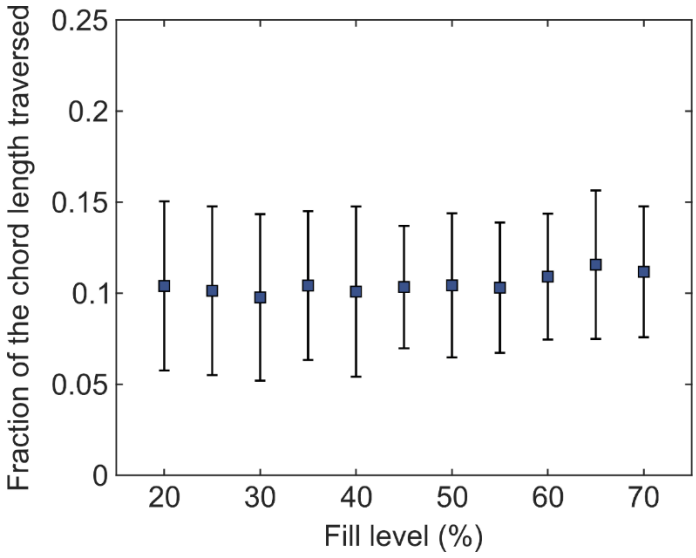

Figure 52 Mean fraction of the chord length traveled by pseudo particles for the entire bed surface during an avalanching event with their respective standard deviations as a function of the fill level of the drum. The drum is rotated at 0.066 rpm. The particles used were ballotini with a diameter 1.0 - 1.3 mm and the drum has an inner diameter of 94 mm.

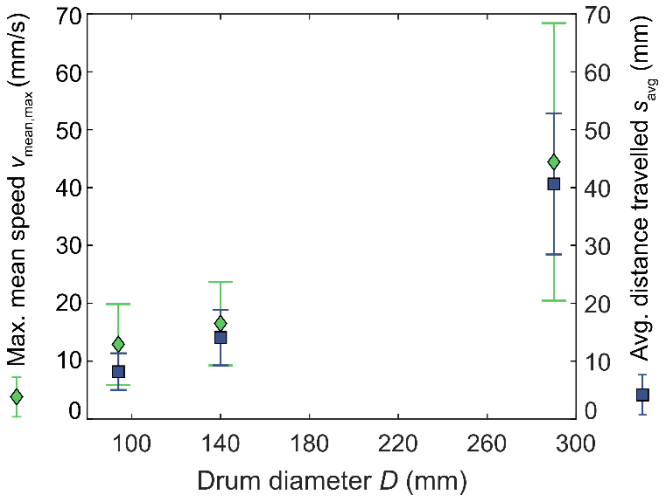

Figure 53 Maxima of the mean speed of the entire bed surface (green) and the average distance travelled (blue) averaged over the entire surface with their respective standard deviations as a function of the drum diameter. The drums rotated at 0.066 rpm. The particles used were ballotini with a diameter 1.0 - 1.3 mm and a fill level of 25 %. The lowest 10 % of the chord was not accounted for to calculate the distance travelled, as particles located in this part of the chord may have been overtaken by particle initially located higher up the chord.

8.5 Discussion

The distance travelled by pseudo particles along the free surface of the bed depends on their starting location. As seen in **Figure 49**, the particles that start in the center of the chord of the free surface travel the farthest and the farther the particle are from the center, the distance travelled by the particle decreases at an increasing rate. This behavior can be understood based on the work by Daerr *et al.* [28], which showed that the movement of particles in an avalanche is driven by two effects: the loss of support as the lower particles slide away and an increase in pressure due to the downward motion of particles that were initially located higher up. At the highest point of the free surface the pressure due to the weight of the particles above is minimal, while at the lowest point of the free surface the motion of particles is hindered by the cylinder wall. On the other hand, at the center of the free surface both effects occur, leading in turn to high avalanche velocities (**Figure 47** (b)).

Metcalfe *et al.* [12] proposed a geometric model for avalanches in which it was assumed that an avalanche transports a “wedge” of material from the upper half of the free surface to the lower half of the free surface as shown in **Figure 43**. In this model the lower half of the free surface is not involved in the avalanche and is simply covered by material flowing from the upper half of the free surface. The data presented here is not consistent with this simple geometric model. **Figure 45** and **Figure 47** clearly demonstrate that avalanches are being initiated in the center of the free surface (**Figure 45**). The avalanche is then propagated through the surface of the bed, setting its entire surface in motion (**Figure 47**), including the lower half of the bed.

Lim *et al.* [13] proposed a modified wedge model. The model of Lim *et al.* [13] assumes that the avalanching material moves an average distance of 1/3 of the chord down the free surface, rather than travelling the entire free surface in one avalanche. Their defined wedge is made up of two chords: the top surface of the bed before and after the avalanche. In accordance with Lim *et al.* [13], who suggested that the number of avalanches required for a particle to traverse the free surface to decrease linearly with increasing, w *Fr* e found the average distance travelled by particles in one avalanche to increase with increasing drum diameter.

Although it is possible to fit a linear relationship between the drum diameter and the average distance traveled (as would be expected according to the relationship proposed by Lim *et al.* [13]), a non-linear relationship is more likely, yet we do not have a sufficient number of experimental data to draw a robust conclusion.

In Lim *et al.*'s [13] model due to the shape of the wedge, which is shown schematically in **Figure 43**, most of the material which descends to the lower wedge is initially located at the top of the free surface. However, in our experiments we observe that particles located at the very top of the bed move significantly less during an avalanche than those in the center of the free surface. Therefore, although the data reported here suggest the model proposed by Lim *et al.* [13] is unlikely, we cannot disprove this model based on these data alone.

Instead, based on our experimental results, showing that particles located in the center of the chord moves the furthest (**Figure 49**) we propose a new geometric avalanche model. When creating a geometric model, a trade off between accuracy and simplicity has to be made. Hence, the new model has two objectives: (i) maintain a simple geometry, as has been done in the previous models of Metcalfe *et al.* [12] and Lim *et al.* [13], and (ii) improve the accuracy by taking into account the PIV results which show that the particles in the center of the free surface move the furthest. The proposed model is sketched in **Figure 55**. Here, the flowing (avalanching) layer is split into three equal "boxes" which deform into a wedge shape over an avalanching event. In the simulation, an avalanching event occurs when the surface has reached an angle of 25° and after the avalanche the free surface is at an angle of 23° (based on the experimental results from the drum of diameter of 140 mm shown in **Figure 44**). The particles in segments "A", "B", and "C" pre avalanche are randomly generated (mixed) in their respective sections after the preceding avalanching event. The deformation of the initial segments during an avalanching event is shown in **Figure 55** (note, the areas of each segment are preserved over an avalanche event).

This model reflects better the PIV results in that, on average particles in the middle segment travel farther than particles in the bottom segment and the same distance as particles in the top segment. Hence, although the middle section still does not move the farthest it is an improvement on both the Metcalfe *et al.* [12] and Lim *et al.* [13] models for which the top section travel the furthest down the free surface.

A schematic comparison of the distances traveled by particles located at the surface of the drum in the different models and the experiments is given in **Figure 54**. Due to the assumption of random mixing, in the simulations particles located higher up the chord in their respective sections have a higher potential to travel further when being re-generated after the avalanching event (**Figure 54**). Therefore, a shortcoming in our model lies in the particle dynamics in the area above the center of the chord. Yet as the particles in the top section (A) travel similar distances as the particles in the middle section, rather than larger distances as in the models Metcalfe *et al.* [12] and Lim *et al.* [13], our model is still an improvement to the existing ones.

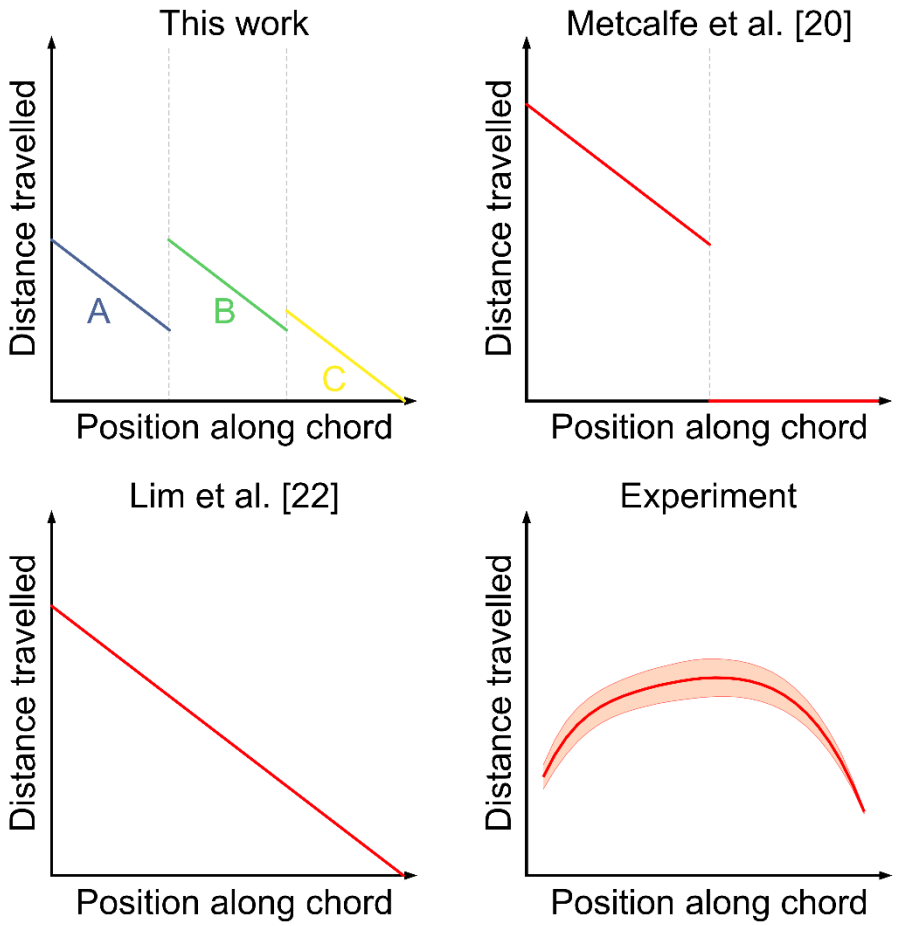

Figure 54 A schematic comparison of the distance traveled by particles located at the surface of the drum in the different models and the experiments.

The proposed model is sketched in **Figure 55**. Here, the flowing (avalanching) layer is split into three equal "boxes" which deform into a wedge shape over an avalanching event. This model reflects better the PIV results in that on average particles in the middle "box" travel farther than particles in the bottom "box" and the same distance as particles in the top "box." Hence, although the middle section still does not move the farthest it is an improvement on both the Metcalfe *et al.* [20] and Lim *et al.* models for which the top section travel the furthest down the free surface.

In order to compare the accuracy and visualize the difference of these three models, we recorded the mixing of an initially segregated bed from the lateral face of the cylinder.

Visualizing the particle mixing behavior through the end plates (see **Figure 56**) is a conventional approach for evaluating the mixing of the bed [12] and although the particle velocity is affected by the endcap walls, it provides useful information for the elaboration and validation of avalanching models.

For all models, we assumed random mixing within the segment of the free surface, although Lim *et al.* [13] do not state explicitly this assumption. (Metcalfe *et al*. [12] state explicitly that random mixing in a segment is assumed). First, we attempted to compare the predictions of the different models with the experimental data by computing a global parameter, i.e. the center of mass of the pink particles. **Figure 54** compares the position of

the center of mass of the pink particles (fill level 80 %, drum diameter 200 mm, particle size range 1.0-1.3 mm) predicted by the three models with the experimental measurements. In the beginning the models and the experimental data show very good agreement, while towards longer rotation times, larger differences between the individual models and the experimental data become apparent. Towards the end of the mixing experiments, it appears as the new model proposed here is closest to the experimental data, yet a clear assessment is difficult.

In a second step, we used key transition points for comparison between the models and the experimental results. The first key point is after the first avalanche. A side view of the bed after the first avalanche in the simulations and experiment is provided in **Figure 56** (a,b). In the experiment we observe a pink wedge, tapered to the outside of the cylinder, after the first avalanche. In the Metcalfe *et al.* [12] model a wedge has been formed but it tapers in towards the center of the cylinder, which does not agree with the experimental observations. The wedge predicted by the model of Lim *et al.* [13] also tapers in the opposite direction (up to the highest point of the free surface) to what is observed experimentally. Owing to the particular construction of the wedges in the Lim *et al.* [13] model and with the assumption of random mixing, some black particles are predicted in the upper half of the free surface after the first avalanche. As a matter of fact, Lim *et al.* [13] do not describe how mixing occurs in the wedge and it is only mentioned that particles move on average 1/3 of the length of the chord. On the one hand, if random mixing is taking place inside the wedges and its centroid moves 1/3 of the chord length, as considered in **Figure 56**, an unrealistic behavior of the black particles would take place. On the other hand, if all particles on the surface of the bed move on average 1/3 of the chord length, the whole wedge would slide down, thus not making possible to have the wedge tapering towards the top they predict.

The new model proposed here overcomes the abovementioned limitations of both Metcalfe *et al.* [12] and Lim *et al.* [13] models and predicts a physically realistic formation of a wedge of pink particles that is tapering in the same direction as the experiments, i.e. towards the lower edge of the free surface.

Another further key transition moment is when black particles start to avalanche down over the pink particles. This point in the rotation cycle allows for another comparison between the three models and experiments (**Figure 56** (c,d)). A red line along the perimeter of the cylinder of equal length allows for an easier comparison between the experiments and the different models. In the models of Lim *et al.* [13] and Metcalfe *et al.* [12], the black beads close to the perimeter have travelled farther down compared to the newly proposed model and the experiments. A further region that allows for a quantitative comparison is the size of the core, i.e. the unmixed center part of the cylinder that exists for fill levels greater than 50 % [12]. The distance from the top of the free surface to the unmixed core, h_c, is marked in **Figure 56** (d) and is used for comparison. We observe that h_c as determined in the experiments is larger than the value predicted in any of the models. Nonetheless, the model proposed in this work gives values of h_c that are the closest to the experimental value. **Table 9** (h_c for 60 % and 80 % fill levels) confirms quantitatively the improved accuracy of the newly proposed model, albeit there still exist some appreciable differences to the experimental results.

Although we have not examined the depth of the surface flow, we can compare the depth of the surface flow in our model with the experimental data of Rabaud *et al.* [93] who examined from the side walls the depth of the surface flow due to avalanches using PIV (drum diameters 17–50 cm, fill level 50 %). It was found that the particle velocity decays exponentially with depth from the surface. If we consider the depth at which the particle velocity has dropped to 25 % of its value at the surface as the thickness of the avalanching layer, the experiments of Rabaud *et al.* [93] yield a thickness of the flowing layer of ~ 3.0 mm (bed particles of size 1.0 mm). This agrees very well with the depth of the segments used in our model.

Table 9 Distance from the surface of bed to the unmixed core of the bed (h_c). The unmixed core is the part of the bed that is not involved during an avalanche and which therefore remains unchanged throughout all rotations

	h_c 60 % fill [mm]	h_c 80 % fill [mm]
Experiment	10.1 ± 2.0	6.6 ± 1.3
New Model	4.0 ± 0.3	2.5 ± 0.5
Lim et al.	0.9 ± 0.5	1.3 ± 0.4
Metcalfe *et al.*	0.1 ± 0.2	0.2 ± 0.3

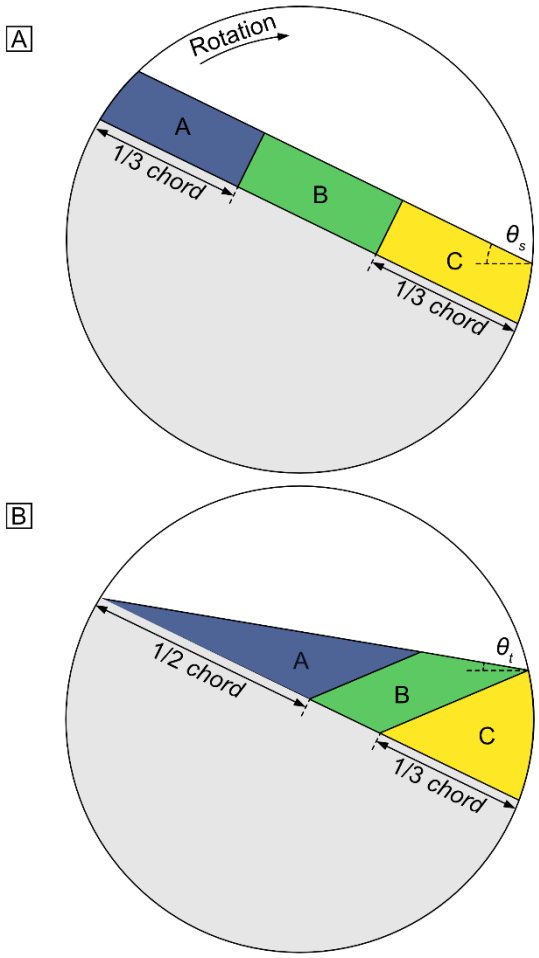

Figure 55 The new geometric avalanche model proposed here based on the experimental PIV data aquired. The flowing layer of the bed is separated into sections A, B and C: (a) The flowing (avanlanching) layer before the avalanching event is initiated; (b) Deformation of the initial segments during the avalanching event considering that particles located in the center of the bed move the farthest during an avalanching event.

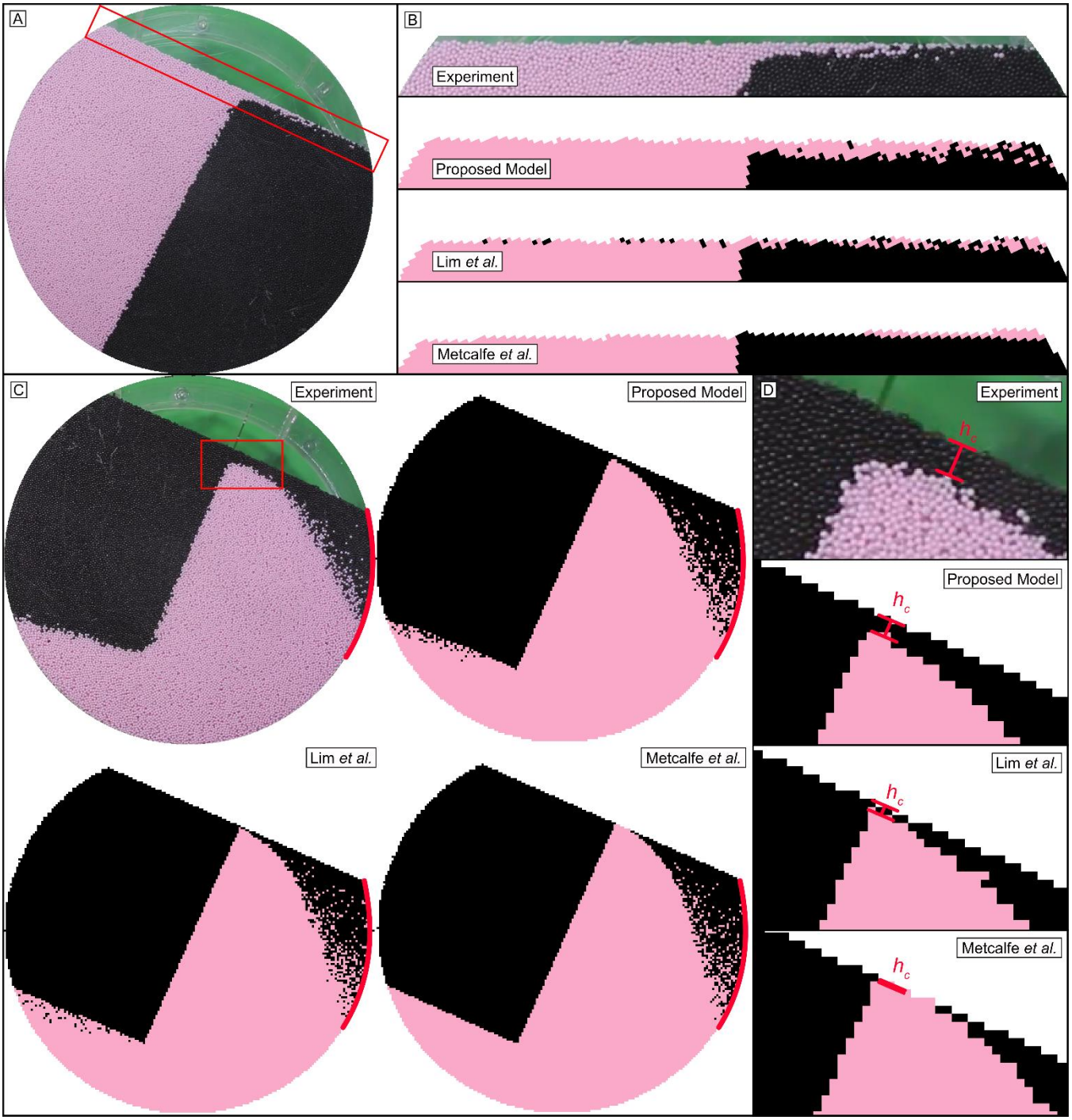

Figure 56 Comparison between the predictions of the models of Metcalfe *et al.* [12] and Lim *et al.* [13], the newly proposed model and experimental data. The fill level is 80 % and the diameter of the cylinder is 200 mm. The particles used in the experiments are 1-1.3 mm in diameter. The red rectangle (a) show the area that has been zoomed into in (b). The snapshot in (a) gives a side of the entire bed after one avalanche. The snapshots in (b) zoom into the top 20 mm of the experimental bed and the predictions of the models of Metcalfe *et al.* [12] and Lim *et al.* [13] and the newly poposed model. (c) Snapshots of the beds after a rotation by 204°. A red line spanning 59° is added to aid a visual comparison between the predictions of the model and the experimental data; (d) zoom into a region spanning from the top surface to the start of the unmixed core of the bed.

8.6 Conclusion

PIV has been performed to examine the movement of particles along the free surface of an avalanche in a rotating cylinder. The angle of repose of the bed was also tracked.

A “sawtooth” pattern can be seen for the slope of the bed as a function of time. The individual avalanches can be observed by a rapid decrease in the slope angle, with each avalanche followed by a linear increase in slope angle during rigid body rotation. As the diameter of the cylinder, and hence the Froude number, is increased, the avalanches become more regular, as also observed by Daerr *et al.* [33].

Avalanches appear to begin from an initiation point anywhere axially on the free surface though radially the initiation is concentrated in the third quarter from the bottom. Avalanches appear to begin from an initiation point anywhere on the free surface and propagate quickly such that more than 90 % of the bed is in motion by about 20 % of the duration of an average avalanche from its start. At the point when the maximum speed in an avalanche was attained, the entire bed is uni-directionally travelling down the chord. The particles still in movement at the end of an avalanche appear to be randomly scattered on the free surface with multi-directional velocities similar to the results of Zaitsev *et al.* and De Boeuf *et al.* [133, 143]. The distances travelled along the free surface of the particle bed are a function of their starting location along the chord of the free surface. The particles that travel the farthest are located at the center of the free surface. Farther from the center, the distance travelled by the particles decreased at an increasing rate. Based upon these results an updated geometric model was proposed, where the flowing surface is divided into three sections which deform into a wedge during an avalanching event. The newly proposed model shows a better agreement with experimental mixing data when compared to the models of Metcalfe *et al.* [12] and Lim *et al.* [13], albeit the improvement is only visible in a few specific locations.

9 Conclusions and Outlook

9.1 Conclusions

This dissertation has explored intriguing phenomena in dynamic granular media. Specifically, the following dynamic granular systems have been studied: 1) the motion of granular droplets and bubbles in beds which are agitated by both vibration and gas fluidization and 2) particle mixing in a rotating cylinder.

The investigation of granular beds that are agitated by both vibration and gas fluidization revealed Rayleigh-Taylor (R-T) like instabilities. When particles of different density were agitated in quasi 2D beds, the lighter grains rose through the bed of heavier grains in the form of "fingers" and "bubbles." Indeed, when initializing in such bed a granular bubble that is made up of less dense particles within a bed of denser particles, the lighter particles rise together as an entity akin to a gas bubble, even in the absence of surface tension in such a system. When the bed was initialized such that the bottom half was filled with less dense particles and the top half with denser particles, the lighter particles rose in the form of fingers (similar to the classic Rayleigh-Taylor instability) until they pinch off and continue to rise to the top of the bed in the form of bubbles. The process continues until the composition of the bed has reversed, i.e. the layer of lighter particles are on top of the layer of heavier particles. It was shown that the size and growth rate of the fingers increases with increasing gas flow rate, vibration strength and particle size and experiments with only gas flow or only vibration were unable to produce the phenomenon.

In the classic R-T instability in liquids, buoyancy is the driving force for inversion and surface tension stabilizes the interface, leading to the formation of fingers of a characteristic wavelength. The R-T instability in granular materials is surprising because the grains are suspended by gas flow and have no significant cohesive forces to create surface tension. We explained the R-T-like phenomenon in granular media as follows: Buoyancy drives the inversion, since the two particle-gas mixtures have different bulk densities and due to interparticle friction the particle-phase has a granular viscosity. The high effective viscosity of the grains stabilizes the interface, leading to perturbations of a characteristic wavelength rather than an immediate homogeneous inversion Thus, the key dimensionless number for describing the initial shape and rate of growth of perturbations is the ratio of viscous to buoyant forces. The ratio of the gas flow rate to the minimum fluidization velocity (U/U_{mf}) was also found to be key in the formation of these perturbations because gas flow is needed to suspend the particles, enabling them to act like a viscous fluid. Vibration strength is the other important dimensionless group for characterizing this phenomenon because vibration lowered the gas velocity at which the particles become suspended, allowing fingers to form without the presence of gas bubbles. U/U_{mf} and the normalized vibration strength Γ were shown to collapse data for the fingering regime map across different particle sizes and vibration conditions and are thus believed to describe well the initial perturbation stage.

Since vibration was found to be key to the R-T instabilities its effects on the minimum fluidization and bubbling velocity were further examined. Experiments in vibrated, gas-solid fluidized beds showed that vibration decreases U_{mf} and U_{mb} in Geldart Group B and D particles for vibration strengths less than 1. U_{mf} decreased more than U_{mb} with vibration, which created a densely packed, homogeneous fluidization state where $U_{mf} < U < U_{mb}$. Particle density was not found to affect the decrease of U_{mf} or U_{mb} with vibration. Particle size on the other hand, had a significant and non-monotonic effect on the extent of this reduction. Importantly, the decrease of U_{mf} and U_{mb} due to vibration was seen in both 3D cylindrical and pseudo-2D fluidized beds. A dimensional analysis taking vibration into account led to a power law that describes accurately the effect of vibration on U_{mf}.

We also observed the phenomenon of a splitting granular droplet, i.e. when a granular droplet composed of denser particles was placed near the top of a bed of lighter particles, it did not simply sink vertically as it does in the case of liquids of different densities, but rather splits into two daughter droplets which sink on an inclined path until they themselves split further and the process repeats itself. The mechanism behind this splitting was explored in detail both experimentally and numerically. In such experiments, a granular droplet was inserted

into a bed composed of bulk particles with a larger diameter and lower density. Simultaneously vertical vibrations and a fluidizing gas flow were applied to the bed (vibro-gas-fluidized bed). The experiments showed that a granular droplet does not simply sink vertically but instead begins its movement preferentially laterally. This causes a spreading and thinning of the granular droplet and ultimately the droplet splits into two daughter droplets. The daughter droplets themselves sink further and may undergo subsequent splitting events. Although visually similar to the Rayleigh-Taylor-induced fragmentation of liquid droplets falling in a miscible liquid of lower density, the mechanism causing the splitting of a granular droplet was shown to be different. Numerical simulations reproduced this splitting phenomenon and demonstrated that the higher density of the particles forming the granular droplet (compared to the density of the surrounding bulk particles) produces an immobilized zone underneath the granular droplet. The immobilized zone blocks the direct downwards motion of the droplet and forces the droplet to spread laterally, leading to the formation of daughter droplets. These daughter droplets are initially connected and move at an angle, maintaining the immobilized zone underneath the elongated droplet, and thus they descend on inclined trajectories around this zone. When the connecting band between the two forming daughter droplets is thin enough, the pressure from the connecting band is insufficient to sustain further an immobilized zone. The disappearance of the immobilized zone starts the binary split of each daughter droplet.

Turning to the motion of particles in a rotating cylinder, particle image velocimetry (PIV) was applied onto the bed surface to image the avalanching regime while the bed of particles was also filmed from the side in order to determine the angle of the free surface of the bed. A “sawtooth” pattern was seen for the slope of the bed as a function of time with individual avalanches leading to a rapid decrease in the slope angle, followed by a linear increase of the slope angle during rigid body rotation. As the diameter of the cylinder increases (i.e. increasing Froude number), the avalanches became more regular. PIV on the bed surface showed that avalanches can initiate anywhere axially on the free surface though radially the initiation is concentrated in the third quarter from the bottom. Upon initiation, the avalanches propagated quickly with more than 90 % of the bed in motion after only 20 % of the duration of an average avalanche has occurred. When the maximum speed in an avalanche was attained, the entire bed is uni-directionally travelling down the chord. The distances travelled by particles along the free surface of the bed during an avalanche were found to be a function of their starting location along the chord of the free surface. Particles in the center travel the furthest and the further the particle from the center the less distance it traveled. These experiment results were subsequently used to propose a novel geometric avalanching model, dividing the flowing surface into three sections which deform into a wedge during an avalanching event. Mixing experiments filmed from the end plates showed that the newly proposed model predicts the experimentally observed mixing pattern more accurately when compared to the models of Metcalfe *et al.* [12] and Lim *et al.* [13].

9.2 Outlook

The research presented here has further advanced our knowledge of granular materials. However, there remains much more to discover on the subject of granular materials. The presented work has described the physics driving the splitting of a granular droplet in a vibro-gas-fluidized bed. However, a key question remains to be resolved: As a binary granular material does not possess any surface tension, why do the denser particles remain aggregated rather than percolating through the bed as individual particles? Royer et al. [80] have shown attractive forces such as van der Waals interactions and capillary bridges in granular materials to lead to the clustering of particles in free-falling streams of granular matter resembling the surface-tension-driven Plateau–Rayleigh instability. However, neither of these attractive forces have been implemented in the numerical simulations reported in this work and yet the granular material still remains aggregated. Thus, these forces cannot explain the aggregation in binary granular material. It could be that size effects and a difference in inter-particle momentum transfer could contribute to this aggregation behavior. The fundamental mechanism behind this aggregation still demands further investigation. Further combinations of numerical simulations and experiments could elucidate which forces play a key role in this aggregation behaviour.

All Rayleigh-Taylor experiments have been performed in quasi 2-D beds. It would be of interest to see if the same instabilities occur also in 3-D systems. Due to the opaque nature of granular matter, it is difficult to test this experimentally. There exist tomographic techniques, which allow for non-intrusive measurements in opaque systems but unfortunately these techniques cannot currently be performed on vibro-fluidized beds. One method for probing opaque systems is real time MRI imaging. When using real-time MRI there are certain restrictions. Due to the high magnetic fields no ferromagnetic materials can be close to the MRI. This makes it difficult to perform vibration experiments as conventional shakers contain to a large extent of ferromagnetic materials. Hence, it would be required to construct a vibrating set-up, e.g. through an eccentric vibrating system constructed. out of PMMA or aluminium with the motor far away from the MRI magnet. The second difficulty of real-time MRI imaging is that the MRI developed in collaboration with Prof. Prüssmann is limited to the detection of proton-containing materials, requiring the availability of MRI sensitive particles. We have developed such materials, but their large-scale manufacturing is still a challenge that has to be overcome [94]. Also, the range of diameters and in particular densities is rather limited. Hence, numerical simulations will be very likely more informative in such 3-D systems, yet full 3D systems are computationally very expensive due to the large number of particles they contain. We have performed some preliminary simulations of 3-D systems. In the simulated 3-D bed the droplet sank down vertically in a straight trajectory. This behaviour is very similar to the numerical simulation of a granular droplet in a quasi 2-D bed without interparticle friction. Based upon the result of this one simulation, it could be hypothesized that in 2-D beds due to the presence of the front and rear walls, a larger immobilized zone below the droplet is generated, forcing the droplet to spread laterally. In the 3-D case, i.e. in the absence of wall effects (or present to a lesser extent), the immobilized zone is too small, leading in turn to a vertical motion. Nonetheless, this is only a speculation, and further numerical (and potentially experimental) work is required to prove or disprove this hypothesis.

PIV imaging was performed on the surface of a bed of particles in a rotating drum to characterize avalanching, both resolved in time and spatially across the surface. Particle trajectories were calculated to estimate mean distances travelled down the slope. Based upon the experimental results, a new mixing model was developed. However, for this mixing model only the surface movement was considered. Therefore, it would be of interest to perform further PIV imaging experiments through the end plates of the cylinder in order to probe how the particles flow below the surface. Unfortunately, these measurements will be affected to some extent by wall effects and may not represent well what occurs beneath the surface further down the bed. Nonetheless, such measurements would be highly complementary and will improve further our understand of the avalanching regime and the mixing in rotating drums.

10 Bibliography

[1] H. M. Jaeger and S. R. Nagel, "Physics of the Granular State," *Science,* vol. 255:5051, no. Physics of the Granular State, pp. 1523-1531, March 1992.

[2] J. M. Ottino and D. V. Khakhar, "Mixing and Segregation of Granular Materials," *Annu Rev Fluid Mech,* vol. 32, p. 55–91, 2000.

[3] P. V. Danckwerts, "Continuous flow systems: distribution of residence times," *Chemical Engineering Science,* vol. 2.1, pp. 1-13, 1953.

[4] A. A. Aissa, C. Duchesne and D. Rodrigue, "Polymer Powders Mixing Part I: Mixing Characterization in Rotating Cylinders," *Chem. Eng. Sci,* vol. 65, p. 786, 2010.

[5] J. Raasch, *Notes for the course of lectures on "Mischen und Rühren" [Mixing and Stirring],* University of Karlsruhe (Technical College), Summer semester 86.

[6] P. M. C. Lacey, "Developments in the theory of particle mixing.," *Journal of applied chemistry,* vol. 4, no. 5, pp. 257-268, 1954.

[7] R. Weinekötter and H. Gericke, Mixing of solids, vol. 12, Springer Science & Business Media, 2000.

[8] G. Seiden and P. J. Thomas, "Complexity, segregation, and pattern formation in rotating-drum flows," *Rev. Mod. Phys.,* vol. 83, pp. 1323-1365, 2011.

[9] V. Lubarda, "The shape of a liquid surface in a uniformly rotating cylinder in the presence of surface tension," *Acta Mech,* vol. 224, no. 7, p. 1365–1382, 2013.

[10] S. H. Chou, C. C. Liao and S. S. Hsiau, "An experimental study on the effect of liquid content and viscosity on particle segregation in a rotating drum," *Powder Technology,* vol. 201, no. 3, pp. 266-272, 2010.

[11] G. Seiden and P. J. Thomas, "Complexity, segregation, and pattern formation in rotating-drum flows," *Reviews of Modern Physics,* vol. 83, no. 4, p. 1323, 2011.

[12] G. Metcalfe, T. Shinbrot, J. J. McCarthy and J. M. Ottino, "Avalanche Mixing of Granular Solids," *Nature,* vol. 374, p. 6517, 1995.

[13] S. Y. Lim, J. F. Davidson, R. N. Forster, D. J. Parker, D. M. Scott and J. P. K. Seville, "Avalanching of Granular Material in a Horizontal Slowly Rotating Cylinder: PEPT Studies," *Powder Technol,* vol. 138, p. 25, 2003.

[14] D. Kunii and O. Levenspiel, Fluidization engineering., Butterworth-Heinemann, 1991.

[15] C. Y. Wen and Y. H. Yu, "A generalized method for predicting the minimum fluidization velocity," *AIChE Journal,* vol. 12, no. 3, pp. 610-612, 1966.

[16] D. Geldart, "Types of gas fluidization," *Powder Technol.,* vol. 7, pp. 285-292, 1973.

[17] G. I. Taylor, "The instability of liquid surfaces when accelerated in a direction perpendicular to their planes," *I. Proc R Soc Lond A,* vol. 201, p. 192–196, 1950.

[18] A. Burrows, "Supernova explosions in the Universe," *Nature,* vol. 403, p. 727–733, 2000.

[19] B. Gyüre and I. M. Jánosi, "Basics of lava-lamp convection," *Phys Rev E,* vol. 80, 2009.

[20] A. Lange, M. Schröter, M. A. Scherer, A. Engel and I. Rehberg, "Fingering instability in a water-sand mixture," *Eur Phys J B - Condens Matter Complex Syst,* vol. 4, p. 475–484, 1998.

[21] J. L. Vinningland, Ø. Johnsen, E. G. Flekkøy, R. Toussaint and K. J. Måløy, "Granular Rayleigh-Taylor Instability: Experiments and Simulations," *Phys Rev Lett,* vol. 99, 2007.

[22] G. Owen, "Load structures: gravity-driven sediment mobilization in the shallow subsurface," *Geol Soc Lond Spec Publ,* vol. 216, p. 21–34, 2003.

[23] R. C. A. Hindmarsh and K. F. Rijsdijk, "Use of a viscous model of till rheology to describe gravitational loading instabilities in glacial sediments," *Geol Soc Lond Spec Publ,* vol. 176, p. 191–201, 2000.

[24] C. J. N. Wilson, "The role of fluidization in the emplacement of pyroclastic claws: An experimental approach," *J Volcanol Geotherm Res,* vol. 8, p. 231–249, 1980.

[25] J. R. Grace, "The viscosity of fluidized beds," *Can J Chem Eng,* vol. 48, p. 30–33, 1970.

[26] N. Burtally, P. J. King and M. R. Swift, "Spontaneous Air-Driven Separation in Vertically Vibrated Fine Granular Mixtures," *Science,* vol. 295, p. 1877–1879, 2002.

[27] G. Owen, "Experimental soft-sediment deformation: structures formed by the liquefaction of unconsolidated sands and some ancient examples," *Sedimentology,* vol. 43, p. 279–293, 1996.

[28] J. J. Thomson and H. F. Newall, "On the formation of vortex rings by drops falling into liquids, and some allied phenomena," *Proc R Soc Lond,* vol. 39, p. 417–436, 1886.

[29] F. T. Arecchi, P. K. Buah-Bassuah, F. Francini, C. Pérez-Garcia and F. Quercioli, "An Experimental Investigation of the Break-up of a Liquid Drop Falling in a Miscible Fluid," *Europhys Lett EPL,* vol. 9, p. 333–338, 1989.

[30] J. Hester and A. Loll, "NASA Hubsite," [Online]. Available: https://hubblesite.org/resource-gallery. [Accessed 4 April 2022].

[31] G. Machu, W. Meile, L. C. Nitsche and U. Schaflinger, "Coalescence, torus formation and breakup of sedimenting drops: Experiments and computer simulations," *J. Fluid Mech.,* vol. 447, p. 299, 2001.

[32] R. A. Bagnold, "The movement of desert sand," *Proc R Soc Lond A,* vol. 157, p. 594–620, 1936.

[33] A. Daerr and S. Douady, "Two types of avalanche behaviour in granular media," *Nature,* vol. 399, p. 241–243, 1999.

[34] F. J. Muzzio, T. Shinbrot and B. J. Glasser, "Powder technology in the pharmaceutical industry: the need to catch up fast," *Powder Technology,* vol. 124, p. 1–7, 2002.

[35] J. C. Abanades, E. J. Anthony, D. Y. Lu, C. Salvador and D. Alvarez, "Capture of CO2 from combustion gases in a fluidized bed of CaO," *AIChE J,* vol. 50, p. 1614–1622, 2004.

[36] D. J. Goldfarb, B. J. Glasser and T. Shinbrot, "Shear instabilities in granular flows," *Nature,* vol. 415, p. 302–305, 2002.

[37] J. R. Royer, "High-speed tracking of rupture and clustering in freely falling granular streams," *Nature,* vol. 459, p. 1110–1113, 2009.

[38] J. Duran, "Rayleigh-Taylor Instabilities in Thin Films of Tapped Powder," *Phys Rev Lett,* vol. 87, 2001.

[39] N. Epstein and B. P. LeClair, "Liquid fluidization of binary particle mixtures—II. Bed inversion," *Chem Eng Sci,* vol. 40, p. 1517–1526, 1985.

[40] R. J. Nichols, R. S. J. Sparks and C. J. N. Wilson, "Experimental studies of the fluidization of layered sediments and the formation of fluid escape structures," *Sedimentology,* vol. 41, p. 233–253.

[41] R. Keane and R. Adrian, "Theory of cross-correlation analysis of PIV images," *Applied scientific research,* vol. 3, pp. 191-215, 1992.

[42] Y. Tsuji, T. Kawaguchi and T. Tanaka, "Discrete particle simulation of two-dimensional fluidized bed," *Powder Technol,* vol. 77, p. 79–87, 1993.

[43] T. Anderson and R. Jackson, "Fluid mechanical description of fluidized beds," *Ind Eng Chem Fundam 6,* vol. 4, pp. 527-539, 1967.

[44] C. Wen and Y. Yu, "A generalized method for predicting the minimum fluidization velocity," vol. 3, pp. 610-612.

[45] T. W. Pan, D. D. Joseph and R. Glowinski, "Modelling Rayleigh–Taylor instability of a sedimenting suspension of several thousand circular particles in a direct numerical simulation," *J Fluid Mech,* vol. 434, p. 23–37, 2001.

[46] J. KOZENY, "Uber Kapillare Leitung der Wasser in Boden," *R Acad Sci Vienna Proc Cl I,* vol. 136, p. 271–306, 1927.

[47] R. M. Davies and G. Taylor, *The Mechanics of Large Bubbles Rising through Extended Liquids and through Liquids in Tubes,* vol. 200, 1950, p. 375–390.

[48] C. Liu, L. Wang, P. Wu and M. Jia, "Effects of Gas Flow on Granular Size Separation," *Phys Rev Lett,* vol. 104, 2010.

[49] S. Residori, P. K. Buah-Bassuah and F. T. Arecchi, "Fragmentation instabilities of a drop as it falls in a miscible fluid," *Eur Phys J Spec Top,* vol. 146, p. 357–374, 2007.

[50] J. Westerweel, "Fundamentals of digital particle image velocimetry," *Meas Sci Technol,* vol. 8, 1997.

[51] D. Geldart, "Types of gas fluidization," *Powder Technol.,* vol. 7, pp. 285-292, 1973.

[52] C. Xu and J. Zhu, "Experimental and theoretical study on the agglomeration arising from fluidization of vohesive particles - effects of mechanical vibration," *Chem. Eng. Sci.,* vol. 60, pp. 6529-6541, 2005.

[53] Y. Mawatari, T. Koide, Y. Tatemoto, S. Uchida and K. Noda, "Effect of particle diameter on fluidization under vibration," *Powder Technol.,* vol. 123, pp. 69-74, 2002.

[54] R. Gupta and A. Mujumdar, "Aerodynamics of a vibrated fluid bed," *Can. J. Chem. Eng.,* vol. 58, pp. 332-338, 1980.

[55] Y. Mawatari, Y. Tatemoto and K. Noda, "Prediction of minimum fluidization velocity for vibrated fluidized bed," *Powder Technol.,* vol. 131, pp. 66-70, 2003.

[56] C. McLaren, T. Kovar, A. Penn, C. Müller and C. Boyce, "Gravitational instabilities in binary granular materials," *Proc. Natl. Acad. Sci.,* vol. 116, no. 19, pp. 9263-9268, 2019.

[57] R. Ojha, N. Menon and D. J. Durian., "Hysteresis and packing in gas-fluidized beds," *Physical Review E,* vol. 62.3, p. 4442, 2000.

[58] S. C. Tsinontides and R. Jackson, "The mechanics of gas fluidized beds with an interval of stable fluidization," *Journal of Fluid Mechanics,* vol. 255, pp. 237-274, 1993.

[59] M. H. Köhl, L. G. J. R. Third, K. P. Pruessmann and C. R. & Müller, "Magnetic resonance imaging (MRI) of jet height hysteresis in packed beds," *Chemical Engineering Science,* vol. 109, pp. 276-283., 204.

[60] Y. Wang, T.-J. Wang, Y. Yang and Y. Jin, "Resonance characteristics of a vibrated fluidized bed with a high bed hold-up," *Powder Technol.,* vol. 127, pp. 196-202, 2002.

[61] D. Barletta, P. Russo and M. Poletto, "Dynamic response of a vibrated fluidized bed of fine and cohesive powders," *Powder Technol.,* vol. 237, pp. 276-285, 2013.

[62] R. Roy, J. Davidson and V.G. Tuponogov, "The velocity of sound in fluidised beds," *Chemical Engineering Science,* vol. 45, p. 3233–3245, 1990.

[63] V. Rojo, J. Guardiola and A. Vian, "A capacitor model to interpret the electric behaviour of fluidized beds. Influience of apparatus geometry," *Chem. Eng. Sci.,* vol. 41, pp. 2171-2181, 1986.

[64] G. Ramos Caicedo, M. García Ruiz, J. Prieto Marqués and J. Guardiola Soler, "Minimum fluidization velocities for gas-solid 2D beds," *Chem. Eng. and Proc: Process Intensif.,* vol. 41, pp. 761-764, 2002.

[65] S. Sánchez-Delgado, J. Almendros-Ibáñez, N. García-Hernando and D. Santana, "On the minimum fluidization velocity in 2D fluidized beds," *Powder Technol.,* vol. 207, pp. 145-156, 2011.

[66] S. Ergun, "Fluid flow through packed columns," *Chem. Eng. Prog.,* vol. 48, p. 89, 1952.

[67] G. Meyrat, B. McArdell, K. Ivanova, C. Müller and P. Bartelt, "Lanslides (in press)," 2021.

[68] F. J. Jaeger, S. R. Nagel and R. P. Behringer, "Granular solids, liquids, and gases," *Rev. Mod. Phys,* vol. 68, p. 1259, 1996.

[69] K. Adachi, S. Kiriyama and N. Yoshioka, "Behavior of a swarm of particles moving in a viscous-fluid," *Chem. Eng. Sci.,* vol. 33, p. 115, 1978.

[70] C. P. McLaren, J. P. Metzger, C. M. Boyce and C. R. Müller, "Reduction in minimum fluidization velocity and minimum bubbling velocity in gas-solid fluidized beds due to vibration," *Powder Technol.,* vol. 382, p. 566, 2021.

[71] J. K. Sveen, "An introduction to matpiv v. 1.6.1," *Matematisk Institutt, Universitetet i Oslo,* 2012.

[72] C. Goniva, C. Kloss, N. G. Deen, J. A. M. Kuipers and S. Pirker, "Influence of rolling friction on single spout fluidized bed simulation," *Particuology,* vol. 10, p. 582, 2012.

[73] P. A. Cundall and O. D. L. Strack, "A discrete numerical model for granular assemblies," *Géotechnique,* vol. 29, p. 47, 1979.

[74] Y. Tsuji, T. Tanaka and T. Ishida, "Lagrangian numerical simulation of plug flow of cohesionless particles in a horizontal pipe," *Powder Technol.,* vol. 71, p. 239, 1992.

[75] S. R. Waitukaitis and H. M. Jaeger, "Impact-activated solidification of dense suspensions via dynamic jamming fronts," *Nature,* vol. 487, p. 205, 2012.

[76] H. J. van Gerner, M. A. Hoef, D. Meer and K. Weele, "Interplay of air and sand: Faraday heaping unravelled," *Phys. Rev. E,* vol. 76, p. 051305, 2007.

[77] P. D. Shoemaker and L. E. M. D. Chazal, "Dimpled and skirted liquid drops moving through viscous liquid media," *Chem. Eng. Sci,* vol. 24, p. 795, 1969.

[78] T. Wairegi and J. R. Grace, "The behaviour of large drops in immiscible liquids," *Int. J. Multiph. Flow,* Vols. 3, 67, 1976.

[79] B. Ray and A. Prosperetti, "On skirted drops in an immiscible liquid," *Chem. Eng. Sci,* vol. 108, p. 213, 2014.

[80] J. R. Royer, D. J. Evans, O. Loreto, Q. Guo, E. Kapit, M. E. Möbius, S. R. Waitukaitis and H. M. Jaeger, "High-speed tracking of rupture and clustering in freely falling granular streams," *Nature,* vol. 459, pp. 1110-1113, 2009.

[81] P. Bak, C. Tang and K. Wiesenfeld, "Self-Organized Criticality: An Explanation of the 1/ f Noise," *Phys Rev Lett,* vol. 59, p. 381, 1987.

[82] R. Li, H. Yang, G. Zheng and Q. C. Sun, "Granular Avalanches in Slumping Regime in a 2D Rotating Drum," *Powder Technol,* vol. 326, p. 322, 2018.

[83] J. J. McCarthy, T. Shinbrot, G. Metcalfe, J. E. Wolf and J. M. Ottino, "Mixing of Granular Materials in Slowly Rotated Containers," *AiChE J,* vol. 42, p. 3351, 1996.

[84] S. C. du Pont, R. Fischer, P. Gondret, B. Perrin and M. Rabaud, "Instantaneous Velocity Profiles during Granular Avalanches," *Phys. Rev. Lett,* vol. 94, p. 048003, 2005.

[85] S. K. Richter, V. Y. Zaitsev, P. Richard, R. Delannay, G. L. Caër and V. Tournat, "Experimental Evidence of Ageing and Slow Restoration of the Weak-Contact Configuration in Tilted 3D Granular Packings," *J. Stat. Mech. Theory Exp,* vol. P11023, 2010.

[86] N. a. G. D. I. Goldman, "Effect of Volume Fraction on Granular Avalanche Dynamics," *Phys. Rev. E,* vol. 90, p. 032202, 2014.

[87] V. Y. Zaitsev, P. Richard, R. Delannay, V. Tournat and V. E. Gusev, "Pre-Avalanche Structural Rearrangements in the Bulk of Granular Medium: Experimental Evidence, EPL Europhys," *Lett,* vol. 83, p. 64003, 2008.

[88] L. E. Silbert, D. Ertaş, G. S. Grest, T. C. Halsey, D. Levine and S. J. Plimpton, "Granular Flow down an Inclined Plane: Bagnold Scaling and Rheology," *Phys. Rev. E ,* vol. 64, p. 051302, 2001.

[89] Q. J. Zheng and A. B. Yu, "Modelling the Granular Flow in a Rotating Drum by the Eulerian Finite Element Method," *Powder Technology,* vol. 286, p. 361, 2015.

[90] J. K. Sveen, *An Introduction to MatPIV,* vol. 1, 2004.

[91] N. J. Balmforth and J. N. McElwaine, "From Episodic Avalanching to Continuous Flow in a Granular Drum," *Granular Matter,* vol. 20, p. 52, N. J. Balmforth and J. N. McElwaine, From Episodic Avalanching to Continuous Flow in a Granular Drum, Granular Matter 20, 52 (2018) 2018.

[92] N. A. Pohlman, S. W. Meier, R. M. Lueptow and J. M. Ottino, " Surface Velocity in Three-Dimensional Granular Tumblers,," *J. Fluid Mech.,* vol. 560, p. 355, 2006.

[93] M. Rabaud, R. Fischer, S. Courrech du Pont, P. Gondret and B. Perrin, "Dynamique Des Avalanches Granulaires," 2003.

[94] A. Penn, C. M. Boyce, T. Kovar, T. Tsuji, K. P. Pruessmann and C. R. Müller, "Real-time magnetic resonance imaging of bubble behavior and particle velocity in fluidized beds," *Ind. Eng. Chem. Res.,* vol. 57, p. 9674, 2018.

[95] H. K. Pak and P. R. Behringer, "Bubbling in vertically vibrated granular materials," *Nature,* vol. 371, p. 231–233, 1994.

[96] J. F. Davidson and D. Harrison, Fluidised Particles, Cambridge: Cambridge University Press, 1963.

[97] O. Pouliquen, J. Delour and S. B. Savage, "Fingering in granular flows," *Nature,* vol. 386, p. 816–817, 1997.

[98] R. Holtzman, M. L. Szulczewski and R. Juanes, "Capillary Fracturing in Granular Media," *Phys Rev Lett,* vol. 108, 2012.

[99] M. Shimokawa, R. Mayumi, T. Nakamura, T. Takami and H. Sakaguchi, "Breakup and deformation of a droplet falling in a miscible solution," *Phys Rev E,* vol. 93, 2016.

[100] M. Shimokawa and H. Sakaguchi, "Mode selection on breakup of a droplet falling into a miscible solution," *Phys Rev Fluids,* vol. 4, 2019.

[101] C. M. Boyce, A. Penn, M. Lehnert, K. P. Pruessmann and C. R. Müller, "Magnetic resonance imaging of single bubbles injected into incipiently fluidized beds," *Chem. Eng. Sci.,* p. 147, 2019.

[102] C. M. Boyce, A. Penn, A. Padash, M. Lehnert, K. P. Pruessmann and C. R. Müller, "Anomalous collapse of interacting bubbles in a fluidized bed: A magnetic resonance imaging study," *Phys. Rev. Fluids,* vol. 4, p. 034303, 2019.

[103] A. Penn, T. Tsuji, D. O. Brunner, C. M. Boyce, K. P. Pruessmann and C. R. Müller, "Real-time probing of granular dynamics with magnetic resonance," *Sci. Adv.,* vol. 3, 2017.

[104] O. Pouliquen, J. Delour and S. B. Savage, "Fingering in granular flows," *Nauture,* vol. 386, p. 816, 1997.

[105] F. T. Arecchi, P. K. Buah-Bassuah, F. Francini and S. Residori, "Fragmentation of a drop as it falls in a lighter miscible fluid," *Phys. Rev. E,* vol. 54, p. 424, 1996.

[106] F. T. Arecchi, P. K. Buah-Bassuah and C. Perezgarcia, "Fragment formation in the break-up of a drop falling in a mischible liquid," *EPL,* vol. 54, p. 429, 1991.

[107] N. Baumann, D. D. Joseph, P. Mohr and Y. Renardy, "Vortex rings of one fluid in another in free-fall," *Phys. Fluids A,* vol. 4, p. 567, 1992.

[108] N. G. Deen, M. Van Sint Annaland, M. A. Van der Hoef and J. A. M. Kuipers, "Review of discrete particle modeling of fluidized beds," *Chem. Eng. Sci.,* vol. 62, p. 28, 2007.

[109] H. R. Norouzi, R. Zarghami, R. Sotudeh-Gharebagh and N. Mostoufi, Coupled cfd-dem modeling: Foramulation, implementation and application to multiphase flows, Chichester: John Wiley & Sons, Ltd., 2007.

[110] H. P. Zhu, Z. Y. Zhou, R. Y. Yang and A. B. Yu, "Discrete particle simulation of particulate systems: Theoretical developments," *Chem. Eng. Sci.,* vol. 62, p. 3378, 2007.

[111] C. R. Müller, D. J. Holland, A. J. Sederman, S. A. Scott, J. S. Dennis and L. F. Gladden, "Granular temperature: Comparison of magnetic resonance measurements with discrete element model simulations," *Powder Technol.,* vol. 184, p. 241, 2008.

[112] C. R. Müller, S. A. Scott, D. J. Holland, B. C. Clarke, A. J. Sederman, J. S. Dennis and L. F. Gladden, "Validation of a discrete element model using magnetic resonance measurements," *Particuology,* vol. 7, p. 297, 2009.

[113] Z. Y. Zhou, S. B. Kuang, K. W. Chu and A. B. Yu, "Discrete particle simulation of particle-fluid flow: Model formulations and their applicability," *J. Fluid Mech.,* vol. 661, p. 482, 2010.

[114] D. L. Koch and R. J. Hill, "Inertial effects in suspension and porous-media flows," *Annu. Rev. Fluid Mech.,* vol. 33, p. 619, 2001.

[115] M. S. van Buijtenen, W.-J. van Dijk, N. G. Deen, J. A. M. Kuipers, T. Leadbeater and D. J. Parker, "Numerical and experimental study on multiple-spout fluidized beds," *Chem. Eng. Sci.,* vol. 66, p. 2368, 2011.

[116] T. B. Anderson and R. Jackson, "Fluid mechanical description of fluidized beds," *Equations of motion, Ind. Eng. Chem. Fundam,* vol. 6, p. 527, 1967.

[117] R. Beetstra, M. A. Hoef and J. A. M. Kuipers, "Numerical study of segregation using a new drag force correlation for polydisperse systems derived from lattice-boltzmann simulations," *Chem. Eng. Sci,* vol. 62, p. 246, 2007.

[118] T. Li, Y. Zhang and F. Hernández-Jiménez, "Investigation of particle–wall interaction in a pseudo-2d fluidized bed using cfd-dem simulations," *Particuology,* Vols. 25, 10, 2016.

[119] M. Faraday and Xvii, *On a peculiar class of acoustical figures; and on certain forms assumed by groups of particles upon vibrating elastic surfaces, Philos,* vol. 121, London, 1831, p. 299.

[120] B. Thomas and A. M. Squires, "Support for faraday's view of circulation in a fine-powder chladni heap," *Phys. Rev. Lett,* vol. 81, p. 574, 1998.

[121] F. A. O. Fontes, J. F. Sousa, C. P. Souza, M. B. D. Bezerra and M. Benachour, "Production Of Nbc from Nb2O5 in a Rotating Cylinder Reactor: Kinetic Study of Reduction/Carburization Reactions," *Chem. Eng. J,* vol. 175, p. 534, 2011.

[122] D. M. Scott, J. F. Davidson, S. E. Cheah, C. Chua, J. G. Gummow and L. B.P., "Transient Granular Flows in an Inclined Rotating Cylinder: Filling and Emptying, Ind," *Eng. Chem. Res,* vol. 48, p. 159, 2008.

[123] G. V. Prasanna Kumar, B. Srivastava and D. S. Nagesh, "Modeling and Optimization of Parameters of Flow Rate of Paddy Rice Grains through the Horizontal Rotating Cylindrical Drum of Drum Seeder, Comput," *Electron. Agric,* vol. 65, p. 26, 2009.

[124] K. Yamane, T. Sato, T. Tanaka and Y. Tsuji, "Computer Simulation of Tablet Motion in Coating Drum," *Pharm. Res,* vol. 12, p. 1264, 1995.

[125] G. Lu, J. R. Third and C. R. Müller, "The Parameters Governing the Coefficient of Dispersion of Cubes in Rotating Cylinders, Granul," *Matter,* Vols. 19, 12, 2017.

[126] G. Lu, J. R. Third and C. R. Müller, "Effect of Wall Rougheners on Cross-Sectional Flow Characteristics for Non-Spherical Particles in a Horizontal Rotating Cylinder," *Particuology,* vol. 12, p. 44, 2014.

[127] J. R. Third, D. M. Scott, G. Lu and C. R. Müller, "Modelling Axial Dispersion of Granular Material in Inclined Rotating Cylinders with Bulk Flow, Granul," *Matter,* Vols. 17, 33, 2015.

[128] G. Lu and C. R. Müller, "Particle-Shape Induced Radial Segregation in Rotating Cylinders, Granul," *Matter,* Vols. 22, 50, 2020.

[129] J. R. Third, D. M. Scott, S. A. Scott and C. R. Müller, "Tangential Velocity Profiles of Granular Material within Horizontal Rotating Cylinders Modelled Using the DEM," *Granul Matter,* vol. 12, p. 587, 2010.

[130] J. R. Third, D. M. Scott and C. R. Müller, "Axial Transport within Bidisperse Granular Media in Horizontal Rotating Cylinders," *Phys Rev E,* vol. 84, p. 041301, 2011.

[131] C. McLaren, J. R. Third and C. R. Müller, "Experimental Investigation of Axial Dispersion in a Horizontal Rotating Cylinder, Granul," *Matter,* Vols. 17, 43, 2015.

[132] J. R. Third, D. M. Scott, S. A. Scott and C. R. Müller, "Effect of Periodic Boundary Conditions on Granular Motion in Horizontal Rotating Cylinders Modelled Using the DEM, Granul," *Matter,* Vols. 13, 75, 2011.

[133] J. R. Third and C. R. Müller, "Is Axial Dispersion within Rotating Cylinders Governed by the Froude Number?," *Phys. Rev. E,* vol. 86, p. 061314, 2012.

[134] F. Cantelaube, Y. Limonuparcmeur, D. Bideau and G. H. Ristow, "Geometric Analysis of Avalanches in a 2D Drum," *J Phys,* vol. I 5, p. 581, 1995.

[135] M. Caponeri, S. Douady, S. Fauve and C. Laroche, Mobile Particulate Systems, Ecole Normale Superieure de Lyon, 1995.

[136] D. Fischer, T. Finger, F. Angenstein and R. Stannarius, "Diffusive and Subdiffusive Axial Transport of Granular Material in Rotating Cylinders," *Phys Rev E,* vol. 80, p. 061302, 2009.

[137] R. D. Keane and R. J. Adrian, "Theory of Cross-Correlation Analysis of Piv Images," *Appl. Sci. Res,* vol. 49, p. 191, 1992.

[138] S. Deboeuf, E. M. Bertin, E. Lajeunesse and O. Dauchot, "Jamming Transition of a Granular Pile below the Angle of Repose, Eur," *Phys. J. B - Condens. Matter Complex Syst,* vol. 36, p. 105, 2003.

[139] C. Xu and J. Zhu, "Parametric study of fine particle fluidization under mechanical vibration," *Powder Technol.,* vol. 161, pp. 135-144, 2006.

[140] H. Perazzini and F. Freire, "The influence of vibrational acceleration on drying kinetics in vibro-fluidized bed," *Chem. Eng. and Proc: Process Intensif.,* vol. 118, pp. 124-130, 2017.

[141] R. Daleffe, M. Ferreira and J. Freire, "Drying of pastes in vibro-fluidized beds: Effects of the amplitude and frequency of vibration," *Drying Technol.,* vol. 23, pp. 1765-1781, 2005.

[142] S. Karimipour and T. Pugsley, "A critical evaluation of literature correlations for predicting bubble size and velocity in gas-solid fluidized beds," *Powder Technol.,* vol. 205, pp. 1-14, 2011.

[143] E. Zhou, Y. Zhang, Y. Zhao, Z. Luo, J. He and C. Duan, "Characteristic gas velocity and fluidization quality evaluation of vibrated dense medium fluidized bed for fine coal separation," *Advanced Powder Technol.,* vol. 29, pp. 985-995, 2018.

[144] J. P. Metzger, C. P. McLaren, S. Pinzello, N. A. Conzelmann, C. M. Boyce and C. R. Müller, "The sinking dynamics and splitting of a granular droplet," *arXiv:2108.03106,* 2021.

[145] S. V. Franklin, Handbook of granular materials, CRC Press, 2016.

[146] R. Jullien and P. Meakin, "A mechanism for particle size segregation in three dimensions," *Nature,* vol. 344, p. 425–427, 1990.

[147] A. Rosato, K. J. Strandburg, F. Prinz and R. H. Swendsen, "Why the Brazil nuts are on top: Size segregation of particulate matter by shaking," *Phys. Rev. Lett.,* vol. 58, p. 1038–1040, 1987.

[148] R. Jullien, P. Meakin and A. Pavlovitch, "Three-dimensional model for particle-size segregation by shaking," *Phys. Rev. Lett.,* vol. 69, p. 640–643, 1992.

[149] J. C. Williams, "The segregation of particulate materials. A review," *Powder Technol.,* vol. 15, pp. 245-251, 1976.

[150] J. Duran, J. Rajchenbach and E. Clement, "Arching effect model for particle size segregation," *Phys. Rev. Lett.,* vol. 70, pp. 2431-2434, 1993.

[151] J. B. Knight, H. M. Jaeger and S. R. Nagel, "Vibration-induced size separation in granular media: The convection connection," *Phys. Rev. Lett.,* vol. 70, pp. 3728--3731, 1993.

[152] J. B. Knight, E. E. Ehrichs, V. Y. Kuperman, J. K. Flint, H. M. Jaeger and S. R. Nagel, "Experimental study of granular convection," *Phys. Rev. E,* vol. 54, pp. 5726-5738, 1996.

[153] W. Cooke, S. Warr, J. M. Huntley and R. C. Ball, "Particle size segregation in a two-dimensional bed undergoing vertical vibration," *Phys. Rev. E,* vol. 53, pp. 2812-2822, 1996.

[154] M. E. Möbius, B. E. Lauderdale, S. R. Nagel and H. M. Jaeger, "Size separation of granular particles," *Nature,* vol. 414, p. 270, 2001.

[155] V. Salinas, C. Quiñinao, S. González and G. Castillo, "Triggering Avalanches by Transverse Perturbations in a Rotating Drum," *Sci Rep,* vol. 11, 2021.

[156] Z. Wang and J. Zhang, "Fluctuations of Particle Motion in Granular Avalanches – from the Microscopic to the Macroscopic Scale," *Soft Matter,* vol. 11, p. 5408, Z. Wang and J. Zhang, Fluctuations of Particle Motion in Granular Avalanches – from the Microscopic to the Macroscopic Scales, Soft Matter 11, 5408 (2015 2015.

[157] R. Y. Yang, A. B. Yu, L. McElroy and J. Bao, "Numerical Simulation of Particle Dynamics in Different Flow Regimes in a Rotating Drum,," *Powder Technology,* vol. 188, pp. 170-177, 2008.

11 Acknowledgements

This work has only been accomplished thanks to the support of many people to whom I am very grateful. I want to specifically thank the following people:

Prof. Dr. Christoph Müller, for supervising me already in my Masters, guiding me through the entire process of being a PHD student, and teaching me through his corrections

Prof. Dr. Chris Boyce for helping to develop the key ideas of my thesis and especially for his time in Zürich.

Alex Penn for his extreme competence in MRI and as a great travel companion

Nicki, for great conversations insights and enjoyable lunches on the Polyterrasse and lots of expert help with my dissertation.

Jens, for his logical thought processes and mathematical genius

Meng for IT help

Aga, for her in the lab

Felix, for help with lab equipment and as a ski buddy

Cristina Faria, for helping with administrative tasks at ETH.

The granular group, Alex, Nicki., Chris B., Jens, Meng and Sergey for fun and productive granular meetings.

Everyone else at LESE, for being a fun and intelligent group.

Herr Gavoldi at the ITET, for preparing all the raw materials we needed for construction.

Daniel Wegmann and ITET for machining necessary parts.

The Bachelor and Master students who have worked with me: Sebastian Pinzello, Yi Tau Li, Yannick Fecke, Fabian Dickhardt, Amira Hamani, Andres Alexander, Yves Aschwaden, Nikolay Kirov, Marc Perret and Martin Reick.

Everyone else at the ETH for supporting me during the work for this dissertation.

My family and friends for their enduring support, love and encouragement.